ABSTRACT

Title of Dissertation:	A GENERALIZED METHODOLOGY TO DEVELOP PYROLYSIS MODELS FOR POLYMERIC MATERIALS CONTAINING REACTIVE FLAME RETARDANTS: RELATIONSHIP BETWEEN MATERIAL COMPOSITION AND FLAMMABILITY BEHAVIOR
	Yan Ding, Doctor of Philosophy, 2018
Dissertation directed by:	Associate Professor, Stanislav I. Stoliarov, Department of Fire Protection Engineering

The development of effective flame retardant polymeric materials is of great interest to the fire protection community. To enable intelligent design of flame retardant polymeric materials, it is important to understand the relation between the material composition and the chemical and physical properties that control the fire growth process. This work details a generalized methodology to characterize flame retardant materials for the development of pyrolysis models that relate the fire behavior to material composition.

The methodology employs thermogravimetric analysis, differential scanning calorimetry, and microscale combustion calorimetry, to measure the sample mass loss, heat required to decompose the sample, and the heat released from the complete combustion of the gaseous products evolved during the sample decomposition,

respectively. Through inverse analysis of the milligram-scale experimental measurements using a numerical pyrolysis framework, ThermaKin2Ds, the decomposition kinetics and thermodynamics, and heats of combustion of gaseous pyrolyzate are determined. The chemical interactions between the polymer matrix and flame retardants are characterized by second-order (two-component) reactions. The resulting reaction model reproduces all aforementioned experiments with a high degree of detail as a function of heating rate and captures changes in the decomposition behavior with changes in the flame retardant contents.

The methodology also utilizes a new bench-scale controlled atmosphere gasification apparatus to measure mass loss rate (MLR), back surface temperature, and sample shape profile evolution of 7-cm-diameter disk-shaped samples exposed to well-defined radiant heating. Inverse analysis of the bench-scale gasification experimental measurements using ThermaKin2Ds and the developed reaction model yields properties that define heat and mass transport in the pyrolyzing samples. This approach is demonstrated using two sets of materials: glass-fiber-reinforced polyamide 66 blended with red phosphorus and glass-fiber-reinforced polybutylene terephthalate blended with aluminum diethyl phosphinate and melamine polyphosphate. The resulting pyrolysis model is capable of predicting MLR data as a function of material composition and external heating condition. Idealized cone calorimetry simulations are conducted to demonstrate that, when the gas-phase combustion inhibition effect is excluded, aluminum diethyl phosphinate has a relatively minor impact on heat release rate, while the impacts of melamine polyphosphate and red phosphorus are significant.

A GENERALIZED METHODOLOGY TO DEVELOP PYROLYSIS MODELS FOR POLYMERIC MATERIALS CONTAINING REACTIVE FLAME RETARDANTS: RELATIONSHIP BETWEEN MATERIAL COMPOSITION AND FLAMMABILITY BEHAVIOR

by

Yan Ding

Dissertation submitted to the Faculty of the Graduate School of the
University of Maryland, College Park, in partial fulfillment
of the requirements for the degree of
Doctor of Philosophy
2018

Advisory Committee:
Professor Stanislav I. Stoliarov, Chair
Professor Marino diMarzo
Professor Michael J. Gollner
Dr. Richard E. Lyon
Professor Jose Torero
Professor Michael Zachariah, Dean's Representative

Acknowledgements

I started this section right after watching the movie – Everybody's fine. A widower sets off on an impromptu road trip to see his four grown children. The father found that all the kids lied to him and pretended to live a happy life because they were so afraid of letting him down. I realize that I am so lucky to be born in my family where my parents, Libao Ding and Yixian Wang, set appropriately high expectations for me. I really appreciate their understanding, strong support and encouragement through the past 26 years. Moreover, I am so grateful to have my best big brother, Qiang Ding, who is always there to protect and support me. Additional thanks go to my sister-in-law (Congling Zhao) and nephew (Yuchen Ding).

In addition to my family, my advisor, Dr. Stanislav Stoliarov, deserves the most significant acknowledgement. He has the most impressive work ethic I have ever encountered. Thanks for his constructive and insightful suggestions when I got stuck with my work, which plays a critical role in the progress of my PhD study. He is also an elder friend who teaches me the right way to be an excellent researcher, a responsible educator, and a nice person. Words cannot express how thankful I am to him.

My dissertation committee members (Dr. diMarzo, Dr. Gollner, Dr. Lyon, Dr. Torero and Dr. Zachariah) also deserve acknowledgement for providing valuable comments that have certainly improved the clarity of the research presented in this dissertation. Thanks in particular to Dr. Gollner who always provides strong support and helps me to treat the current situation from a different angle through sharing his

own experience. I also want to thank Dr. Lyon who drove all the way from New Jersey to Maryland to be my committee member.

I am certainly indebted to my lab-mates who collaborated with me on several projects, Mark McKinnon and Joshua Swann. Mark is my senior colleague (or second advisor) when I first came to University of Maryland and started my research. Thanks for his patience in teaching me how to operate various instruments and explaining the numerical modeling tool. Josh helped me a lot, especially with the experimental work. I also want to thank for their unique training on my English pronunciation. I also want to thank other lab-mates who provide useful suggestions on my research and life, which made my PhD study more colorful and enjoyable. Special thanks to Cara, Isaac, Conor, Dushyant, Xuan, Jing, Zhibo, Qi, Xi, Fernando, Ahmed, Chris, Jacques, Jess, Geri, Kevin, Chad, and Adam. Thanks to the diversity of our group, we ended up with seven different languages to express “good morning” when we see each other in the early morning, which partially motivated me to show up in the office every day.

I also owe a lot to those who went to gym together with me. I really enjoyed the work out. The people who deserve acknowledgement are Yizhou (bodypump partner), Conor (badminton partner), Cara/Evan (yoga partner), and Jess (HIIT partner). Great thanks to my great roommates, Yilin, Jiani, Lan, Qingjian, Qingqing, Wenxin, Luyao, Yamei, and Xianbo. They made me feel that I am not alone. I really appreciate the help from faculties (Dr. Milke, Dr. Quintiere, Ken, Dr. Sunderland, Dr. Trouve, Dr. Marshall), staffs (Christine, Nicole, Brian, Mary Lou, Kay, Sharon, Olga) and friends (Xingyu, Zhengyang, Xiaoyue, Paul, Shiyun, Salman, Luying, Ram, Dannis, Rui,

Xiuqi, Xinyun, Raquel, Hao) in the Fire Protection Department. Their smiles and greetings lit up my life.

Further thanks go to the friends outside of UMD: to Xiu, Cheng, Wei, Yilin, Pan, Yongjia, Xiaotian, for their understanding and strong support of both my academic and life pursuits. Final thanks go to the funding agencies: BASF and the U.S. National Science Foundation CAREER (Award #1347196 under the grant monitor Dr. Song-Charng Kong). Thanks for their strong support.

Table of Contents

List of Tables

List of Figures

Nomenclature

Symbols	Description
c	heat capacity [J $kg^{-1}K^{-1}$]
d	grid size
e	fitting parameters in Eq. (4.11)
h	heat evolved in reaction [J kg^{-1}] (h_c convective heat transfer coefficient [W $m^{-2}K^{-1}$], h_{com} heat of combustion
$\bar{h}$	area averaged convective heat transfer coefficient [W m^{-2} K^{-1}]
k	thermal conductivity [W $m^{-1}K^{-1}$]
m	mass [kg] (m_0 is the initial sample mass)
p	arbitrary property (see Eq. (4.1))
q	heat flux due to radiation, thermal conduction or convection [W m^{-2}]
q''	heat flux due to radiation [W m^{-2}] (see Eq. (3.2))
$\dot{q}$	heat flow rate to a sample material [W kg^{-1}]
r	reaction rate [kg $m^{-3}s^{-1}$]
r_z	radial distance from the sample center [m]
t	time [s]
u	coefficient in transient heating rate expression (Eq. (4.7))
x	axial direction [m]
z	radial direction [m]
A	Arrhenius pre-exponential factor [$(m^3$ $kg^{-1})^{n-1}$ s^{-1}] (reaction of order n)
C	gas concentration [kg m^{-3}]
E	activation energy [J mol^{-1}]
H	distance from the sample surface to the bottom of the heater housing [m]
I	radiant flux [W m^{-2}]
J	mass flux [kg $m^{-2}s^{-1}$]
N	number of components
N_r	number of reactions
R	sample radius [m]
R_u	universal gas constant [J $mol^{-1}K^{-1}$]
T	temperature [K]
V	volume fraction
θ	stoichiometric mass coefficient

ξ	mass concentration [kg m^{-3}]
λ	mass transport coefficient [m^2 s^{-1}]
κ	absorption coefficient [m^2 kg^{-1}]
ϵ	emissivity
α	thermal diffusivity [m^2 s^{-1}]
α_{con}	conversion
γ	reflection loss coefficient
δ	thickness of sample [m]
ρ	density [kg m^{-3}]
σ	Stefan-Boltzmann constant [W $m^{-2}K^{-4}$]

Subscripts

back	back surface
c	convection
com	combustion
con	conversion
ex	radiation from external sources
g	gas g
i	reaction i
in	inlet
int	intermediate component
j	component j
P	peak
peak	maximum mass loss rate or temperature at which the maximum occurs
rr	re-radiation from sample material
s	sample top surface
top	the plate on the top of the heater, see Figure 4.1
W	radius of the cylinder used in the ThermaKin2Ds verification
z	radial direction

Superscripts

0	net radiation
top	top sample surface (see Eq. (4.11))
n	exponent for last term in Eq. (4.1)

Acronyms

DEPAL	Aluminum Diethyl Phosphinate
FAA	US Federal Aviation Administration
FPA	Fire Propagation Apparatus

GF	Glass Fiber
HRR	Heat Release Rate
MCC	Microscale Combustion Calorimetry
MLR	Mass Loss Rate
MPP	Melamine Polyphosphate
NIST	US National Institute of Standards and Technology
PA66	Polyamide 66 or Nylon 66
PBT	Polybutylene Terephthalate
RP	Red Phosphorus
SLPM	Standard Liters per Minute (at 1 atm and 298 K)
STA	Simultaneous Thermal Analysis
TGA	Thermogravimetric Analysis

Chapter 1. Introduction

1.1 Background

There has been a sharp increase in the use of synthetic polymeric materials during the past 60 years. Polymers are widely used in both high technology and household applications due to low weight, high tensile strength and low processing cost. Most polymers contain a large fraction of carbon and hydrogen atoms, which makes their composition similar to that of fossil fuels. Therefore, one key disadvantage of polymers is their inherent flammability. Most polymer-containing products must satisfy fire safety standards to assure public safety. As a recent example, an exterior aluminum-polyethylene cladding, which failed to meet the flammability requirements, contributed to the destructive Grenfell Tower fire in June 2017 [1]. As this example demonstrates, the flammability of polymeric materials is a serious concern.

A traditional solution to the polymer flammability problem is to incorporate flame retardants into the polymer to reduce its fire hazard. A flame retardant is a chemical that, when added to a combustible material, slows flame spread of the resulting material by promoting the formation of a char layer on the surface of the material or by inhibiting the chemical reactions in the flame [2]. Flame retardant materials have contributed to a significant reduction in the frequency of occurrence and the severity of fire events. For example, the number of television fires in Europe is estimated to be at least an order of magnitude higher than in the USA where the fire safety classifications for television enclosure materials has been more stringent and

flame retardant materials have been used [3]. Therefore, to further reduce the frequency of occurrence of fire events, it is very important to develop new and more effective flame retardant materials and design a set of methods to evaluate the fire performance of the developed materials.

Several standard test methods [4–6] that mimic fire scenarios have been developed and employed to assess the material's fire behavior. However, each of these tests is configuration specific. There has been limited success in attempts to extrapolate the generalized results to different scenarios. Additionally, these standard test methods offer limited quantitative insights into the fundamental chemical and physical processes that occur during pyrolysis.

The limitations of the standard test methods have necessitated the rapid development of computational fire models that are capable of predicting the fire response of solid materials over a wide range of scenarios. Such models can provide a rapid and cost-effective assessment of material flammability by reducing the number of costly physical tests required to assess the flammability of a material. Fire models are characterized by a complex coupling of gas-phase and condensed-phase phenomena. Much work has focused on understanding the physics in gas-phase processes such as gas-phase combustion, turbulence, soot formation, and oxidation. However, the condensed-phase pyrolysis of burning materials have been less studied and understood due to the complexity of the fundamental physical and chemical processes [7]. The condensed-phase pyrolysis process is critical in the burning process because it generates the volatiles required for combustion [7]. Therefore, the

development of a comprehensive pyrolysis model plays a significant role in predicting ignition and growth of fires.

In order to develop the pyrolysis model, a complete set of material properties as model inputs are required. These parameters include decomposition kinetic and thermodynamic parameters as well as thermal transport properties. Some success has been achieved in evaluating material properties and developing pyrolysis models for non-charring, charring, and composite materials [8–13]. As the demand for effective flame retardant additives to engineered plastics increases [14], it is crucial to extend the current methods to aid in developing pyrolysis models for polymeric materials blended with flame retardants.

1.2 Literature Review

1.2.1 Review of Pyrolysis Modeling Development

It is recognized that the condensed-phase pyrolysis process that produces the volatiles required for combustion plays an important role in the ignition, flame spread, and burning process during the early stage of fire growth [7]. Significant efforts have been made to develop mathematical pyrolysis models to gain insight into the pyrolysis process. Several studies [15–17] provide useful summaries of the modeling of the complex chemical and physical processes that occur in the pyrolysis of solid materials.

Pyrolysis models may be classified into either simple thermal models or comprehensive models based on the assumptions made to simplify the scenario. A major distinction between these two types of models is that thermal models rely on the assumption of infinite-rate reaction kinetics while comprehensive models account for

finite-rate reaction kinetics. In thermal models, the thermal decomposition process begins abruptly when the temperature reaches a critical value. The application of the critical decomposition temperature greatly reduces the model complexity to a single energy balance equation, which effectively decouples the thermal degradation process from other physical processes.

The thermal models can be further categorized into two main groups in terms of the solution approach: simple analytical and integral models [16]. Analytical models are closed-form solutions for the rate of pyrolyzate production using the critical pyrolysis temperature. Despite the simplicity and convenience of analytical models, they have very limited usability because of the low accuracy resulting from the neglected physical and chemical processes.

Integral thermal models are less restrictive than analytical models as they account for the physical phenomena (i.e. transient heat conduction, charring process, and flame heat transfer) ignored in simple models. Integral models also have the advantage of being computationally economical. An initial sample temperature distribution that depends on the spatial variable is substituted into the heat conduction equation and integrated with respect to the spatial variable to obtain the heat balance integral. Therefore, the original partial differential problem is simplified into an ordinary differential equation with time as the independent variable. A wide range of temperature distribution profiles including polynomial and exponential temperatures have been reported [18]. Recent studies showed that integral models were able to provide a reasonable accuracy for engineering purposes [19–22]. This type of model is also known as a Stefan problem.

Quintiere developed an integral model to describe the burning rate of solid materials [19]. This model included the charring process, vaporization, flame heat transfer, and transient heat conduction effects. It was assumed that the fuel decomposed to char and volatiles in an infinitesimally thin pyrolysis front at a fixed vaporization temperature. This model was applied to the gasification of a non-charring material by Quintiere and Iqbal [20]. Further examination of this model was conducted against the experimental data of semi-infinite charring solid materials collected by Spearpoint and Quintiere [21]. The mass loss and temperatures of four species of wood exposed to incident heat fluxes of 25-75 kW m^{-2} were measured. A second-order polynomial function was selected as the temperature distributions for the virgin material. All the material properties were assumed to be constant during the experiment. This model was found to provide reasonable predictions of the mass loss rates (MLR) and surface temperatures.

Another similar integral model for predicting the burning of non-charring and charring materials was successfully demonstrated by Moghtaderi et al. [22]. A quadratic profile for the temperature distribution within the material was assumed. All the thermal properties were considered constant (independent of temperature and location). This model was validated against surface temperature, MLR, and char depth of pyrolyzed material obtained from analytical and numerical solutions, as well as experimental data. Though the integral models address the shortcoming of closed-form solutions, like all other thermal models, integral models employ the critical temperature criterion and therefore neglect the effect of chemical kinetics on the overall thermal

decomposition process. In addition, the simplified heat balance equations with the selected temperature profiles are not as accurate as the original un-simplified equations.

Several comprehensive models have been developed to account for the finite chemical reaction rate and solve the partial-differential energy conservation equation. The Arrhenius equation is often used to calculate the reaction rate as a function of temperature. Comprehensive models utilize a lumped-species reaction scheme to provide thermal degradation rates in the condensed-phase. Although several molecular dynamics techniques, including reactive empirical bond-order potentials [23], ReaxFF force field [24,25], and reactive molecular dynamics [26–29], have been developed to provide detailed chemical reaction mechanisms, the simple lumped-species reaction scheme provides sufficient mass loss information while greatly saving computational cost and efforts [30].

There are three classes of reaction schemes in the literature [15] including one-step global reaction scheme, one-step multi-reaction scheme, and multi-step semi-global reaction scheme. One-step global reaction schemes employ a single reaction to describe the total mass loss that occurs in the pyrolysis process [15]. One-step, multi-reaction schemes use several parallel reactions that include a single reaction step for each virgin material [15]. Multi-step semi-global reaction schemes represent the most realistic reaction mechanisms and include primary reactions as well as secondary reactions that represent further degradation of the intermediate condensed-phase products [15].

Different levels of approximations have been made when modelling the complex physical processes of pyrolysis. In 1945, Bamford et al. [31] adopted a simple approach

of a Fourier heat conduction equation with a source term representing the heat generated by chemical reaction. Thermal decomposition was represented by a single first-order reaction. Reaction kinetics were approximated through measurements of the rate of decomposition of wood at various temperatures. A vertical sheet of wood was heated on each parallel face by a flame and the central temperatures of pyrolyzing wood were measured. This model provided reasonable predictions of the experimental central temperatures. Tinney [32] developed a similar mathematical model to describe the combustion behavior of small wooden dowels heated externally. In these two studies by Bamford et al. and Tinney, the variation of thermal properties in temperature and time and the convective heat transfer of volatiles were neglected. In 1972, Kung [33] developed a more realistic model that included variable thermo-physical properties and also accounted for internal heat convection due to the transport of volatiles. The flowing gases were assumed to be in thermal equilibrium with the condensed-phase materials.

More recently, several generalized comprehensive pyrolysis models that can simulate the gasification of a variety of solid materials have been developed. The most prominent are Gpyro [34], the solid-phase model for National Institute of Science and Technology (NIST) Fire Dynamics Simulator (FDS) [35], and ThermaKin [36]. It should be noted that the term "model", when used in this study, represents both the modeling tools and specific sets of material properties.

Gpyro [34] is an open-source model that is capable of simulating a wide range of scenarios. Temperature, species, and pressure distributions inside the sample are determined by solving the corresponding conservation equations for both gas-phase

and condensed-phase. The energy conservation equation takes into account conduction, heats of reaction, convection from the gas-phase components to the condensed-phase components, and in-depth absorption. However, the in-depth emission is assumed to be negligible and neglected in the model. The heat transfer between the gas-phase and condensed-phase components can be calculated using either thermal equilibrium or two-temperature (non-equilibrium) formulations. The gas-phase momentum is represented using Darcy's law. The chemical reactions are described in Gpyro with Arrhenius reaction parameters and both heterogeneous and homogeneous reactions can be captured.

The FDS solid-phase model [35] at NIST has the advantage of being coupled to the FDS gas-phase solver and can be applied in a wide range of fire scenarios. The conservation equations of mass, energy, and species are included and solved to predict the mass loss data. The energy equation takes into account the conduction in the solid phase, heats of reaction, in-depth radiation absorption, and in-depth emission of radiation. A "two-flux" model is employed to account for the radiation into and out of the sample. The model allows for multiple reactions in parallel or in sequence with an Arrhenius expression for the reaction rate. One limitation of FDS solid-phase model is that the gases generated in depth are assumed to be transported to the top surface instantaneously. In addition, FDS solid-phase model cannot simulate two-reactant reactions. The FDS condensed-phase model has been employed extensively in research and modeling efforts [37–39].

ThermaKin was developed by Stoliarov and Lyon [36] at the Federal Aviation Administration (FAA). The major difference between ThermaKin and the condensed-

phase model in FDS is the in-depth radiation absorption model. In ThermaKin, external radiation is absorbed within a single element that is selected at each time step using a random absorption algorithm. The Beer-Lambert distribution of absorbed energy is applied using a probability density function to guide this selection. Radiative heat transfer inside the sample is considered by applying the radiation diffusion approximation [40]. Both first-order and second-order (two solid components) reactions can be defined. This model has a flexibility to define most of the thermo-physical parameters of a component as functions of temperature using quadratic polynomial formulations.

All of these generalized models require a complete set of materials properties as model inputs in order to predict the rate of gaseous pyrolyzate production during pyrolysis of solid materials. These parameters include decomposition kinetic and thermodynamic parameters and thermal transport properties. A number of techniques have been developed to estimate the material properties. Although large-scale methods provide the closest representation to the real scenarios encountered in the built environment, the most commonly used methods are either milligram-scale or bench-scale because the complexity and costs for fire tests increase significantly with increasing scales.

Thermogravimetric Analysis (TGA) is a widely used milligram-scale test that can be used to determine the thermal degradation kinetics (pre-exponential factor, activation energy, and stoichiometric coefficients of reactions). In TGA [41], the sample mass is measured as the environmental temperature follows a user-specified temperature program in a well-defined gaseous atmosphere. The temperature is

controlled by a furnace that is capable of isothermal or dynamic heating (or cooling) of the sample. The small sample mass (5 to 10 mg) and low heating rates (10 to 30 K min^{-1}) are employed to ensure thermally thin behavior (no significant temperature or concentration gradients within the sample), effectively decoupling the chemical reactions from heat and mass transfer processes. The sample is contained in a ceramic or platinum crucible. The crucible may have a lid to improve the uniformity of the temperature profile within the sample or may not have a lid to improve the interaction between the sample and the atmosphere. A well-defined flowing atmosphere (often nitrogen or air), with a flow rate on the order of 100 mL min^{-1}, helps to reduce condensation and deposition of gaseous products, flush out the corrosive byproducts, and reduce the possibility of secondary reactions.

The Arrhenius equation was utilized to represent the solid-state chemical reactions [42]. The application of the Arrhenius equation to solid-state kinetics was justified by Galwey and Brown [43]. The Arrhenius equation and its relation to the sample MLR are shown in Eq. (1.1).

$$\frac{d\alpha_{con}}{dt} = A\exp\left(\frac{-E}{R_u T}\right) f(\alpha_{con}) \tag{1.1}$$

$$\alpha_{con} = \frac{(m_0 - m)}{(m_0 - m_f)} \tag{1.2}$$

α_{con} is the extent of conversion, defined in Eq. (1.2). A and E are the pre-exponential factor and activation energy, respectively. R_u represents the universal gas constant. T denotes the temperature. m_0 indicates the initial sample mass, m_f denotes the final mass, and m represents the instantaneous mass at time t. $f(\alpha)$ is the reaction model. The first-order reaction model, where the reaction rate is only dependent on one

reactant concentration, was widely adopted and found to be applicable for most solid materials [8,17,40,44–46]. A set of different reaction models applied to describe thermal decomposition in solids can be found in a study by Vyazovkin and Wight [47].

Isothermal and non-isothermal heating (usually constant heating rate) are two commonly used methods to estimate the reaction rate [48]. The isothermal method [49,50] yields time-evolved measurements at constant temperature. The main advantage of this method is that changes in the reaction mechanism are detectable because decomposition rates are obtained at a single temperature. In contrast to the non-isothermal method, the kinetic parameters are easily determined analytically. The disadvantage of the isothermal method is that the sample experiences a non-isothermal heating period (transition from one single temperature to another) and undergoes unknown transformations that likely affect the calculations. The non-isothermal technique mitigates this issue by heating the sample to a very high temperature at a prescribed heating rate. However, the reaction parameters in this case do not have analytical solutions and are more difficult to determine.

Model-fitting [51] and model-free (iso-conversional) [52] methods have been developed to determine the reaction parameters. One disadvantage with model-fitting method is that different sets of Arrhenius parameters are able to predict the same experimental results due to the kinetic compensation effect [47,53]. This uncertainty in the kinetic triplet (reaction model, activation energy, and pre-exponential factor) may result in unreliable parameterization of kinetic parameters.

The iso-conversional method relies on multiple heating rates and is able to yield the activation energy as a function of the extent of conversion ($E_{\alpha_{con}}$). It is called

"model free" because activation energy can be obtained independent of the reaction model. Several iso-conversional methods have been developed to determine the reaction parameters [52]. Friedman [54] proposed a differential iso-conversional method which required numerical differentiation of the experimental α_{con} with respect to T. However, this method often resulted in noisy data and thus, unstable $E_{\alpha_{con}}$. Integral iso-conversional methods [52,55,56] were developed to avoid this issue. Integral iso-conversional methods are computed either by approximation or numerical integration since analytical solutions did not exist.

Differential scanning calorimetry (DSC) [57] is a method that measures the difference between the heat flow rate to a milligram-sized sample and a standard reference. The system is subjected to a well-defined temperature program and a well-controlled gas environment. The sample and reference are both held in crucibles with lids to improve the uniformity of the temperature profile within the sample and reference. In this work, the TGA instrument operates in combination with DSC to simultaneously measure the mass loss and heat flow, which decreases the number of tests required and uncertainty between mass loss and heat flow data.

There are two main types of DSC [58] (heat flux DSC and power-compensated DSC) and the main difference between the two types of DSC lies in the construction and principle of the measurement. In a heat flux DSC, there is a single furnace that heats both the sample and reference. The primary measurement is the temperature difference between the sample and the reference while the sample undergoes glass transition, melting or chemical reactions. The temperature difference is related to the heat flow to the sample through a calibration curve determined based on the heats of

melting of several salts and metals that are well characterized in literature. In a power-compensated DSC, there are two independent furnaces. The temperatures of the sample and reference are kept at the same value via independent heating. As the sample absorbs energy due to sensible enthalpy changes, the sample furnace increases the heating power to maintain the temperature program. The difference in heating power provides a direct measurement of the heat flow to the sample. The analysis of DSC measurements allows for the determination of thermodynamic parameters of thermal decomposition. In this work, simultaneous thermal analysis (STA) was employed to simultaneously conduct both TGA and DSC tests to reduce the number of experiments as well as accurately determine decomposition kinetics and thermodynamics.

In addition to defining decomposition kinetics and thermodynamics, a pyrolysis model requires the quantification of thermal transport parameters including optical properties and thermal conductivity. The optical properties are the surface emissivity, surface absorptivity, and absorption coefficient. The optical properties have been found to have a significant effect on the time to ignition [59].

Most fire scenarios have temperatures around 1200 K or lower, which means that most of the energy released by radiation from the fires is in the infrared part of the spectrum around 2 μm or higher [60]. Tsilingiris [60] conducted an analysis to calculate the total infrared transmission of various polymer film materials for a broad range of radiant source temperatures from 273 to 873 K. Polyethylene and polypropylene were found to have a very high transmission while materials like fiberglass, kapton, and mylar had a low transmission. The effects of source temperatures on the total transmission were found to vary from sample to sample.

Försth and Roos [61] conducted an extensive study to measure the absorptivity of 62 products in the wavelength region of 0.3 – 20 μm. An integrating sphere was utilized to perform the reflectance and transmittance measurements. All of the measurements were conducted at room temperature. The effective absorptivity of most of the tested materials changed less than 10% when the temperatures of heat sources varied from 674 K to 1300 K. The authors also found that the effective absorptivity of some materials exposed to a cone heater decreased with increased exposure time.

Linteris et al. [62] measured the absorption coefficients and total reflectance of 11 commonly used thermoplastics. The absorption coefficients were calculated from data collected with two different methods, an integrating sphere and a broadband method. The first method measured the reflected or transmitted energy through the sample, and a ratio to the reference beam through the empty reference port of the sphere was computed. The second approach is similar to that developed by Jiang et al. [63] where the absorption coefficients were determined by comparing the radiative heat flux transmitted through the sample with the heat flux incident to the sample. It was found that both methods provided reasonably consistent results with each other. The average absorption coefficient was found to be highly dependent on the sample thickness and source temperature.

While optical properties can be measured directly, it is very difficult to measure the thermal conductivity of samples that undergo thermal degradation. The existing methods for the measurement of thermal conductivity can be classified as steady state and dynamic/transient. The steady state methods, for example, guarded-hot-plate [64] and heat flow meter apparatus [65], are governed by a similar principle where heat

fluxes through the materials are measured while the temperatures at both sides of sample are maintained constant. However, these methods require samples with parallel sides and the dimensions to remain unchanged during the measurements. In addition, such methods require a relatively long time to reach steady state.

Several transient methods have been developed and are used to measure the thermal conductivity as a function of temperature. Most of the existing studies only focused on measurements up to a temperature that was below the onset of decomposition. Harada et al. [66] used the flash method [67] to measure the thermal properties of wood from room temperature up to 543 K. Zhang and Fujii [68] employed the transient short-hot-wire method [69] to measure the thermal conductivity and thermal diffusivity of nine polymers up to about 500 K. The design of a short-hot-wire (about 10 mm long) allowed for the use of a small amount of sample, which ensured uniformity inside the sample. This method was especially suitable for measurements of molten polymers. Assael et al. [70] improved the transient-hot-wire technique by introducing a soft-paste material to minimize the thermal-contact resistance. The thermal conductivity of poly(methyl methacrylate) (PMMA) was measured from room temperature up to 350 K. Stoliarov el al. [8] measured the thermal conductivity of several polymers using a Thermoflixer apparatus that was based on the transient line source method. The measurements of several polymers were performed in the temperature range between 315 K and the stability limit point (50 K below the onset of the decomposition).

Those transient methods require two or more measurement points at well-defined locations and a good thermal contact to obtain accurate measurements. However,

samples may expand/shrink and/or form porous structures during the pyrolysis process. Therefore, these methods cannot measure thermal conductivity of the intermediate products or char produced during decomposition process.

It is challenging to accurately measure all the material properties of pyrolyzing materials. Any changes and/or uncertainties of the properties will affect the predictions of the burning rate and heat release rate. Comprehensive sensitivity analyses have been conducted to identify the most relevant parameters. Stoliarov et al. [71] employed ThermaKin to analyze the effect of independently varying polymer properties (thermal, optical, and chemical properties) on the rate of burning. A number of literature sources containing information on synthetic polymers were used to determine the average values and boundaries of these properties. It was found that the heats of decomposition, char yield, pre-exponential factor, and activation energy are of key importance for the prediction of the peak and average burning rates. Density, heat capacity, and thermal conductivity are of little significance.

Linteris [72] performed an additional sensitivity analysis to study the effects of properties variation on the time-dependent MLR (time to ignition and time to peak MLR) in addition to the effects on global parameters (such as peak heat release and average heat release) reported by Stoliarov et al [71]. It was found that the heats of reaction and thermal conductivity have the greatest and least effects on the prediction of the polymer decomposition, respectively. The absorption coefficient influenced the shape of the MLR curve and ignition time. The variation of material thickness also showed significant effects on the shape of the MLR curve and time to peak MLR. These sensitivity studies can be helpful in reducing the dimensionality and complexity of

models for a given application and guiding experimental design to focus on the most critical properties.

In addition, the design of customized bench-scale flammability apparatuses have contributed to the development of pyrolysis modeling. The cone calorimeter is one of the most widely used bench-scale methods to investigate the material burning process and to estimate the material properties [8,34,39,40,73,74]. One issue with the cone calorimeter is that the tests are conducted in well-ventilated, open air whereas ventilation is usually limited during real fire scenarios. Additionally, the effects of oxidation and gas-phase combustion on condensed-phase pyrolysis cannot be eliminated in the poorly defined boundary conditions of cone calorimeter tests. Therefore, specialized bench-scale gasification techniques were required to provide well-defined boundary conditions and to decouple these additional effects from condensed-phase pyrolysis. These instruments includes NIST gasification apparatus [75], fire propagation apparatus (FPA) [76], mass loss calorimeter [77], and controlled atmosphere pyrolysis apparatus (CAPA) [78]. These techniques enable the simultaneous measurement of sample mass loss and sample temperature in an anaerobic environment. Several methods have been proposed to determine a complete set of material properties based on the data obtained from these bench-scale tests.

Lautenberger et al. [79] proposed a methodology that employed an automated optimization technique integrated with the NIST FDS pyrolysis model to estimate the materials properties from experimental data collected from cone calorimeter tests. Two charring materials (redwood and red oak) and one thermoplastic material (polypropylene) were tested and surface temperatures and MLR were recorded. A

genetic algorithm (GA) that imitates the principles of natural selection and mutation was developed. The initial set of property values are randomly generated and the next set are created by stochastic mutations. The magnitude of the mutations is decreased with each iteration until convergence is achieved and no subsequent improvements occur. GA's advantages include excellent performance in high-dimensional and non-linear problems, resistance to solution being trapped in a local optima, and wide exploration of the parameter space. GA was used to determine parameter sets that provided near-optimal agreement between the model predictions and experimental data. All the properties were assumed to be independent of temperature. The developed models provided satisfactory predictions of experimental data.

Chaos et al. [76] employed a more advanced optimization scheme (Shuffled Complex Evolution (SCE) approach) to determine the material properties from pyrolysis data collected in FPA tests. SCE has the advantage of considerably reducing the number of iterations required for convergence and providing more accurate predictions compared to GA. The one-dimensional (1D) pyrolysis model developed by Chaos et al. was based on the principles of Gpyro [34]. The model coupled with SCE was employed to estimate the parameters of three materials: PMMA, single-wall corrugated board, and chlorinated polyvinyl chloride. It should be noted that only MLR data were used to develop the pyrolysis model. The surface temperature data measured with an infrared pyrometer were not used in model development due to the unknown surface emissivity. The temperature-dependency of properties was not considered. This approach predicted the MLR data of the tested materials exposed to several heat fluxes very well. It is noted that Chaos et al. attempted to estimate all the material properties

though a single set of experimental data for pyrolyzing materials that undergo a complex coupling of physical and chemical processes. The resulting material properties may not be representative of the actual physical and chemical properties and thus the extrapolation to scenarios outside of calibration conditions were unjustifiable [34,80]. Therefore, it is crucial to design an approach to yield more physically realistic parameters that can describe material response to conditions outside the calibration scenarios.

Li et al. [9,46,78,81] developed a methodology to parameterize the material properties for pyrolysis model development of solid materials in a hierarchical way. This methodology was based on the TGA, DSC, and CAPA experiments coupled with inverse numerical modeling of these experimental data using ThermaKin. First, TGA and DSC tests where the chemical reactions were decoupled from the mass and heat transport processes were conducted to determine to the kinetics and thermodynamics of decomposition, respectively. Second, the back surface temperatures were obtained by focusing a calibrated infrared camera on the bottom sample surface through a gold-coated flat mirror in CAPA experiments. An inverse analysis of the measured back surface temperatures was employed to determine the thermal conductivity of components. The temperature-dependency of the parameters were considered. Third, the MLR data obtained from CAPA tests, not used as parameter calibration, were employed to validate the resulting parameters. This methodology has been successfully applied to a set of non-charring and charring polymers [9,46,78,81]. The resulting pyrolysis models were able to predict the experimental burning rates collected at different heat fluxes beyond the calibration range.

McKinnon et al. [12,82] extended this existing methodology to construct pyrolysis models for highly complicated composites. Microscale combustion calorimeter tests were also introduced to determine the complete heats of combustion of evolved volatiles [83]. The heats of combustion are critical for fire risk assessments as it relates the burning rate to the heat release rate. In the study of the multilayer floor covering [82], McKinnon and Stoliarov parameterized each layer individually to identify its contribution to the overall response of the composite. The combination of different layers produced a fair agreement between the experimental and simulated data of the composite. The potential physical and chemical interactions between layers were not considered.

As the demand for more effective and environmentally friendly flame retardant additives to engineered plastics increases [14], it is crucial to extend this methodology to flame retardant materials for pyrolysis model development. Girardin et al. [84] attempted to develop a pyrolysis model of a multi-component flame retardant system. During the model construction, the blend was treated as a single component and the potential chemical and physical interactions between each component were not taken into account. Knowledge of the interactions enables a quantitative understanding of the relation between the fire behavior and the material composition (flame retardant content), which plays a critical role in designing flame retardant materials with optimal fire resistance and other excellent mechanical properties.

1.2.2 Review of Characterization of Flame Retardant Materials

A number of flame retardants, which act on a material with different physical and chemical mechanisms to improve the material fire performance, have been explored

for various polymers. In general, flame retardants can be classified into three different types based on the mechanisms of flame retardant action [85]: gas-phase flame retardancy, char-forming flame retardancy, and endothermic flame retardancy. The first and second flame retardancy methods are more widely adopted.

Halogenated flame retardants have been in use since the 1930s and have been found to be the most effective for a wide range of polymers. Among all the halogenated flame retardants, brominated flame retardants are most widely used since they are highly efficient and relatively inexpensive [86]. It was found that the C-Br bond is stable enough for environmental exposure and yet unstable enough that heat can easily break the bond, releasing the bromine under fire conditions to inhibit free radical combustion reactions in the vapor phase. However, significant concerns have been raised regarding the persistence of brominated flame retardants in the environment, the tendency of brominated flame retardants to bio-accumulate and their potential toxicity [87,88]. Efforts have been made to develop environmentally friendly alternatives to halogenated flame retardants.

Halogen-free phosphorus-based flame retardants have gained increasing popularity for various polymeric materials since they can be effective in both vapor phase through flame inhibition and condensed-phase by producing and enhancing char layers [89–92]. Phosphorus-based flame retardants can vary greatly from inorganic to organic forms and vary between oxidation states (0, +3, +5) [93]. Even at a relatively low loading level (mass concentration), the phosphorus-based flame retardants demonstrate effective flame retardancy [94]. In addition, the phosphorus compounds act as acid catalysts in the intumescent systems to initiate the char formation process to

produce a protective carbon layer. An intumescent system [95] consists of three components: an acid catalyst, a carbon source, and a blowing agent. The intumescent systems are typically used to provide fire protection for fire barriers and applications requiring a high level of fire safety.

In this work, two widely used phosphorus-containing flame retardant polymers are investigated: glass fiber reinforced polyamide 66 (PA66/GF) blended with red phosphorus (RP) and glass fiber reinforced polybutylene terephthalate (PBT/GF) mixed with aluminum diethyl phosphinate (DEPAL) and melamine polyphosphate (MPP). The engineering plastic PA66 has an excellent electrically insulating property, high tensile strength, and high ductility, and has been widely used as electrical insulator. However, pure PA66 has poor dimensional stability and poor resistance to long-term heat exposure [94]. Therefore, additives are always incorporated into PA66 to maintain dimensional stability and increase fire resistance before use in electrical and electronic products where fire resistance is required. The incorporation of glass fiber helps to prevent the PA66 from dripping. However, glass fiber reinforced PA66 is more combustible than the pure PA66 due to the "wick effect" [96,97] where the molten polymer is transported from regions of higher concentration to regions of lower concentration. Phosphorus-containing additives have been found to be very effective in improving the fire performance of PA66/GF. Red phosphorus blended with PA66/GF is the most widely used [93,98]. It was found that the incorporation of 6-8 wt.% of red phosphorus (RP) into glass fiber reinforced polyamide blends yields a V-0 rating in UL 94 tests [94]. UL 94 [5] is a standard test for flammability of polymeric

materials used for parts in devices and appliances. Materials that obtain a V-0 rating are classified to be flame resistant.

Schartel et al. [99] conducted an extensive study of the decomposition and combustion behavior of seven glass fiber reinforced PA66 blends. Thermogravimetry (TG) coupled with Fourier Transform Infrared Spectroscopy, and TG coupled with Mass Spectroscopy, were used to investigate the thermal decomposition of the blends. A cone calorimeter was employed to analyze their combustion behavior. With the introduction of RP, the MLR curves showed two separate decomposition peaks in TG results. The temperature regions of the decomposition MLR curve of RP-containing blends were broadened. The cone calorimeter results showed that RP acted in condensed-phase decomposition by increasing the amount of char. The produced char acted as a barrier layer that inhibited the mass and heat transfer, which resulted in a decrease in total heat release.

PBT is used for various insulating parts in the electrical and electronic industries, like lamp holders, switches, circuit breakers, and motor casings. It has high heat resistance, good mechanical strength, water resistance, and excellent electrical insulating properties [100]. However, pure PBT is highly combustible, so it is necessary to improve its fire retardancy to meet the fire safety requirements of electrical and electronic applications. GF is added into PBT to help prevent dripping and maintain integrity when burning. However, PBT/GF is more flammable than pure PBT due to the wick effect. Phosphorus-based additives are added into PBT to improve the fire resistance and are found to be very effective in both the condensed-phase by promoting char formation and gas-phase by inhibiting the flame [101–103]. The introduction of

melamine derivatives as a synergist with phosphorus flame retardants was found to further contribute to the fire resistance of the polymer matrix [102,104,105]. Braun et al. [103] investigated the effects of different flame retardants on the pyrolysis and fire behavior of PBT/GF by means of TGA-infrared spectroscopy and cone calorimeter tests as well as scanning electron microscopy. It was found that PBT/GF, flame retardant with DEPAL and melamine cyanurate, achieves a V-0 classification in UL 94 test and has an increased LOI of 44%.

Most of the previous studies of flame retardant materials focused on the qualitative or semi-quantitative analysis of the thermal decomposition and combustion behavior [92,96,99,103,105–109]. None of them can provide a quantitative understanding of the relation between the fire behavior and material composition. Knowledge of this relation allows for intelligent design of flame retardant materials with optimized fire resistance and other excellent mechanical properties. Therefore, in this work, special attention has been focused on the development of a condensed-phase pyrolysis model that quantitatively relates the flame retardant contents to the fire behavior.

1.3 Objective and Current Approach

The present research seeks to characterize flame retardant materials for the development of pyrolysis models that quantitatively relate the flame retardant contents to fire behavior of flame retardant materials. Relating the fire behavior to material composition enables informed design of flame retardant materials with optimized fire performance while maintaining optimal mechanical properties. A combined

experimental and modeling methodology is detailed to estimate the model inputs (material properties) for the development of comprehensive pyrolysis models of flame retardant materials. Two sets of widely used flame retardant materials (PA66/GF/RP blends and PBT/GF/DEPAL/MPP blends) are examined in this work to demonstrate the generality of the methodology [110–113].

The methodology employs milligram-scale experiments (TGA, DSC, and MCC) to measure the sample mass loss, the heat required to decompose the sample, and the heat released from the complete combustion of the gaseous products evolved during the sample decomposition. The small sample mass and low heating rate used in the milligram-scale experiments facilitate decoupling the chemical reactions from the mass and thermal transport processes. Through an inverse analysis of the TGA, DSC, and MCC measurements using a fully verified and validated numerical pyrolysis framework, ThermaKin2Ds, the decomposition kinetics and thermodynamics, and heats of complete combustion of gaseous pyrolyzate released from decomposition are determined. The decomposition kinetics and thermodynamics include the reaction kinetics, heat capacities of condensed-phase reactants and products, and heats of decomposition or melting. The extrapolating capability of the developed reaction model is validated against data collected at different heating conditions and for blends with new material compositions that differ from those employed in the model calibration.

The methodology also relies on a new controlled atmosphere pyrolysis apparatus II (CAPA II) to simultaneously measure the MLR, back surface temperature, and sample shape profile evolution of pyrolyzing samples exposed to well-defined radiant

heating. CAPA II has been developed to enable carefully controlled gasification experiments of intumescent and charring materials through a joint effort between several colleagues. Interpretation of the CAPA II measurements using the reaction model and ThermaKin2Ds yields the properties that define heat and mass transport in the pyrolyzing samples. A complete pyrolysis model is developed using the resulting reaction model and thermal and mass transport properties. The extrapolating capability of the pyrolysis model is examined against data obtained at different external heating conditions and for blends with new compositions that are outside of those used in the model calibration.

Additionally, idealized cone calorimetry simulations are conducted to demonstrate the action of flame retardants on the fire performance of a material based on the heats of combustion of gaseous products obtained in MCC and the developed pyrolysis model. To the best of my knowledge, it is the first time that a quantitative relation between the fire behavior and material composition has been developed for multi-component flame retardant systems. This work is critical for intelligent design of flame retardant materials with optimal fire resistance and other optimal properties tailored for specific applications.

Chapter 2. Materials

2.1 PA66/GF/RP Blends

The glass fiber reinforced polyamide 66 mixed with red phosphorus tested in this work was provided by BASF. The compounds were mixed and produced on a twin-screw extruder. The extrudate was pulled through a water bath for cooling prior to becoming granulated. Samples for gasification tests were prepared via injection molding [114] into 3.8 mm thick plates.

The formulation name and composition of PA66-based blends are shown in Table 2.1. These materials were selected to represent a range of compositions that are commonly encountered in industrial and commercial applications. Three blends, PA66/GF25, PA66/GF25-RP1.5, and PA66/GF-RP6.0, were employed to develop the reaction mechanism. Glass fiber was assumed to be chemically inert. PA66, PA66/GF25-RP3.0, PA66/GF-RP4.5, and PA66/GF-RP9.0 were used to validate the developed reaction mechanism. The first four blends in Table 2.1 were employed to develop the pyrolysis model that was built on the foundation of the developed reaction mechanism. Two blends with new compositions, PA66/GF-RP4.5 and PA66/GF-RP9.0, were used to validate the pyrolysis model. It should be noted that PA66 was also included in the pyrolysis model development to enable the parameterization of the thermal transport properties of PA66 and the physical interaction between PA66 and GF when developing the pyrolysis model.

The samples for TGA, DSC, and MCC tests were prepared by either cutting or grinding the plates into 3-7 mg specimens. Each test was repeated multiple times using

varying sample mass and shape to verify that the test results were not sensitive to these factors and thus ensure thermally thin behavior (no significant temperature or composition gradients within the sample). The samples for gasification tests were prepared by cutting the 3.8 mm thick plate with a computer numerical control milling machine into a circle with a diameter of 0.07 m. The samples were further machined to have a thickness on the order of 1×10^{-3} m for broadband radiation absorption measurements. All samples were conditioned in a desiccator in the presence of Drierite for a minimum of 48 hours prior to testing to obtain measurements with negligible contribution from moisture.

Table 2.1 PA66-based materials tested in this study.

	Formulation Name	PA66 (wt.%) A24 *	GF (wt.%) OCF DS 1110 *	RP (wt.%)
Model Development	PA66	100	0	0
	PA66/GF25	75	25	0
	PA66/GF25-RP1.5	73.5	25	1.5
	PA66/GF25-RP6.0	69	25	6.0
Model Validation	PA66/GF25-RP3.0	72	25	3.0
	PA66/GF25-RP4.5	70.5	25	4.5
	PA66/GF25-RP9.0	66	25	9.0

* Commercial name

2.2 PBT/GF/DEPAL/MPP Blends

Glass fiber reinforced polybutylene terephthalate mixed with aluminum diethyl phosphinate and melamine polyphosphate blends tested in this work were provided by BASF. They were produced by first mixing the polymer matrix and additives and then

extruding the mixture into 3.8 mm thick plates in the same manner as described in Section 2.1. The formulation name and composition of the PBT-based materials are shown in Table 2.2. Five blends, PBT/GF25, PBT/GF25-DEPAL8, PBT/GF25-DEPAL16, PBT/GF25-MPP4, and PBT/GF25-MPP8, were employed to develop the reaction mechanism. Glass fiber was assumed to be chemically inert. PBT, PBT/GF25-DEPAL8-MPP4, and PBT/GF25-DEPAL16-MPP8 were subsequently used to validate the reaction mechanism. The first six blends in Table 2.2 were employed to develop the pyrolysis model. The last two blends in Table 2.2, PBT/GF25-DEPAL8-MPP4 and PBT/GF25-DEPAL16-MPP8, were used to validate the pyrolysis model. It is noted that PBT was also included in the pyrolysis model development, unlike the reaction mechanism development, to enable the parameterization of the thermal transport properties of PBT and the physical interaction between PBT and GF when developing the pyrolysis model.

The samples for TGA, DSC, and MCC tests were prepared by either cutting or grinding the plates into 3-7 mg specimens. Each test was repeated multiple times using varying sample mass and shape to verify that the test results were not sensitive to these factors and thus ensure thermally thin behavior (i.e., no significant temperature or composition gradients within the sample). The samples tested in gasification tests were carefully cut with a computer numerical control milling machine to have a diameter of 0.07 m and a thickness of 3.8 mm. All samples were conditioned in a desiccator in the presence of Drierite for a minimum of 48 hours prior to testing to ensure negligible contributions from moisture.

Table 2.2 PBT-based materials tested in this study.

	Formulation Name	PBT Ultradur B4500* (wt. %)	GF Glass fiber PPG 3786* (wt. %)	DEPAL Exolit OP 1240* (wt. %)	MPP Melapur 200* (wt. %)
Model Development	PBT	100	0	0	0
	PBT/GF25	75	25	0	0
	PBT/GF25-DEPAL8	67	25	8	0
	PBT/GF25-DEPAL16	59	25	16	0
	PBT/GF25-MPP4	71	25	0	4
	PBT/GF25-MPP8	67	25	0	8
Model Validation	PBT/GF25-DEPAL8-MPP4	63	25	8	4
	PBT/GF25-DEPAL16-MPP8	51	25	16	8

* Commercial name

Chapter 3. Experimental Methods

3.1 Milligram-scale Experiments

3.1.1 Simultaneous Thermal Analysis (STA)

A Netzsch 449 F3 Jupiter Simultaneous Thermal Analyzer was employed to conduct TGA and DSC tests simultaneously. This apparatus combines a TGA instrument equipped with a 1 μg-resolution microbalance and a heat flux DSC implemented using a Netzsch TGA-DSC sample carrier equipped with P-type thermocouples. Figure 3.1 depicts a schematic of the STA. More information on the design of the 449 F3 Jupiter STA can be found in the manufacture's brochure [115].

All STA tests followed a carefully prescribed temperature program. The temperature program for these tests had a conditioning period in which the sample was maintained at 313 K for 25 min, followed by a linear heating up to 873 K. The majority of the tests were conducted at a nominal heating rate of 10 K min^{-1} (0.167 K s^{-1}) to ensure that the heating rate was sufficiently low to decouple the chemical reactions from the mass and thermal transport. The tests were performed in an anaerobic environment established by continuously purging the analyzer's furnace with nitrogen at a rate of 50 mL min^{-1}. Platinum-Rhodium crucibles with lids were utilized in all tests to maximize temperature uniformity and heat flow sensitivity. The lids had a small opening for ventilation to allow gaseous pyrolyzate to escape the crucible. It was shown in a previous study [45] that the lid does not interfere with the transfer of gaseous decomposition products out of the crucible. The mass and heat flow data were collected simultaneously as a function of time and sample temperature.

The temperature and heat flow sensors of this instrument were calibrated using a set of seven organic and inorganic compounds with known melting points and heats of melting. The temperature calibration provided a relation between the measured and actual sample temperatures. The heat flow sensors calibration provided a conversion between the difference in the voltage generated by the sample crucible and the reference crucible, and the actual sample heat flow. The calibration tests were performed under the same test conditions (temperature program, flow rate, and type of crucible) as those utilized in the majority of actual experiments. The stability of the calibrations were checked once a month and the apparatus was completely recalibrated every 3 months.

Each sample test was preceded by a baseline test where the empty sample and reference crucibles were subjected to the same heating program as the actual test. The mass and heat flow data of the baseline were subtracted from the corresponding data obtained from the actual sample test. All the TGA and DSC data presented in this work have been baseline corrected. A detailed description of the instrument calibration and testing protocol can be found in an earlier publication [45].

The STA tests of both PA66-based and PBT-based blends employed in the reaction mechanism development were conducted at 10 K min^{-1} and repeated ten times to ensure reproducibility and accumulate necessary statistics. Additional TGA-only tests (no heat flow signal was collected) of these blends were performed at 5 K min^{-1} and 20 K min^{-1}. These TGA-only tests were repeated three times and were used to verify that the developed reaction model correctly extrapolated the material's behavior to alternate thermal conditions. Only TGA tests on the remaining PA66-based blends

used for reaction model validation were conducted at 10 K min^{-1} and repeated three times. The STA tests on the remaining PBT-based blends used for reaction model validation were conducted at 10 K min^{-1} and repeated five times to produce reliable DSC data. The TGA tests of MPP were performed at 10 K min^{-1} in triplicate. The mass and heat flow data obtained from repeated tests were averaged prior to use to minimize random errors.

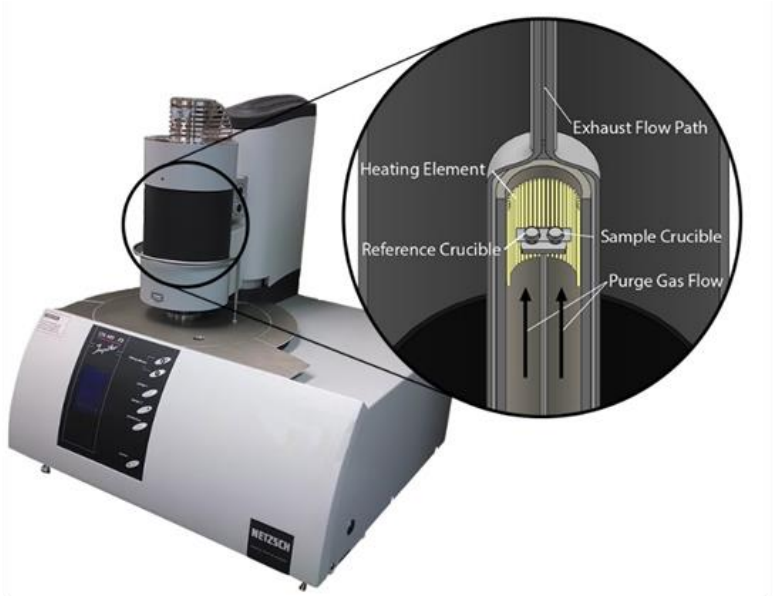

Figure 3.1 Schematic of Simultaneous Thermal Analysis.

3.1.2 Microscale Combustion Calorimetry (MCC)

MCC is a standardized test method used to measure the heat release rate (HRR) from complete combustion of gaseous products evolved from a pyrolyzing solid. Figure 3.2 shows a schematic of Microscale Combustion Calorimeter. The primary components of this apparatus consist of a pyrolyzer and a combustor. The MCC tests were performed at the same prescribed heating rate of 10 K min^{-1} as used in STA tests to enable a direct comparison with the STA measurements. A slightly higher

temperature of 348 K was set as the initial temperature. All the samples were pyrolyzed in a ceramic crucible without a lid in nitrogen at a flow rate of 80 mL min^{-1}. The gaseous pyrolyzate was purged by nitrogen into the combustor, where the pyrolyzate was mixed with excess oxygen, supplied at a flow rate of 20 mL min^{-1}, and oxidized. The temperature of the combustor was set at 1173 K to ensure complete combustion. The heat released from the combustion process was measured using the principle of oxygen consumption [83]. The HRR was recorded as a function of time and pyrolyzing sample temperature. A detailed description of the MCC method can be found elsewhere [83].

The MCC apparatus was carefully calibrated on a monthly basis following the recommended procedures [83]. A temperature calibration that relied on the melting point of several pure metals (Indium, Lead, Zinc, and Aluminum) was conducted to ensure accurate sample temperature measurements. The oxygen sensor was calibrated against a standard O_2/N_2 mixture to ensure accurate HRR measurements. Polystyrene tests were conducted prior to the sample test to ensure the stability of the instrument. MCC tests were subsequently performed on the materials used in the reaction model development. Each test was repeated three times due to their high reproducibility. The HRR data obtained from repeated tests were averaged prior to further analysis.

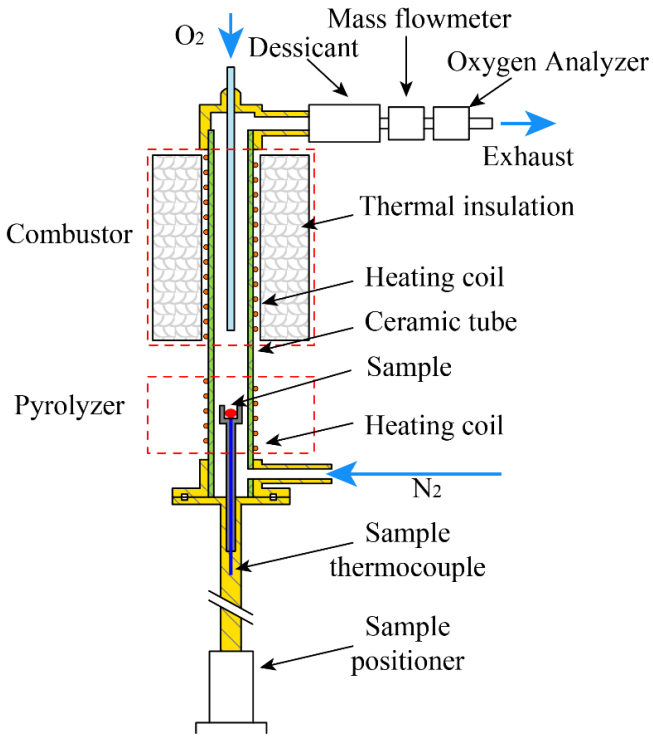

Figure 3.2 Rendering of the Microscale Combustion Calorimeter.

3.2 Bench-scale Experiments

3.2.1 Broadband Radiation Absorption

The broadband radiation absorption coefficient measurement was based on a methodology described by Linteris et al. [62], which was adopted in several additional studies [78,82,116]. The method involved irradiating a material specimen with a thickness about 1×10^{-3} m, at a well-defined radiant flux from an electric conical heater. The radiation flux transmitted through the sample was measured with a Schmidt-Boelter heat flux gauge (1.2×10^{-2} m diameter). A schematic of the measurement setup is provided in Figure 3.3. The radiation was collimated by Kaowool PM insulation board with a cylindrical hole in the center, comparable in size to the diameter of the heat flux gauge, to direct the light waves through the sample specimen.

The heater was set at a temperature of 940 K that corresponded to the radiant heat flux of 45 kW m^{-2} to the sample surface in the gasification experiment, described in Section 2.3. The sample was positioned 0.07 m below the base of the heater housing and the heat flux gauge was positioned directly below the sample.

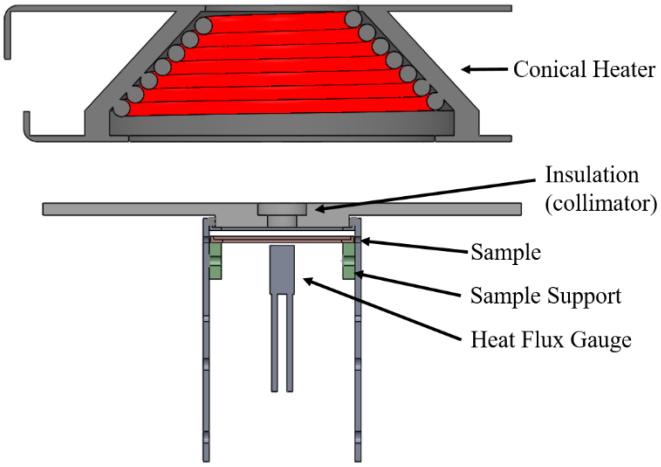

Figure 3.3 Schematic of apparatus to measure the absorption coefficient.

The incident radiation flux to the heat flux gauge was first measured for 30 s, with the sample removed. After 30 s, the sample was placed under the insulation and the transmitted flux was measured for the first 3 s of sample radiation exposure to ensure the conduction through the sample did not contribute significantly to the measurement. Each test was performed in duplicate to accumulate necessary data statistics. The averaged data collected in these measurements were used to calculate the effective absorption coefficient with Eq. (3.1), adapted from [62]. In Eq. (3.1), κ is the absorption coefficient, ρ is the density measured at room temperature, and δ is the sample thickness. x is the coordinate parallel to the direction of the heat flow. ε represents the sample surface emissivity, which was obtained based on literature data.

$I_{x=\delta}$ and $I_{x=0}$ are the radiation measured by the heat flux gauge through the sample and with the sample removed, respectively.

$$\kappa = \frac{2\ln(\varepsilon) - \ln(\frac{I_{x=\delta}}{I_{x=0}})}{\rho\delta} \quad (3.1)$$

3.2.2 Controlled Atmosphere Pyrolysis Apparatus II (CAPA II)

The CAPA II, as depicted in Figure 3.4, is a newly designed gasification instrument that enables carefully controlled pyrolysis of intumescent and charring materials. CAPA II consisted of an electrical radiant conical heater, a gasification chamber, a balance, an infrared camera, and a video camera. The electric radiant heater, capable of providing up to 100 kW m^{-2} heat flux, was positioned on a moving track to enable its fast placement and removal from above the gasification chamber. Inside the gasification chamber, there is a steel sample holder with an inner diameter of 82 mm. Figure 3.5 shows the top-view of the gasification chamber and cross-section of CAPA II. The chamber was constructed from two concentric, circular, aluminum tubes that were water-cooled. The top of the outer tube was located 0.03 m above the initial sample surface and 0.01 m below the bottom of the radiant heater housing to minimize the entrainment of ambient air. The inner wall of the outer aluminum tube was coated with a high emissivity paint to suppress reflections of the heater's radiation. A continuous flow of gas was introduced to the apparatus within the channel between the aluminum tubes. The gas was purged through a layer of glass beads with a diameter of 6.4 mm to ensure a homogenized flow. The gas composition can be prescribed.

Material samples of 0.03 to 0.07 m in diameter and 1 to 20 mm in thickness can be accommodated within the apparatus. Kaowool PM insulation board was used to

thermally insulate the samples around the perimeter, as detailed in Figure 3.5. A piece of 0.76 mm thick, diamond-shaped aluminum mesh covered with a thin (0.025 mm) copper foil supports the bottom of the sample. The sample, thermal insulator, aluminum mesh and copper foil were all contained within the sample holder.

The CAPA II diagnostics include three main components: sample mass, back surface temperature, and sample shape profile. The instantaneous sample mass was recorded using a high precision (1 mg resolution) Sartorius Cubis balance at a frequency of 2 Hz. A FLIR E40 infrared camera was focused on the thin painted copper foil holding the sample to measure the back surface temperature at a frequency of 7.5 Hz. The foil was coated with a high (0.94) emissivity paint to ensure accuracy of this measurement. Due to geometrical constraints, a gold mirror (with average reflectance of 0.96) was used to provide the view to the back of the sample. The emissivity in the infrared camera has been adjusted to account for the transmission loss in the gold mirror, and was validated against thermocouple based temperature measurements. A Logitech C930e high definition camera was focused on the sample through a quartz observation window to monitor evolution of the sample shape profile. Independent measurements were performed with 3 thermocouples positioned within the channel between the aluminum tubes and above the glass beads, to obtain the averaged gas temperature at each prescribed heat flux.

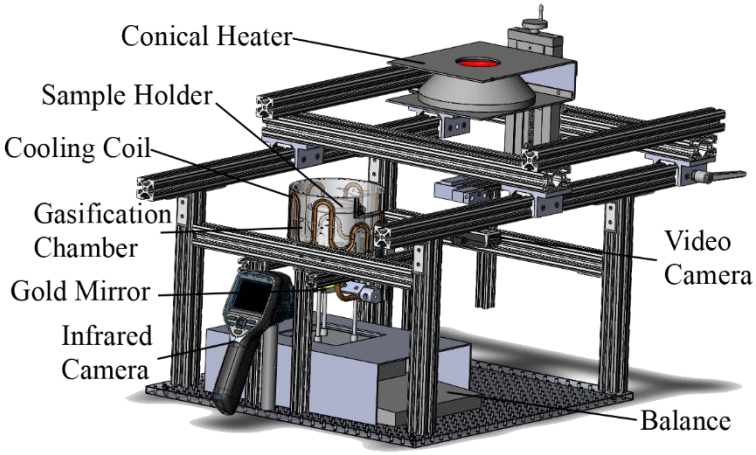

Figure 3.4 Three-dimensional drawing of CAPA II

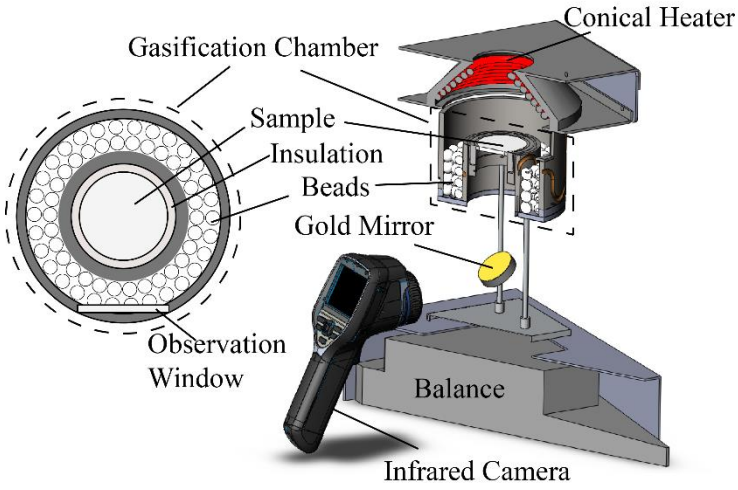

Figure 3.5 Top-view of the gasification chamber (left) and cross-section of CAPA II (right)

The apparatus provided well-defined boundary conditions. The gasification chamber was purged with nitrogen at a constant flow rate of 185 SLPM at 298 K and 101 kPa. At this flow rate, the mean oxygen concentration in the pyrolysis zone was controlled to below 1 vol.% to ensure that the measurements were free of oxidation effects. A detailed quantification of the gaseous condition was provided in a previous study [117].

The incident radiative heat flux from the conical heater was carefully characterized using a water-cooled Schmidt-Boelter heat flux gauge to account for changes in the sample surface position, including the surface's angular orientation. The incident radiation measurements were performed at a series of vertical distances h_x from the initial top sample surface position. At each distance h_x, the heat flux was measured at several horizontal radial distances from the sample's center (r_z). Most measurements were performed with the gauge's sensor facing straight upward. However, a subset of measurements were conducted with the sensor positioned at several polar angles (θ) to capture the impact of local surface orientation. h_x was normalized by the distance from the sample surface to the bottom of the heater housing, H=0.04 m. r was normalized by the initial sample radius, R=0.035 m. The results of the dependence of the incident radiative heat flux (q'') measurements on surface position are summarized in Eq. (3.2).

$$\frac{q''\left(\frac{h_x}{H},\frac{r_z}{R},\theta\right)}{q''\left(\frac{h_x}{H}=0,\frac{r_z}{R}=0,\theta=0\right)} = \left(a_2\left(\frac{r_z}{R}\right)^2 + a_1\left(\frac{r_z}{R}\right) + 1\right)\left(b_2\left(\frac{h_x}{H}\right)^2 + b_1\left(\frac{h_x}{H}\right) + 1\right)(g_2\theta^2 + g_1\theta + 1) \quad (3.2)$$

In this equation, a_2 and a_1 coefficients were used capture the radial trends. b_2 and b_1 coefficients were used to capture the axial trend. g_2 and g_1 coefficients were vertical distance dependent coefficients used to capture the angular trends. $a_2 = a_{22}(h_x/H)^2 + a_{21}(h_x/H) + a_{20}$ and $a_1 = a_{12}(h_x/H)^2 + a_{11}(h_x/H) + a_{10}$ where a_{22} =0.126, a_{21} =0.040, a_{20} =-0.044, a_{12} = -0.088, a_{11} =0.092 and a_{10} =-0.008, b_2 = -0.393 and b_1 = 0.438 coefficients are used to capture the axial trend. c_2 and c_1 are vertical distance dependent coefficients: $g_2 = c_{22}(h_x/H)^2 + c_{21}(h_x/H) + c_{20}$

and $g_1 = c_{12}\,(h_x/H)^2 + c_{11}\,(h_x/H) + c_{10}$, where $c_{22} = -0.191$, $c_{21} = -0.136$, $c_{20} = -0.029$, $c_{12} = 0.482$, $c_{11} = 0.261$, and $c_{10} = -0.440$.

Eq. (3.2) provided a capability to compute the incident radiant heat flux distribution for an intumescent material sample from a known heat flux set point. Variation of this set point from 30 to 70 kW m^{-2} was examined. It was found that the mean difference between the model prediction and measured heat fluxes was about 1%, regardless of the set point selection. The convective heat losses on the top and bottom sample surface were quantified through detailed simulations and further validated against experimental measurements, which is detailed in Section 4.2. It is noted that the instantaneous gas temperatures were quantified and used for convective heat flux calculations.

In this work, the CAPA II tests on PBT-based samples were conducted at nominal radiative heat fluxes of 30, 45, and 60 kW m^{-2}. The gasification tests of the six blends employed for calibration (PBT, PBT/GF25, PBT/GF25-DEPAL8, PBT/GF25-DEPAL16, PBT/GF25-MPP4, and PBT/GF25-MPP8) were conducted at both 30 kW m^{-2} and 60 kW m^{-2}. The gasification tests of two blends (PBT/GF25-DEPAL8-MPP4 and PBT/GF25-DEPAL16-MPP8) employed to examine its extrapolating capability, were performed at an intermediate heat flux of 45 kW m^{-2}. The experiment was terminated when no significant mass loss was observed. The sample shape profile evolutions of PBT-based samples showed that the surfaces of all the studied samples remained uniform across the radius during the pyrolysis process. The thickness of pure PBT reduced to almost zero at the conclusion of the test. The thicknesses of PBT/GF25, PBT/GF25-DEAPL8, and PBT/GF25-DEPAL16 remained approximately constant

throughout the CAPA II tests. The thicknesses of PBT/GF25-MPP4 and PBT/GF25-MPP8 increased by approximately 3 mm and 3.5 mm at about 150 s and then remained unchanged until the end of the tests.

The CAPA II tests on PA66-based samples were conducted at nominal radiative heat fluxes of 30, 40, 45, and 60 kW m^{-2}. The decomposition of pure PA66 was only examined at 60 kW m^{-2} because the results at the lower heat flux were found to be poorly reproducible. The gasification tests of PA66/GF25 were conducted at both 30 kW m^{-2} and 60 kW m^{-2}. The gasification tests of PA66/GF25-RP1.5 and PA66/GF25-RP6.0 were performed at 40 kW m^{-2} and 60 kW m^{-2}. The RP-containing blends required a heat flux of 40 kW m^{-2} instead of 30 kW m^{-2} because the thermal stability of the RP-containing blends was higher than that of PA66/GF25. The gasification tests of PA66/GF25-RP4.5 and PA66/GF25-RP9.0 were performed at 45 kW m^{-2}. The examination of the sample shape profiles revealed that the sample surface remained nearly flat and the sample thickness did not change significantly ($<$ 3 mm) throughout the pyrolysis tests.

Therefore, a 1D assumption was made when simulating the gasification tests, given the flat sample surface and small changes in sample thickness for all blends. The radiative and convective heat fluxes at the middle point ($r_z/R = 0.5$) were used as the averaged values across the sample radius in the simulations. The back surface temperature measurements at r_z/R = 0, 0.29, 0.57, and 0.86 were found to be similar and they were averaged and employed as the inverse modeling target. Each test was performed in duplicate to ensure reproducibility and to accumulate necessary data statistics. The MLR was computed using a 5 s time differential and normalized by the

initial top surface area of the sample. The data were subsequently grouped into 5 s bins for which mean MLR and mean time values were computed. The temperature and MLR data from repeated tests were grouped together prior to averaging.

Chapter 4. Numerical Framework – ThermaKin2Ds

4.1 Governing Equations

ThermaKin [36] was first developed to compute the transient rate of gaseous fuel production from fundamental physical and chemical properties of constituents of a 1D pyrolyzing solid. ThermaKin was later expanded into a two-dimensional (2D) pyrolysis solver, ThermaKin2D [118], which incorporated a flexible analytical representation of flame spread. A new fully verified and validated numerical framework, ThermaKin2Ds [116], was developed to emulate the CAPA II cylindrical geometry (2D axisymmetric) and to simulate the gasification experiments.

ThermaKin2Ds accounts for chemical reactions (chemical mechanisms of arbitrary complexity can be modeled), transient conduction (governed by temperature-dependent properties), in-depth thermal radiation absorption and emission, mass transport of gaseous species through the condensed-phase, and expansion or contraction of the pyrolyzing object. The material is represented by a mixture of components. By default, the maximum number of components is restricted to 50. All components are divided into 3 categories: solids, liquids, and gases. Every component is characterized by density, heat capacity, thermal conductivity, a gas transfer coefficient, emissivity, and a radiation absorption (or extinction) coefficient. The first four properties are defined by a flexible function of temperature, T, given by Eq. (4.1).

$$\text{property} = p_0 + p_1 + p_n T^n \tag{4.1}$$

Where p_0, p_1, p_n, and n are user-specified parameters. The emissivity and absorption coefficient are defined by single (constant) values.

Chemical reactions are defined in ThermaKin2Ds as occurring between one or two components to produce zero to two components, given by Eq. (4.2).

$$\theta_1 \mathrm{COMP1} + \theta_2 \mathrm{COMP2} \rightarrow \theta_3 \mathrm{COMP3} + \theta_4 \mathrm{COMP4} + h_i \tag{4.2}$$

θ_1 to θ_4 denote the stoichiometric mass coefficient, which is negative when component is the reaction's reactant and positive when it is this reaction's product. The subscript i represents the i-th reaction. h_i is the temperature dependent heat released or absorbed for each chemical reaction or phase transition, which can be defined as a temperature-dependent quantity with Eq. (4.1). h_i is positive when the reaction is endothermic. The Arrhenius reaction rate, r_i, is defined in Eq. (4.3)

$$r_i = A_i \exp\left(-\frac{E_i}{R_u T}\right) \xi_{\mathrm{COMP1}} \xi_{\mathrm{COMP2}} \tag{4.3}$$

A_i and E_i are the Arrhenius pre-exponential factor and activation energy for reaction i. R_u is the universal gas constant. ξ_{COMP1} and ξ_{COMP2} represent the mass concentration of reactants. In the absence of the second reactant, ξ_{COMP2} is set to 1. Eq. (4.4) provides the mass conservation for the j-th component in terms of the mass concentration of the component. In the 2D axisymmetric module, a material object is defined using the cylindrical coordinates x (axial) and z (radial). The mass conservation accounts for consumption or production of j-th component due to chemical reactions, mass transport of gaseous products (labeled with subscript g) within the condensed-phase given by Eq. (4.5) (in both axial and radial directions), and mass transport

associated with contraction or expansion of the material with respect to a stationary boundary (x = 0). No expansion or contraction is allowed in the radial (z) direction.

$$\frac{\partial \xi_j}{\partial t} = \sum_{i=1}^{N_r} \theta_i^j r_i - \frac{\partial {J_j}^x}{\partial x} - \frac{1}{z}\frac{\partial (z{J_j}^z)}{\partial z} + \frac{\partial}{\partial x}\left(\xi_j \int_0^x \frac{1}{\rho}\frac{\partial \rho}{\partial t} dx\right) \quad (4.4)$$

$${J_g}^x = -\rho_g \lambda \frac{\partial (\xi_g/\rho_g)}{\partial x}; {J_g}^z = -\rho_g \lambda \frac{\partial (\xi_g/\rho_g)}{\partial z} \quad (4.5)$$

Where t and N_r represent the time and the number of reactions. λ is the gas transfer coefficient. It is noted that only gaseous components are considered to be mobile and λ does not depend on the nature of the gas that is being transferred. The thermo-physical properties without subscripts correspond to the property of a mixture, and are calculated as either volume- or mass-weighted sums of the properties of each component [36].

Eq. (4.6) represents the energy conservation in terms of temperature. The energy conservation accounts for heat flow due to thermal degradation reactions and phase transitions, and heat conduction within the condensed-phase, defined in Eq. (4.7) (in both axial and radial directions). The energy conservation also accounts for absorption of radiant heat from external sources, defined in Eq. (4.8), radiant heat loss from the material to the environment, defined in Eq. (4.9), convective heat transfer due to gas transport, and energy flow associated with contraction or expansion of the material with respect to a stationary boundary (x = 0).

$$\sum_{j=1}^{N} \xi_j c_j \frac{\partial T}{\partial t} = \sum_{i=1}^{N_r} h_i r_i - \frac{\partial q_x}{\partial x} - \frac{1}{z}\frac{\partial (z q_z)}{\partial z} - \frac{\partial I_{ex}}{\partial x} + \frac{\partial I_{rr}}{\partial x} - \sum_{g=1}^{N_g} c_g \left({J_g}^x \frac{\partial T}{\partial x} + {J_g}^z \frac{\partial T}{\partial z}\right) + c\rho \frac{\partial T}{\partial x}\int_0^x \frac{1}{\rho}\frac{\partial \rho}{\partial t} dx \quad (4.6)$$

$$q_x = -k\frac{\partial T}{\partial x};\ q_z = -k\frac{\partial T}{\partial z} \tag{4.7}$$

$$\frac{\partial I_{ex}}{\partial x} = -I_{ex}\sum_{j=1}^{N}\kappa_j\xi_j \tag{4.8}$$

$$\frac{\partial I_{rr}}{\partial x} = \frac{\varepsilon\sigma T^4}{I_{ex}^0}\frac{\partial I_{ex}}{\partial x} \tag{4.9}$$

The symbols in Eqs. (4.6-4.9) are defined as follows: N represents the number of components, c is the heat capacity, k is the thermal conductivity, κ is the absorption coefficient, and ε is the emissivity. I_{ex} is the radiation flux absorbed by the sample (including in-depth) from external sources. The superscript 0 in I_{ex}^0 denotes net external radiation flux through the material boundary (incident flux minus reflected), and σ is the Stefan-Boltzmann constant. I_{rr} is radiant heat loss from the material to the environment. A more detailed explanation of the terms of the governing equations, as well as their numerical solution methodology, can be found in earlier publications [36,116,118].

These equations rely on the assumptions that the radiative exchange between the material object and environment only occurs in the axial direction and that the rate of local heat transfer between gases and condensed-phase components is infinitely fast. The latter assumption is implemented in the convective heat flow terms (sixth right-hand-side terms in Eq. (4.6)). An approximate finite rate correction to this assumption can be made by scaling gas heat capacities (c_g) downward from their actual values. The last right-hand-side term in Eq. (4.6) accounts for the heat transfer associated with contraction or expansion of the material object with respect to a stationary boundary (x

= 0). It is also assumed that the momentum from the gases transported in the solid material is negligible.

4.2 Boundary Conditions

The boundary condition specification in ThermaKin2Ds is subdivided into three object geometries: 1D, 2D, and 2D axisymmetric. The boundary conditions defined for 1D and 2D objects are the same as those in ThermaKin [36] and ThermaKin2D. [118]. All the geometries share the same description of mass transport at the boundary. The mass transport boundary conditions are defined to enable the mass transport between the sample and surroundings. The mass transport at the boundary is specified with a linear function generally used to remove gaseous pyrolyzate from the solid sample surface. Alternatively, an exponential function may be applied as the boundary condition to simulate surface reactions (such as oxidation) or dripping [36].

The external heat flux (radiative or convective) is defined using a piecewise-linear spatial distribution function analogous to the 2D object [118]. An additional external heat flux module is provided to enable modeling of pyrolysis experiments in the CAPA II [117] through accounting for the effects of sample surface changes on the radiation and convection. The dependence of incident radiative heat flux on the sample surface changes was characterized in Section 3.2.2. The dependence of convective heat flux on the sample surfaces is characterized through computational fluid dynamics (CFD) calculations and provided later in this section. This additional CAPA II module can be turned on and off at user-specified times. All external and CAPA II heat fluxes are added together.

CFD calculations have been conducted to analyze convective heat transfer at the sample surfaces. The calculations were performed using the Fire Dynamics Simulator (FDS) version 6.2.0 [119] in the direct numerical simulation mode with the radiation sub-model turned off. An axisymmetric computational domain, built to represent the CAPA II gasification chamber, is shown in Figure 4.1.

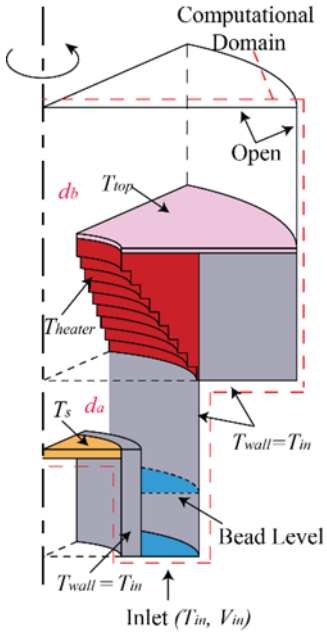

Figure 4.1 Schematic of CFD model of CAPA II

A series of scenarios representative of those likely to be encountered in the gasification experiments have been explored in these calculations. In all scenarios, the inlet flow temperature and velocity (T_{in} = 363 K and V_{in} = 0.348 m s^{-1}) and the temperatures of the heater and the plate on the top of heater (T_{heater} = 999 K and T_{top} = 423 K) were specified to correspond to those measured in the experiments conducted at 51.5 kW m^{-2} heat flux set point. The sample surface temperature (T_s) and sample shape were varied from scenario to scenario as indicated in Table 4.1 and Figure 4.2. Nitrogen was defined as the gaseous media in all scenarios with the exception of #6,

where air was used instead. Scenario #6 was employed to analyze convective losses from the bottom sample surface. Thus, the choice of gaseous media reflects the fact that, in the CAPA II, the enclosure containing this bottom surface is not purged with nitrogen.

The convective heat flux, q_c'', was calculated as the product of the gas temperature gradient taken along a direction orthogonal to the sample surface (using the grid points nearest to the sample surface) and the thermal conductivity of the gas at the film temperature. The dots shown in Figure 4.2 depict locations where q_c'' values were computed. To increase computational efficiency, the computational domain was subdivided into two parts, as shown in Figure 4.1. d_a and d_b represent the grid size in the region below and above the bottom of the heater, respectively. A grid convergence study was conducted using scenario #3 (corresponding to the highest sample surface temperature). It was determined that selecting 0.25 and 0.5 mm grid sizes for d_a and d_b, respectively, produces q_c'' values that are within 3% of those computed using a much finer, 0.125 mm sized grid.

Table 4.1 Summary of input parameters used in the CFD calculations. Slope represents the ratio of maximum height versus radius of the top sample surface for scenarios #1-5 and the bottom surface for scenario #6.

Scenario #	T_s (K)	Slope
1	500	0
2	700	0
3	900	0
4	700	0.5
5	700	1.0
6	600	0

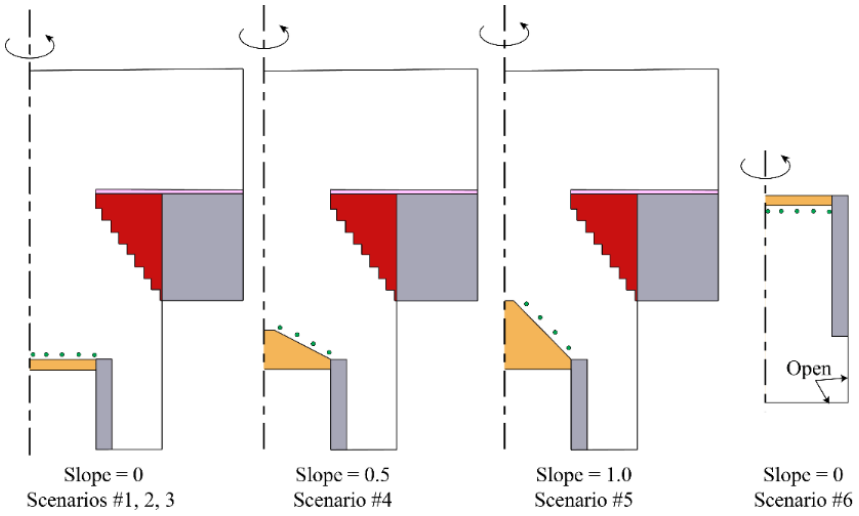

Figure 4.2 Scenarios explored in the CFD calculations. Slope represents the ratio of maximum height versus radius of the sample surface. The dots depict locations where q_c'' values were computed

The CFD simulations of each scenario were carried out for 18 s. Scenarios #2-5 displayed oscillating flows; thus, the duration of the simulations was selected to reveal the periodic character fully. A set of temperature distribution snapshots taken over one oscillation period for scenario #3 are shown in Figure 4.3. It appears that, despite significant forced flow through the gasification chamber, near the sample's surface, the flow is driven primarily by buoyancy and the observed oscillation is a manifestation of the Rayleigh–Taylor instability.

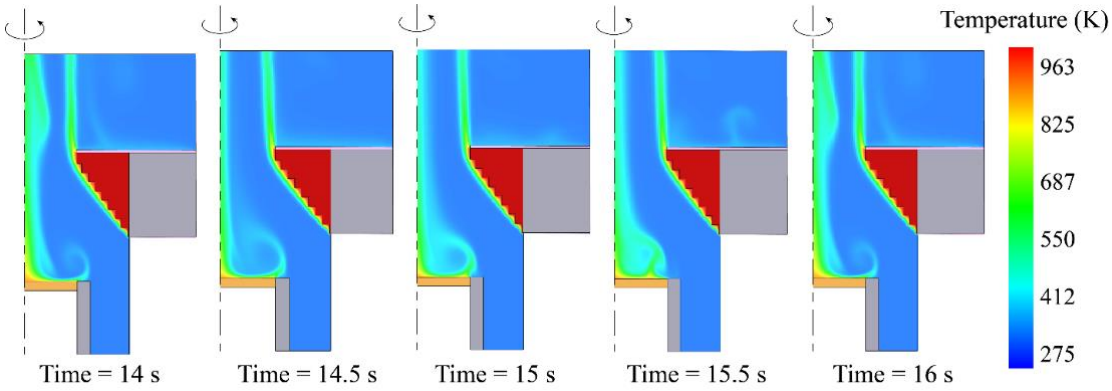

Figure 4.3 Oscillating temperature profile in one period (14 – 16 s) obtained for scenario #3

The convective heat fluxes computed for scenario #3 at two representative radial positions (r_z/R = 0.286 and r_z/R = 0.857) are shown in Figure 4.4. To convert these heat fluxes to convection coefficients, they were first averaged in time over the oscillation period (or over 5 s in the cases of non-oscillating flows). To examine the impact of surface temperature on the convection, the convection coefficients obtained for the scenarios where this temperature was varied (scenarios #1, 2 and 3) were further averaged over the top sample surface area using Eq. (4.10):

$$\bar{h}_c = \frac{2}{R^2}\int_0^R h_c r dr \tag{4.10}$$

Where h_c represents time averaged and position specific convection coefficient, $h_c = q_c''/(T_s - T_{in})$. $\bar{h}_c$ (time and position averaged convection coefficient) was found to increase from 6.2 to 9.8 W m^{-2} K^{-1} with T_s increasing from 500 to 900 K. This change in $\bar{h}_c$ was deemed to be insufficiently large to justify an increase in the complexity of the convective loss model through introduction of a surface temperature dependent convection coefficient. Therefore, the convection coefficients computed at T_s = 700 K for the top sample surface and T_s = 600 K for the bottom sample surface were postulated to be representative of the corresponding surface temperature ranges.

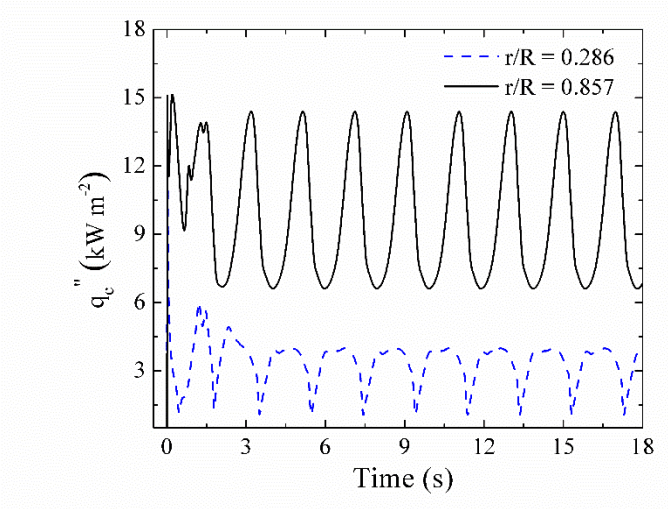

Figure 4.4 Convective loss heat fluxes computed for scenario #3 at r_z/R = 0.286 and r_z/R = 0.857

The time averaged top surface convection coefficients, h_c^{top}, computed for different scenarios are plotted with respect to the radial distance in Figure 4.5. Slope represents the ratio of maximum height versus radius of the sample surface. These scenarios also explore the impact of the shape of the sample on the convective loss from the top surface. The results indicate that the shape of the sample has a minor effect of the convection coefficient, while the impact of radial position is significant. This radial dependence is captured with Eq. (4.11):

$$h_c^{top} = e_1(r_z/R) + e_0 \tag{4.11}$$

Where e_1= 8.45 W m^{-2} K^{-1} and e_0= 2.97 W m^{-2} K^{-1}.

In addition to the sample geometries explored in these scenarios, the impact of a recessed top sample surface (3 mm below the edge of the sample holder) was also explored. It was determined that this geometry was well represented by the same parameters. The convection coefficient for the bottom surface was found to be weakly

dependent on radial distance and its surface area averaged value was determined to be 4 W m^{-2} K^{-1}.

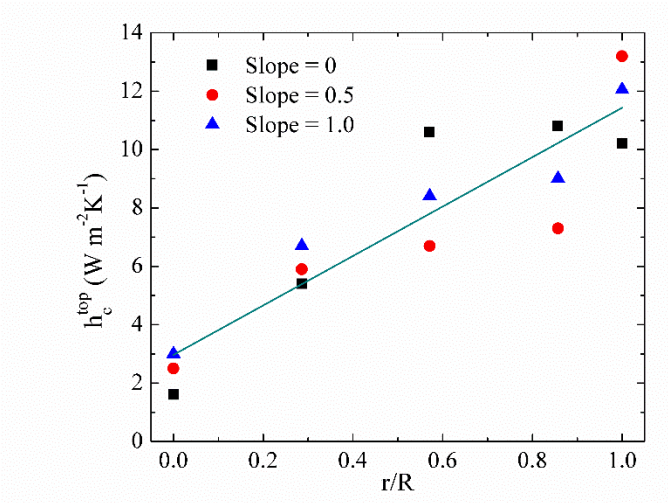

Figure 4.5 Time averaged convective heat transfer coefficients computed for Slope = 0, 0.5, 1.0. Slope represents the ratio of maximum height versus radius of the sample surface. The line is the fit of the data with Eq. (4.11).

An averaged value of h_c^{top} computed for the top surface was validated against an experiment where a copper plate, coated with a 0.95 emissivity paint and attached to Kaowool PM insulation board, was placed into the gasification chamber instead of a material sample and heated with the radiant heat flux set at 25 kW m^{-2}. The temperature of the plate was measured with embedded thermocouples and compared with results computed using h_c^{top} averaged over the top surface area of the plate with Eq. (4.11) in ThermaKin2Ds. The thermo-physical properties of copper and insulation can be found elsewhere [120,121]. As Figure 4.6 indicates, the modeled temperature is in excellent agreement with the results of the experimental measurement.

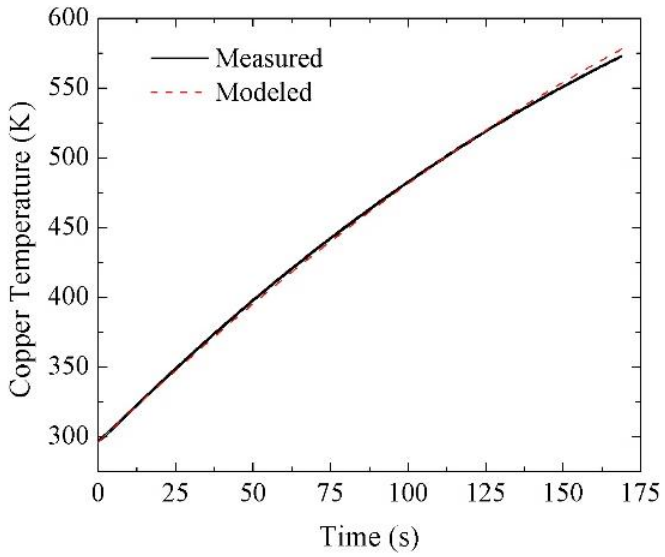

Figure 4.6 Comparison of experimental and modeled temperatures of the copper plate exposed to the incident radiant heat flux set at 25 kW m^{-2}.

4.3 Solution Methodology

To solve the mass and energy conservation equations, a material object is divided into finite volumes (or elements). For 2D axisymmetric objects, the elements were characterized by two sizes: x and z. These sizes represent discretization with respect to the corresponding axial and radial coordinates. Each element is also characterized by masses of components and temperature. Changes in these parameters with time are computed using a small time-step, t. For the x dimension, the time integration is based on the Crank-Nicolson scheme [122]. A detailed description of this integration procedure can be found in an earlier publication [36]. For the z dimension, a simple explicit integration is used. Previously performed simulations [118] indicate that the integration in the x dimension is stable at a wide range of selected values of x and t. The accuracy of the results gradually decreases with increasing value of either of these

parameters. Therefore, to ensure that a given simulation is converged, a sensitivity of the results to the values of the integration parameters should always be examined. x = 5×10^{-5} m and t = 0.01 s represent a good initial guess for a typical pyrolysis problem. The stability of the solution in the explicit integration dimension (z) is subject to a well-defined condition:

$$\frac{(\Delta z)^2}{\Delta t} > 2A \tag{4.12}$$

Where A represents either the gas transfer coefficient (λ) or thermal diffusivity ($\alpha = \frac{k}{\rho c}$), of the object, whichever is greater.

4.4 Verification of ThermaKin2Ds

To ensure that the 2D axisymmetric module was implemented correctly, its performance was compared to relevant analytical solutions. Four verification cases were examined, including heat conduction in the x and z directions as well as mass diffusion in both directions. The integration of chemical kinetics and solution of the radiation transport were verified previously within the framework of the original ThermaKin [36] and therefore did not require further verification in the 2D axisymmetric module.

4.4.1 Heat Conduction in the Axial Direction

A cylindrical object with temperature independent properties was employed to analyze the heat conduction in the axial direction. The cylinder had a height of L = 0.005 m and radius of W = 0.005 m. The initial temperature of the cylinder was at T_i = 300 K. The origin of the cylindrical coordinates was at the center of the bottom cylinder

surface. The top surface boundary (x = L) was set at a constant temperature, T_L = 1000 K, while the bottom and side boundaries were defined as adiabatic. The density, heat capacity, thermal conductivity, gas transfer coefficient, and emissivity of the cylinder were set at 1000 kg m^{-3}, 2000 J kg^{-1} K^{-1}, 0.2 W m^{-1} K^{-1}, 1×10^{-6} m^2 s^{-1}, and 0, respectively.

The governing equation for the 1D heat conduction in the axial direction is given by Eq. (4.13), obtained from Carslaw and Jaeger [123].

$$\frac{\partial^2 T}{\partial^2 x} = \frac{1}{\alpha}\frac{\partial T}{\partial t} \tag{4.13}$$

The analytical solution to this problem is given by Eqs. (4.14 – 4.16).

$$T(x,t) = T_L + \sum_{n=1}^{\infty} B_n \cos(\lambda_n x) \exp(-\lambda_n^2 \alpha t) \tag{4.14}$$

$$B_n = \frac{2}{L}\int_0^L (T_i - T_L)\cos(\lambda_n x)\, dx \tag{4.15}$$

$$\lambda_n = (n - \frac{1}{2})\frac{\pi}{L} \tag{4.16}$$

The infinite series was evaluated at n = 1000 to make sure that the resulting term was converged. In the ThermaKin2Ds simulation, the element sizes in x and z directions, and time step were set at 5 x 10^{-5} m and 5 x 10^{-3} m, and 0.01 s. The convergence of the numerical solution was verified by demonstrating that the results were not sensitive to a factor of four change in the integration parameters. Figure 4.7(a) portrays the comparison between the numerical results from ThermaKin2Ds (open symbols) and the analytical solution (red solid line) for several different times. The two solutions are in a perfect agreement with each other.

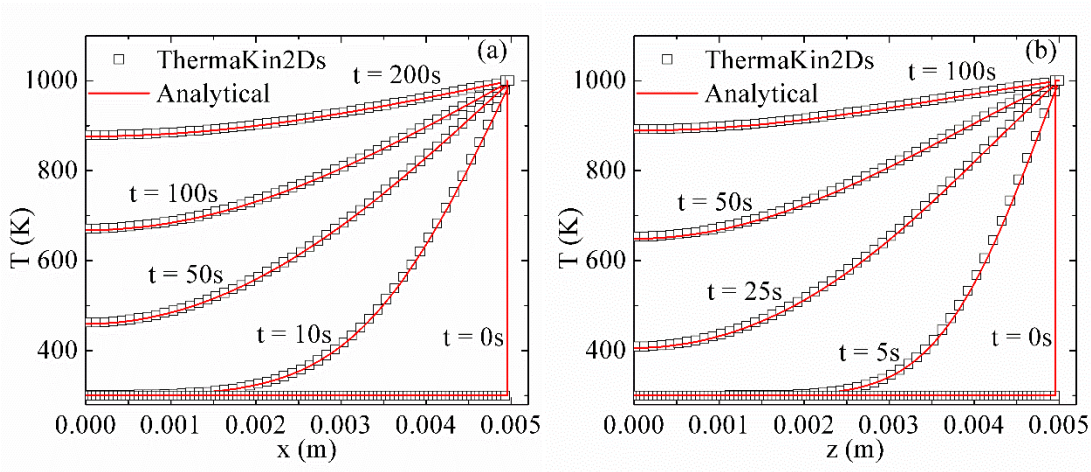

Figure 4.7 A comparison of the temperature profiles of transient heat conduction in the (a) axial and (b) radial directions between the ThermaKin2Ds simulation and corresponding analytical solutions [123].

4.4.2 Heat Transfer in the Radial Direction

The same cylindrical object with the same constant material properties was employed to examine the transient heat conduction in the radial direction. The initial temperature of the cylinder was prescribed as T_i = 300 K. The temperature at z = W (in the radial direction) was set to a constant value, T_W = 1000 K. The top and bottom surface boundaries were defined as adiabatic. The analytical solution for the 1D transient heat conduction in the radial direction is given as Eq. (4.17) [123].

$$\frac{1}{z}\frac{\partial}{\partial z}\left(z\frac{\partial T}{\partial z}\right) = \frac{1}{\alpha}\frac{\partial T}{\partial t} \tag{4.17}$$

The analytical solution to this problem is given by Eq. (4.18)

$$T(z,t) = T_W + \frac{2(T_i - T_W)}{W}\sum_{n=1}^{\infty}\left(\frac{J_0(\lambda_n z)}{\lambda_n J_1(\lambda_n W)}\exp(-\alpha\lambda_n^2 t)\right) \tag{4.18}$$

Where J_0 and J_1 represent Bessel functions, and the eigenvalues are the roots of $J_0(\lambda_n W) = 0$. The infinite series was evaluated at n = 308 to make sure that the resulting

term was converged. In the ThermaKin2Ds simulation, the element sizes in axial and radial directions, and time step were set at 5 x 10^{-3} m and 5 x 10^{-5} m, and 0.01 s. A comparison of this solution with the ThermaKin2Ds simulation is shown in Figure 4.7(b). The two results are in good agreement, which indicated that the heat transport in the radial direction was solved correctly in the 2D axisymmetric module.

4.4.3 Mass Transfer in the Axial Direction

The transient mass diffusion in the axial direction was examined using the same cylindrical object (same dimensions and same physical properties) as that defined in Section 4.4.1. The initial gas concentration (C) inside the cylinder was set as C_i =0 kg m^{-3}. No mass transport was allowed through the side or bottom surface boundaries (x = 0). The gas concentration at the top surface boundary (x = L) was set to be a constant value of C_L = 250 kg m^{-3}. The temperature of the cylinder and environment was set at a constant value of 300 K.

According to Crank [124], the analytical solution for the 1D mass diffusion in the axial direction is given by Eq. (4.19):

$$\frac{\partial^2 C}{\partial^2 x} = \frac{1}{\lambda}\frac{\partial C}{\partial t} \tag{4.19}$$

λ is the gas transport coefficient. The analytical solution to this problem is given by Eqs. (4.20 - 4.22).

$$C(x,t) = C_L + \sum_{n=1}^{\infty} B_n \cos(\lambda_n x)\exp(-\lambda_n^2 \lambda t) \tag{4.20}$$

$$B_n = \frac{2}{L}\int_0^L (C_i - C_L)\cos(\lambda_n x)\,dz \tag{4.21}$$

$$\lambda_n = (n - \frac{1}{2})\frac{\pi}{L} \tag{4.22}$$

The infinite series was evaluated at n = 1000 to make sure that the resulting term

was converged. In the ThermaKin2Ds simulation, the element sizes in x and z directions, and time step were set at 5 x 10^{-6} m and 5 x 10^{-3} m (a single element in the radial direction), and 0.001 s. The convergence of the numerical solution was verified by demonstrating that the results were not sensitive to a factor of four change in the integration parameters. Figure 4.8(a) portrays the comparison of the gas concentration profiles in the axial direction obtained from the analytical solution and simulation. The results are in perfect agreement with each other.

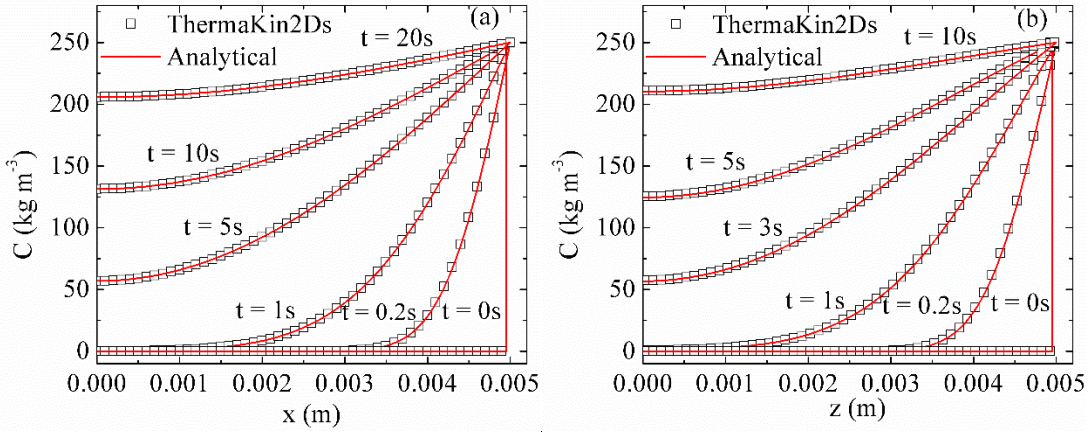

Figure 4.8 A comparison of the concentration profiles arising as a result of transient mass diffusion in the (a) axial and (b) radial directions between the ThermaKin2Ds and corresponding analytical solutions [124].

4.4.4 Mass Transfer in the Radial Direction

The mass transfer in the radial direction was verified use the same cylindrical object with the same physical properties. The initial gas concentration condition was prescribed as $C_i = 0$ kg m^{-3}. The gas concentration at z = W (in the radial direction) was set as $C_W = 250$ kg m^{-3}. No mass transport was allowed at the top and bottom surface boundaries. The temperature of the cylinder and environment was set at a constant

value of 300 K. The governing equation for the mass transfer in the radial direction is given by Eq. (4.23), obtained from Crank [124].

$$\frac{1}{z}\frac{\partial}{\partial z}\left(z\frac{\partial C}{\partial z}\right) = \frac{1}{\lambda}\frac{\partial C}{\partial t} \tag{4.23}$$

The analytical solution to this problem was given by Eq. (4.24).

$$C(z,t) = C_W + \frac{2(C_i - C_W)}{W}\sum_{n=1}^{\infty}\left(\frac{J_0(\lambda_n z)}{\lambda_n J_1(\lambda_n W)}\exp(-\lambda\lambda_n^2 t)\right) \tag{4.24}$$

J_0 and J_1 represent Bessel functions, and the eigenvalues are the roots of $J_0(\lambda_n W) = 0$. The infinite series was evaluated at n = 308 to make sure that the resulting term was converged. In the ThermaKin2Ds simulation, the element sizes in axial and radial directions, and time step were set at 5 x 10^{-3} m (a single element in axial direction) and 5 x 10^{-5} m, and 0.001 s. Figure 4.8(b) portrays the comparison between the numerical results from ThermaKin2Ds (open symbols) and the analytical solution (red solid line) for several different times. The excellent agreement between the two solutions provides a verification that the numerical model is correct.

4.5 Modeling Setup

4.5.1 Modeling Milligram-scale Experiments

In the modeling of the milligram-scale experiments, all samples were treated as thermally thin and simulated using a single spatial element. The gas transfer coefficient was set at $2 \times 10^{-5}\ m^2 s^{-1}$ for all gaseous decomposition products to enable an unimpeded gas flow through the condensed-phase. The mass flow boundary for the top sample surface was defined to provide no resistance to the outflow of the gaseous pyrolyzate. No mass flow was allowed through the back surface boundary. The element

temperature was forced to follow the mean experimental temperature profile by defining a sufficiently high convection coefficient (1×10^5 W m^{-2} K^{-1}) at the element boundary. To account for the thermal inertia preventing the STA and MCC from reaching the nominal heating rate instantaneously [82,125], the actual experimental temperature profile was approximated by expressing the heating rate as an exponentially-decaying sinusoidal function, described in Eq. (4.25).

$$\frac{dT}{dt}(t) = u_1\left(1 - (\exp(-u_2\, t))(\cos(u_2\, t) + u_4 \sin(u_3\, t))\right) \quad (4.25)$$

This function was added to the modeling formulation to define the temperature of the simulated sample as a function of time. The parameters of this function were determined to reproduce heating rate profiles observed in the STA and MCC experiments. For each set of materials (PA66-based and PBT-based blends), the heating rate profile was re-fitted (polymer matrix was used to represent each set of blends). An example of the comparison of the fitted and experimental heating rate profiles for PA66/GF/RP blends of STA tests at 10 K min^{-1} is shown in Figure 4.9. The values of the resulting parameters are provided in Table 4.2. The heating rate functions were also parametrized for the STA tests at 5 K min^{-1} and 20 K min^{-1} and MCC tests at 10 K min^{-1}. The corresponding values of the parameters in Eq. (4.25) are also reported in Table 4.2.

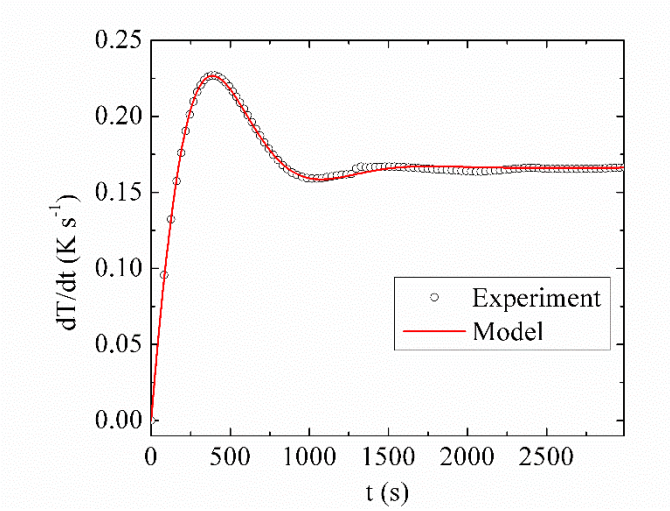

Figure 4.9 Instantaneous heating rate as a function of time for PA66/GF/RP blends of STA tests at 10 K min^{-1}

Table 4.2 The values of parameters in Eq. (4.25) determined for STA and MCC tests. (MCC tests were marked with asterisk).

	Heating Rate K min^{-1}	u_1 K s^{-1}	u_2 s^{-1}	u_3 s^{-1}	u_4
PA66/GF/RP	5	0.0835	0.0033	0.0049	-0.9278
	10	0.166	0.0030	0.0046	-0.9922
	20	0.333	0.0024	0.0054	-0.6971
	10 *	0.167	0.0034	0.0046	-0.2403
PBT/GF/DEPAL/MPP	5	0.0835	0.0033	0.0049	-0.9278
	10	0.1662	0.0030	0.0046	-1.094
	20	0.333	0.0024	0.0054	-0.6971
	10 *	0.167	0.0034	0.0046	-0.2403

* Represent the MCC tests

4.5.2 Modeling Bench-scale Experiments

In this work, a 1D assumption was made when simulating the bench-scale gasification experiments due to the approximately flat sample surface and small changes in sample thickness. Therefore, all calculations were conducted using x = 1 ×

10^{-5} m and z = 3.5×10^{-2} m (a single element in the radial direction) spatial discretization and 0.01 s time step. Every integration parameter was varied by a factor of two, while keeping the others fixed, and the simulation results were compared to ensure that all numerical solutions were fully converged. The gas transfer coefficient was set at $2 \times 10^{-5}\ m^2 s^{-1}$ for all gaseous decomposition products to enable an unimpeded gas flow through the condensed-phase. The gaseous products were assumed not to contribute to the volume of the sample. The mass flow boundary for the top sample surface was defined to provide no resistance to the outflow of the gaseous pyrolyzate. No mass flow was allowed through the back surface boundary, which simulated the presence of the copper foil underneath the sample [117]. The sample thickness evolution was modeled by prescribing the densities of condensed-phase decomposition products to capture the overall change in sample volume as done previously [82].

As discussed in Section 3.2.2, the instantaneous gas temperatures (T^e) were quantified and used in the calculations of convective heat flux at top sample surface. The gas temperature evolution was expressed through Eq. (4.26). It is important to note that a constant top background temperature ($T_{top,e}$) of 290 K, which corresponds to the temperature of the heat flux gauge, was used as a baseline for the temperature fitting. The associated fitting parameters of Eq. (4.26) were determined for each applied incident heat flux, as shown in Table 4.3.

$$T^e = T_1^e \exp(T_2^e t) + T_3^e \exp(T_4^e t) + 290 \quad (4.26)$$

The background temperature at the bottom surface was assumed to be the same as measured inner chamber wall temperature which showed an initial rise (from 300

K) until about 800 s and then stayed constant. The initial temperature rise was approximately fitted using a linear function. The transition point/temperature ($T_{bottom,e}$) at 800 s for each heat flux is determined and reported in Table 4.3.

Table 4.3 The values of the fitting parameters for the gas temperature and the background temperature at the top and bottom surface.

Nominal heat flux [kW m^{-2}]	T_1^e [K]	T_2^e [s^{-1}]	T_3^e [K]	T_4^e [s^{-1}]	$T_{top,e}$ [K]	$T_{bottom,e}$ [K]
30	48.1	3.11×10^{-8}	-26.6	-1.28×10^{-2}	290	316
40	66.5	9.80×10^{-6}	-35.0	-1.29×10^{-2}	290	322
45	73.8	2.11×10^{-6}	-42.5	-1.06×10^{-2}	290	325
60	90.5	1.19×10^{-5}	-54.7	-8.98×10^{-3}	290	334

Chapter 5. Characterization of PA66/GF/RP Blends

5.1 Milligram-scale Results and Analysis

5.1.1 Overall Approach to Reaction Model Development for PA66/GF/RP Blends

The generalized reaction model for the PA66/GF/RP system was developed through a quantitative analysis of the thermal degradation behavior of PA66/GF25, PA66/GF25-RP1.5, and PA66/GF25-RP6.0 blends. This development process consisted of four steps. First, a PA66 decomposition model was derived from the TGA and DSC data obtained for the PA66/GF25 blend. The GF component was assumed to be chemically inert.

In the second step, an attempt was made to simulate the TGA and DSC data obtained for the PA66/GF25-RP1.5 blend using a combination of the PA66 decomposition model and a reaction representing sublimation of RP, the kinetics of which was initially estimated using literature data. Significant differences between this simulation and experimental data were identified. These differences were interpreted as evidence of a chemical interaction between PA66 and RP. The parameters of reactions representing this interaction were determined thorough a fitting of the TGA and DSC data obtained for PA66/GF25-RP1.5 and PA66/GF25-RP6.0 blends.

In the third step, the reaction model including this interaction was employed to simulate MCC experimental data for PA66/GF25, PA66/GF25-RP1.5, and PA66/GF25-RP6.0 blends. Heats of combustion (h_{com}) of all gaseous reaction products

were derived from these simulations. In the final step, the validity of the developed reaction model was verified by demonstrating that this model successfully predicts TGA data for a series of blends with a wide range of RP content. It was also shown that the reaction model captures the kinetics of decomposition of these materials at lower and higher heating rates than those utilized in the parameterization process.

5.1.2 Inverse Modeling of TGA and DSC Data of PA66/GF/GF Blends

The mean experimental results of the TGA and DSC tests of PA66/GF25 blend are shown as open symbols in Figure 5.1. Figure 5.1(a) displays the dependence of the sample mass, m, and MLR normalized by the initial mass, m_0, on temperature, T. Figure 5.1(b) contains initial-sample-mass-normalized heat flow and integral heat flow dependences on temperature. All error bars were calculated as two standard deviations of the mean. The experimental MLR profile contains a single peak at 700 K corresponding to the decomposition process. This decomposition produced 27 wt.% condensed-phase residue, which included 25 wt.% of GF. The normalized heat flow curve contains two distinct maxima. The first (535 K) maximum represents the melting process; the second (700 K) maximum represents thermal decomposition.

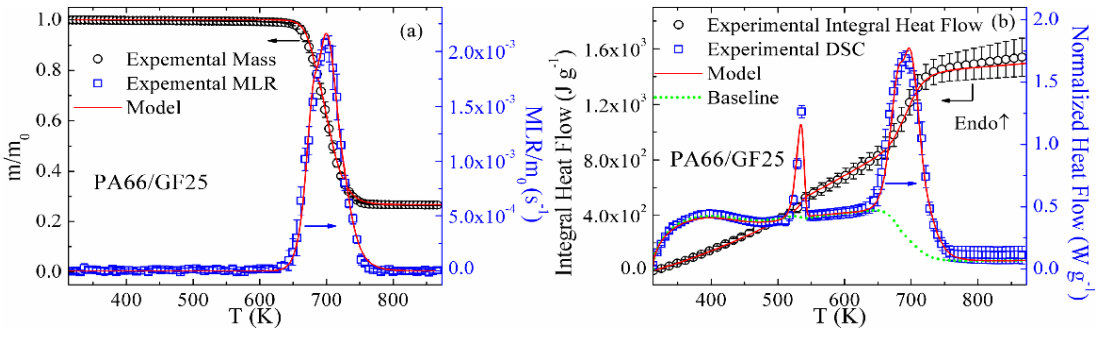

Figure 5.1 Experimental and simulated (a) TGA and (b) DSC data obtained for PA66/GF25 at 10 K min^{-1}

During the inverse modeling process, several criteria were defined to help bring the agreement between modeled and experimental curves within the experimental uncertainties. The kinetic parameters were adjusted until the experimental and modeled final mass residues, and positions and magnitudes of MLR maxima were within 3%, 5 K and 8%, respectively. The thermodynamic parameters were adjusted until the predicted magnitudes of heat flow maxima were within 10%, temperatures of the maxima were within 5 K, and final integral heat flow was within 5% of the average experimental results.

A reaction scheme consisting of four consecutive steps, Reactions (1-4), given in Table 5.1 was found to be required to capture the experimental TGA and DSC data of PA66/GF25 with the accuracy defined by the aforementioned criteria. Reaction (1) was used to represent the melting process. Reactions (2-4) were required to accurately capture the shape and magnitude of both the MLR and heat flow peaks corresponding to the decomposition. The component names used in this reaction scheme are self-explanatory. The key reaction parameters, including the pre-exponential factor, A, and activation energy, E, are provided in Table 5.2. The reaction parameters were derived through a manually iterative process that is discussed in detail in earlier publications [12,82] and Appendix II.

The heat capacity of GF was obtained from the literature [126]. The heat capacities of PA66 and PA66_Melt components were determined through the fitting of the corresponding regions of the experimental PA66/GF25 DSC data. The heat capacity

of the component representing the final residue, PA66_Res3, could not be resolved due to an extremely small yield (2 wt.%). Therefore its heat capacity was assumed to be equal to the average heat capacity of chars, 1700 J $kg^{-1}K^{-1}$ [46], produced by several common polymers. The heat capacities of the intermediate condensed-phase products, PA66_Res1 and PA66_Res2, were assumed to be equal to the average heat capacity of the PA66_Melt and PA66_Res3. The heat capacity values of all condensed phase components are listed in Table 5.3. The heats of reactions, h, were fitted into the corresponding regions of the DSC curve after all heat capacities were determined; the values of h are listed together with the kinetic parameters in Table 5.2. Additional details of the thermodynamic parameter determination process are provided in earlier publications [12,82,110,125] and Appendix II.

Table 5.1 Reaction model for all tested materials.

#	Reaction
1	PA66→PA66_Melt
2	PA66_Melt→0.83 PA66_Res1+0.17 PA66_Gas1
3	PA66_Res1→0.4 PA66_Res2+0.6 PA66_Gas2
4	PA66_Res2+PA66_Res2→0.14 PA66_Res3+1.86 PA66_Gas3
5	RP→RP_Gas
6	PA66_Melt+0.03 RP→1.03 PA66_RP
7	PA66_RP→0.04 PA66_RP_Res1+0.96 PA66_RP_Gas1
8	PA66_RP+0.02 RP→0.49 PA66_RP_Res2+0.53 PA66_RP_Gas2
9	PA66_RP_Res2→0.21 PA66_RP_Res3+0.79 PA66_RP_Gas3

Table 5.2 Kinetic and thermodynamic parameters of reactions of the thermal decomposition of PA66/GF/RP system (the positive heat values correspond to endothermic processes).

#	A (s^{-1} or $m^3\ kg^{-1}\ s^{-1}$)	E ($J\ mol^{-1}$)	h ($J\ kg^{-1}$)
1	2.0×10^{40}	4.28×10^5	9.1×10^4
2	1.5×10^{30}	4.13×10^5	1.3×10^5
3	1.1×10^{19}	2.80×10^5	4.4×10^5
4	9.7×10^{14}	2.75×10^5	8.4×10^5
5	1.5×10^{18}	2.74×10^5	5.5×10^5
6	1.0×10^{19}	2.49×10^5	0
7	1.5×10^{20}	3.02×10^5	6.5×10^5
8	1.1×10^{17}	2.69×10^5	3.1×10^5
9	1.5×10^{17}	2.69×10^5	2.9×10^5

Table 5.3 Heat capacities of condensed-phase components.

Component	c ($J\ kg^{-1}\ K^{-1}$)	Component	c ($J\ kg^{-1}\ K^{-1}$)
PA66	$-640 + 7.32T$	PA66_Res3	1700
GF	$442 + 1.24T$	PA66_RP	$606 + 4.10T$
RP	$510 + 0.50T$	PA66_RP_Res1	1700
PA66_Melt	$610 + 4.30T$	PA66_RP_Res2	$1153 + 2.05T$
PA66_Res1	$1155 + 2.15T$	PA66_RP_Res3	1700
PA66_Res2	$1155 + 2.15T$		

The RP is known to sublime at 671 K [127]. Therefore, Reaction (5) was added to the reaction scheme (see Table 5.1) to represent this transition. Subsequently, an attempt was made to fit the PA66/GF25-RP1.5 TGA and DSC experimental data shown in Figure 5.2 by adjusting the parameters of this reaction. This fitting attempt was unsuccessful because the magnitude of the MLR maximum increased significantly (with respected to that produced by PA66/GF25 blend and shown in Figure 5.1(a)), while the amount of added RP (1.5 wt.%) was close to negligible. The position of the maximum also shifted to a higher temperature (710 K), which was impossible to

explain by the sublimation reaction. Therefore, a reaction between PA66_Melt and RP, Reaction (6), was added to the reaction scheme (see Table 5.1).

This Reaction (6) in Table 5.1 was assumed to occur at a temperature below the onset of the thermal decomposition of PA66 (630 K) and to consume a majority of the PA66_Melt component in the PA66/GF25-RP1.5 blend. These assumptions were supported by the fact that neither the onset nor peak MLR associated with the decomposition of PA66_Melt were evident in the PA66/GF25-RP1.5 experimental data. Aside from converting PA66_Melt to a new condensed-phase component, this reaction produced no heat or mass loss, as indicated by the experimental data shown in Figure 5.2. It is possible that the reason why this reaction did not manifest itself directly in the experimental data is because it took place during the material manufacturing process as RP is known to be highly reactive even at relatively low temperatures [127].

Subsequently, a reaction of decomposition of the product of the PA66_Melt and RP interaction, Reaction (7) in Table 5.1, was added and its kinetic parameters were determined through fitting of the main MLR peak observed for the PA66/GF25-RP1.5 blend. This new reaction mechanism (Reactions (1-7) in Table 5.1) was utilized to predict the experimental data obtained for the PA66/GF25-RP6.0 blend and shown in Figure 5.3. The two MLR maxima (at 678 and 730 K) observed for this material were not successfully predicted by this reaction scheme even after the parameters of Reaction (5) were varied in an attempt to fit the experimental data.

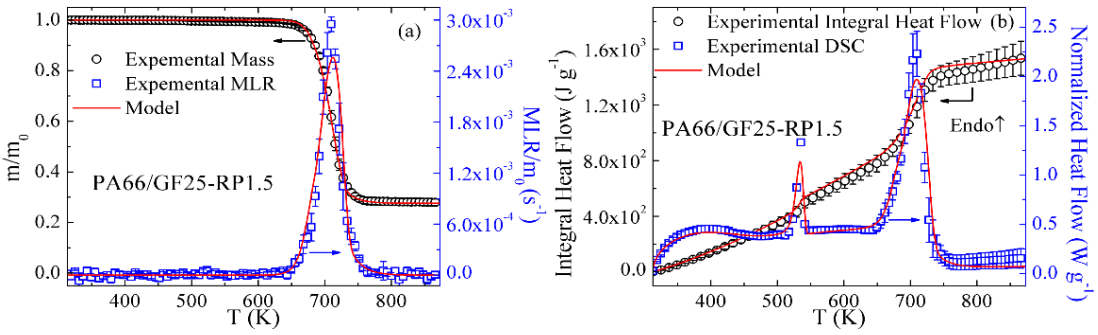

Figure 5.2 Experimental and simulated (a) TGA and (b) DSC data obtained for PA66/GF25-RP1.5 at 10 K min^{-1}

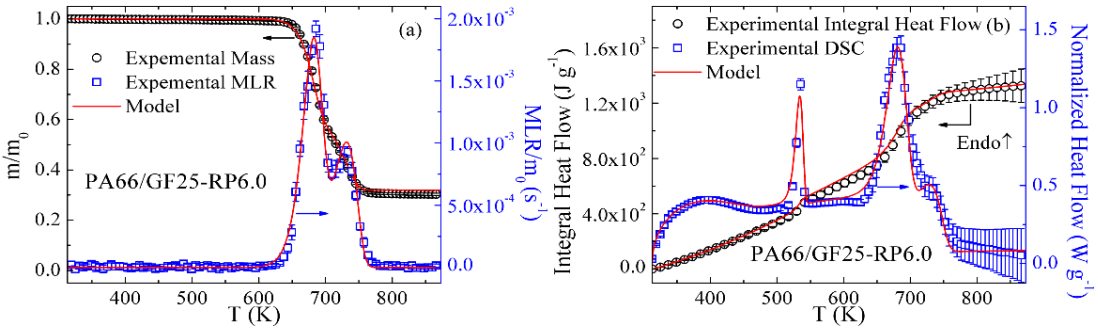

Figure 5.3 Experimental and simulated (a) TGA and (b) DSC data obtained for PA66/GF25-RP6.0 at 10 K min^{-1}

The simplest explanation of this result is that, in the PA66/GF25-RP6.0 blend, the remaining RP, which is not consumed in the reaction with PA66_Melt, reacts with the PA66_Melt and RP interaction product, PA66_RP, to produce a gaseous component and condensed-phase residue. This additional reaction, Reaction (8) in Table 5.1, competes with Reaction (7) and, together with further decomposition reaction, Reaction (9), create a dual peak MLR structure consistent the experimental data shown in Figure 5.3(a).

The kinetic parameters of Reactions (8), (9) and (5) in Table 5.1 were adjusted to fit the experimental MLR observed for the PA66/GF25-RP6.0. The variation in the

parameters of the reaction representing sublimation of RP (Reaction (5)) was constrained to keep this reaction's onset temperature equal to the reported sublimation point (671 K [127]). The heat capacity of RP was obtained from the literature [127]. The heat capacity of PA66_RP was calculated as the average of heat capacities of PA66_Melt and RP weighted by the stoichiometric coefficients of Reaction (6) in Table 5.1. The heat capacity of PA66_RP_Res1 and PA66_RP_Res3 was assumed as the average heat capacity of chars, 1700 $\mathrm{J\,kg^{-1}K^{-1}}$ [46]. The heat capacity of the intermediate condensed-phase product PA66_RP_Res2 was determined as the average of heat capacities of PA66_RP and PA66_RP_Res3. The heats of Reactions (5-9) in Table 5.1 were determined through fitting of the DSC data obtained for PA66/GF25-RP1.5 and PA66/GF25-RP6.0 blends. The kinetic and thermodynamic parameters of these reactions can be found Table 5.2 and 5.3.

As indicated by the red solid lines in Figure 5.2 and 5.3, the developed reaction model successfully predicts the TGA and DSC data for PA66/GF25-RP1.5 and PA66/GF25-RP6.0 blends. This model (Reactions (1-9) in Table 5.1) also successfully predicts the thermal of decomposition of PA66/GF25. For consistency, all model predictions shown in Figures 5.1-5.3 were generated using the same (complete) reaction mechanism.

5.1.3 Inverse Modeling of MCC Data of PA66/GF/RP Blends

The heat of combustion of RP_Gas was computed using the oxygen consumption method [128]. The heats of combustion of other volatiles were first estimated by dividing the MCC experimental HRR data by the MLR computed in ThermaKin2Ds

using the heating rate history specific to the MCC [12]. Comparisons between the experimental HRR and modeled MLR profiles revealed some discrepancies. The experimental HRR curves had a tendency to be shifted to a lower temperature by 0-5K, which was apparent because some portions of the curves indicated heat release in the absence of concurrent mass loss. The experimental HRR data were shifted to a higher temperature to correct these discrepancies. The magnitude of the shift was determined using the principle that any significant heat release required a concurrent mass loss.

A predicted HRR curve was subsequently generated by multiplying the rates of production of each gaseous component, computed using ThermaKin2Ds, by the corresponding estimated value of h_{com} and adding these contributions. The values of h_{com} were further refined until the predicted and experimental MCC data agreed within the established criteria. The criteria were defined as differences of less than 5% between the height of the experimental and modeled HRR maxima, less than 8K between the positions of the HRR maxima and less than 8% between the final integral HRR values. The results of h_{com} are reported in Table 5.4. All h_{com} values are within the range, $1.69 - 3.8 \times 10^7$ J kg^{-1}, consistent with the hydrocarbon nature of these gases [129]. Figure 5.6 shows the comparisons of the experimental and simulated MCC data obtained for all the tested systems. The non-modified and shifted experimental data are less than 5K apart and therefore only the shifted experimental data are shown to avoid congestion. The model captures the experimental HRR and integral HRR of the three materials very well.

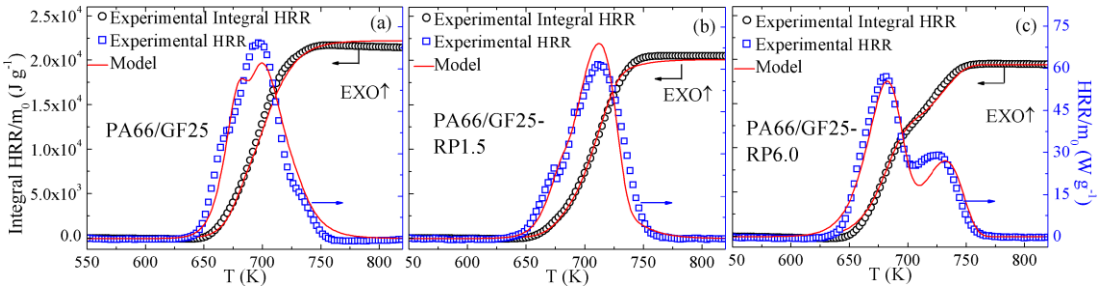

Figure 5.4 Experimental and simulated MCC data for (a) PA66/GF25, (b) PA66/GF25-RP1.5, and (c) PA66/GF25-RP6.0 at 10 K min^{-1}

Table 5.4 Heats of combustion of gaseous decomposition products (here, the positive heat values correspond to exothermic processes)

Component	h_{com} (J kg^{-1})	Component	h_{com} (J kg^{-1})
PA66_Gas1	3.80×10^7	PA66_RP_Gas1	2.65×10^7
PA66_Gas2	2.85×10^7	PA66_RP_Gas2	3.10×10^7
PA66_Gas3	2.90×10^7	PA66_RP_Gas3	2.68×10^7
RP_Gas	1.69×10^7		

5.1.4 Milligram-scale Model Validation for PA66/GF/RP Blends

The final reaction model (summarized in Table 5.1) has been formulated to accurately reproduce TGA, DSC, and MCC data of PA66/GF25, PA66/GF25-RP1.5, and PA66/GF25-RP6.0 blends. To validate the model, first, its ability to predict thermal decomposition dynamics of the same blends at lower (5 K min^{-1}) and higher (20 K min^{-1}) heating rates than those used in the model parameterization process was examined. A comparison of the experimental TGA data obtained at these heating rates (open symbols) with model predictions (red solid lines) is shown in Figure 5.5. This comparison indicates that this model successfully captures the impact of heating rate on the rate of production gaseous species.

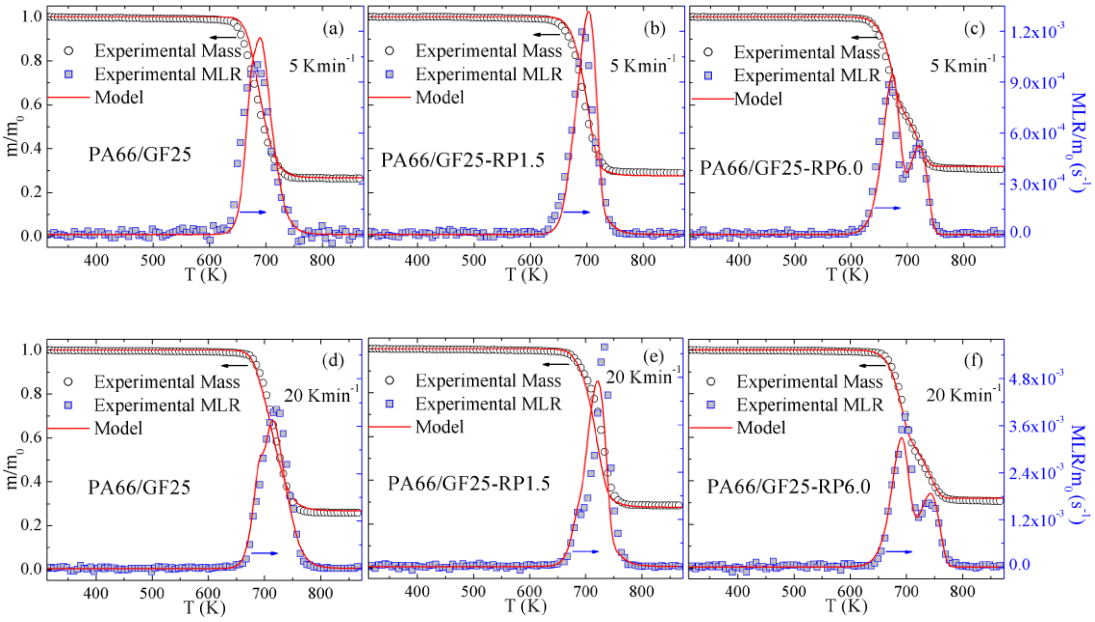

Figure 5.5 Experimental and simulated TGA data obtained for PA66/GF25, PA66/GF25-RP1.5, PA66/GF25-RP6.0 at (a) (b) (c) 5 K min^{-1} and (d) (e) (f) 20 K min^{-1}

Subsequently, an ability of the model to predict outcomes of TGA experiments conducted on material compositions that differ from those used in the parameterization process was tested. A comparison of the modeling predictions with experimental results obtained for pure PA66, PA66/GF25-RP3.0, PA66/GF25-RP4.5, and PA66/GF25-RP9.0 materials is shown in Figure 5.6. The model predicts all experimental data well, with a possible exception of pure PA66. The model underpredicts the temperature of the PA66 MLR peak by 18 K. This discrepancy is likely a consequence of unique behavior of this material in the TGA tests. In these tests, the material had a tendency to partially re-condense on the top lid of the crucible thus creating a physical separation and associated temperature lag between the sample and the sensor (located below the bottom of the crucible). The rest of material

compositions studied in this work (including PA66/GF25 blend) did not exhibit re-condensation. The peak experimental MLR for the PA66/GF25-RP3.0 blend was also somewhat underpredicted. However, the overall agreement was deemed acceptable because the mass evolution trend, including the onset of mass loss and final residue yield, was captured well.

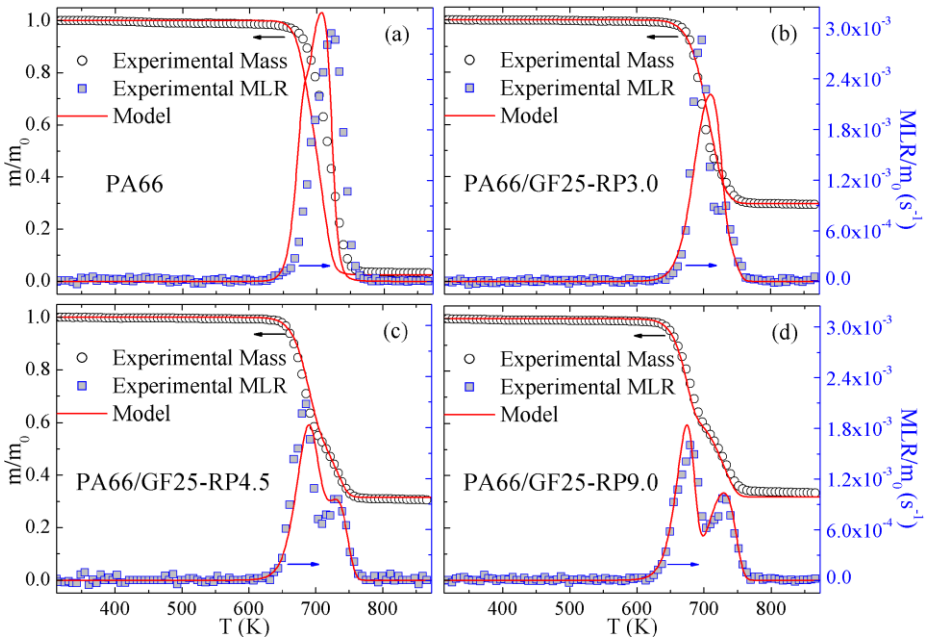

Figure 5.6 Experimental and simulated TGA data obtained for (a) PA66, (b) PA66/GF25-RP3.0, (c) PA66/GF25-RP4.5, and (d) PA66/GF25-RP9.0 at 10 K min^{-1}

5.2 Bench-scale Results and Analysis

5.2.1 Overall Approach to Pyrolysis Model Development for PA66/GF/RP Blends

The pyrolysis model development of PA66/GF/RP blends requires the measurement of the kinetics and thermodynamics of thermal decomposition, heats of combustion of gaseous products, and thermal transport properties. The kinetics and

thermodynamics of thermal decomposition and heats of combustion of gaseous products have been parameterized through a manually iterative inverse analysis of milligram-scale experimental data in Section 5.1. The resulting reaction model along with the determined parameters summarized in Tables 5.1-5.4, are capable of predicting TGA, DSC, and MCC data as a function of material compositions and heating conditions. The thermal transport properties were determined through an inverse analysis of the bench-scale gasification experimental measurements. This inverse analysis of bench-scale results for the multi-component blends consisted of four steps.

In the first step, the sample thickness and T_{back} data of pure PA66 at 60 kW m^{-2} were inversely analyzed to determine the thermal transport properties of PA66-based condensed-phase components participating in Reactions (1-4) in Table 5.1. The resulting thermal transport properties were validated against the corresponding MLR data at 60 kW m^{-2}, which were not used in the parameterization process. It is important to note that the temperature data at the lower heat flux, 30 kW m^{-2}, were not employed in the parameterization process because the results were found to be poorly reproducible.

In the second step, the thermal transport properties of GF were determined using the sample thickness and T_{back} data of PA66/GF25 at 30 kW m^{-2} and 60 kW m^{-2}. The parameterization process relied on the thermal transport properties of PA66 determined in the first step. Initially, GF was modeled as a single component throughout the test. However, it was determined that it was impossible to capture the temperature profiles at both heat fluxes by treating GF in such simple manner.

Therefore, GF was assumed to evolve identically to PA66 decomposition shown as Reaction (1-4) in Table 5.1 (GF → GF_Melt, GF_Melt → GF_Res1, GF_Res1 →GF_Res2, GF_Res2→GF_Res3). These reactions were assigned the same Arrhenius parameters as Reactions (1-4). They were also specified not to contribute to mass loss or heat production/consumption. Their purpose was to account for evolution of the interface between GF and decomposing PA66; this interface was speculated to have a significant impact on the heat transport process. The thermal transport properties of GF-based components were subsequently obtained.

In the third step, the thermal transport parameters of RP-based components participating in Reactions (5-7) in Table 5.1 were determined through the inverse analysis of sample thickness and T_{back} data of PA66/GF25-RP1.5 at 40 kW m^{-2} and 60 kW m^{-2}. The thermal transport parameters of RP-based components participating in Reactions (8-9) in Table 5.1 were determined and validated through the inverse analysis of experimental measurements of PA66/GF25-RP6.0 at 40 kW m^{-2} and 60 kW m^{-2}. The lower RP concentration blend, PA66/GF25-RP1.5, was not selected in parameterizing the properties of components participating in Reactions (8-9) in Table 5.1 because these two reactions were inactive when the RP concentration is low. The parameterization was further validated against the MLR data obtained for both RP-containing blends. A single pyrolysis model was developed based on the resulting material properties in these three steps and previously determined reaction parameters [110]. This pyrolysis model was capable of capturing the pyrolysis behavior of PA66, PA66/GF25, PA66/GF25-RP1.5, and PA66/GF25-RP6.0.

In the final step, the extrapolating capability of the resulting model was further examined through predicting experimental measurements obtained for two additional blends with new compositions, PA66/GF25-RP4.5 and PA66/GF-RP9.0. The RP concentration of PA66/GF25-RP4.5 was in between the blends employed for the model development and PA66/GF-RP9.0 had a higher RP concentration than the calibration blends. Additional simulations of an idealized cone calorimeter experiment were conducted to understand the impact of red phosphorus on HRR data of a burning sample and thus evaluate its role in the fire performance of PA66/GF/RP blends.

5.2.2 Pyrolysis Model Development for Pure PA66

Inverse analysis of the gasification experimental results of PA66 requires knowledge of the optical properties (emissivity and absorption coefficient) of all the condensed-phase components participating in Reactions (1-4) in Table 5.1. The emissivity of PA66 was obtained from the study by Linteris et al. [62]. The same emissivity as PA66 was assigned to PA66_Melt assuming the melting process did not affect the sample emissivity. The emissivity of residual component, PA66_Res3, was defined as 0.94. This value was determined experimentally by comparing the measured back surface temperatures of various residue samples with one-half of the residue surface coated with high emissivity paint (0.94) and the other uncoated residue. No difference in the sample back surface temperature was identified between the painted and unpainted halves. Therefore, the emissivity of the residual component was defined to be the same as the paint emissivity, 0.94. PA66_Res2 and PA66_Res3 were produced within a similar temperature range and thus PA66_Res2 was assumed to have the same emissivity as PA66_Res3. The emissivity of intermediate product

(PA66_Res1) that represented the gradual transformation from PA66_Melt to PA66_Res2, was assumed to be equal to the averaged value of PA66_Melt and PA66_Res2.

The absorption coefficient of PA66 was measured through the broadband radiation absorption experiment described in Section 3.2.1. The final residue was observed to appear very optically dark and graphitic in nature. Therefore, the absorption coefficient of the final residue, PA66_Res3, was defined sufficiently high (100 $m^2 kg^{-1}$) to ensure that no significant radiation was allowed to transmit through the residue. The intermediate components, PA66_Melt, PA66_Res1, and PA66_Res2, were the products of the consecutive reactions, describing the gradual physical and chemical transformation from the original component to the final decomposition product. Therefore, the absorption coefficients of these intermediate components were defined to be equally spanned between the values of initial component (PA66) and final residue (PA66_Res3). It should be noted that the absorption coefficients reported in the current study were normalized by the corresponding densities. The resulting emissivity and absorption coefficients are provided in Table 5.5.

Subsequently, the densities of five condensed-phase components, PA66, PA66_Melt, PA66_Res1, PA66_Res2, and PA66_Res3, were defined to capture the observed experimental sample thickness evolution. The density of PA66 was measured at room temperature. At 60 kW m^{-2}, 1 wt. % of residue remained at the end of the test. The densities of all the components were initially defined to be equal to PA66. Subsequently, the densities of PA66_Res1 and PA66_Res2 were refined based on the experimental observations (no reduction in the sample thickness during the early stage

of pyrolysis test). The density of PA66_Res3 was defined to be equal to PA66 component to correctly capture the final reduction of sample thickness. The resulting densities are provided in Table 5.5.

Table 5.5 A full set of thermal transport properties of each condensed-phase component.

Component	ρ (kg m^{-3})	ε	κ (m^2 kg^{-1})	k (W m^{-1} K^1)
PA66	1173	0.95	2	$0.08+2\times10^{-4}$ T
PA66_Melt	1173	0.95	26.5	0.22
PA66_Res1	974	0.945	51	0.1
PA66_Res2	974	0.94	75.5	0.06
PA66_Res3	1173	0.94	100	0.06
GF	2600	0.81	1.6	0.36
GF_Melt	400	0.84	26.2	0.09
GF_Res1	2600	0.87	50.8	0.85
GF_Res2	510	0.91	75.4	0.85
GF_Res3	349	0.94	100	1×10^{-10} T^3
RP	2000	0.95	30	0.06
PA66_RP	600	0.95	28.3	0.15
PA66_RP_Res1	65	0.94	100	$-0.07 + 8\times10^{-10}$ T^3
PA66_RP_Res2	350	0.94	100	0.13
PA66_RP_Res3	180	0.94	100	8×10^{-10} T^3

Figure 5.7 depicts the averaged experimental back surface temperatures (black dashed line) and MLR data (symbol) of pure PA66 exposed to radiant fluxes at 60 kW m^{-2}. Shaded area corresponds to the maximum and minimum temperatures across the sample surface from the repeated experiments. The error bars of MLR data were computed as two standard deviations of the mean. The temperature profile was cropped at the time when 70 wt. % of the sample was decomposed. This was done because the

1D assumption was not valid after a majority of sample was consumed. Toward the end of the experiments, the residue had a tendency to agglomerate in the center rather than remain as a uniform layer.

The thermal conductivity, k, of these five condensed-phase components were determined through the inverse analysis of back surface temperature profile. It is worth noting that the thermal conductivities are the only undefined properties. The data of 0 - 100 s, 100 - 150 s, and 150 - 200 s at 60 kW m^{-2} in Figure 5.7(a) were inversely modeled to determine the thermal conductivities of PA66, PA66_Melt, and PA66_Res1, respectively. The data of 200 - 275 s at 60 kW m^{-2} in Figure 5.7(a) were fitted to determine the thermal conductivity of PA66_Res2 and PA66_Res3 that were produced at a high temperature. The principle of the inverse fitting process is to keep the smallest parameter set as possible while the agreement between the experimental and modeled curves is within the experimental uncertainties on average. The resulting thermal conductivities are reported in Table 5.5. The pyrolysis model, that included thermal transport properties determined in this section and the reaction parameters determined in Section 5.1.2 and summarized in Tables 5.1-5.3, was employed to produce the temperature profile obtained at 60 kW m^{-2}, shown as the red solid line in Figure 5.7(a).

The developed pyrolysis model of pure PA66 was employed to predict the experimental MLR data of pure PA66 obtained at 60 kW m^{-2}. These MLR data were not utilized in the inverse analysis model calibration and served as the model validation. The predicted MLR data are shown as a red solid line in Figure 5.7(b). The model predicts the experimental MLR profiles well with the exception of an abrupt MLR

decrease to zero at the end. This is likely due to the invalid 1D assumption at the end of the experiment when the residue agglomerated in the center rather than remained as a uniform layer.

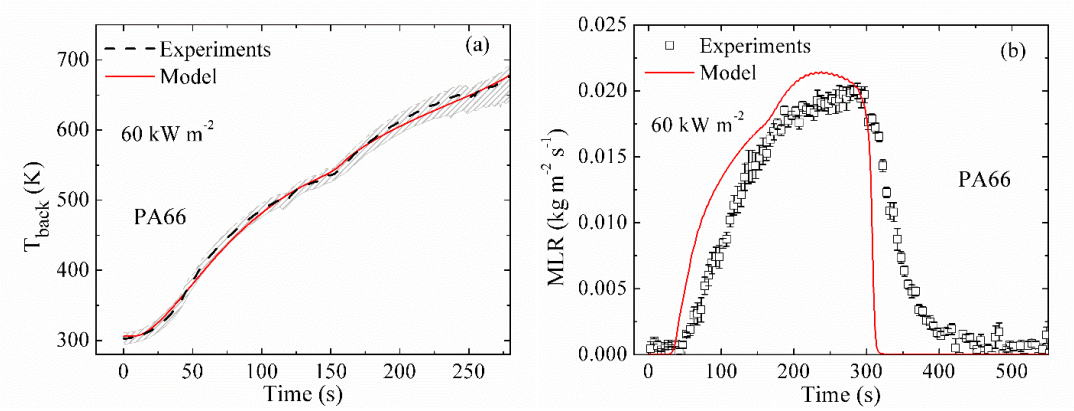

Figure 5.7 Experimental and simulated (a) back surface temperatures and (b) MLR data of pure PA66 exposed to radiant flux set at 60 kW m^{-2}. Shaded area corresponds to the maximum and minimum experimental temperatures across sample surface from repeated tests.

5.2.3 Pyrolysis Model Development for PA66/GF25

The resulting material properties of pure PA66 in Section 5.2.2 remained identical and were employed to characterize the pyrolysis model of PA66/GF25. As was discussed in Section 5.2.1, GF was assumed to evolve in the same manner as PA66 to account for the changes in thermal transport interaction between PA66 and GF associated with PA66 decomposition. Therefore, the thermal transport properties of GF-based components were estimated to capture the experimental measurements of PA66/GF25.

The emissivity of GF was assumed to be the same as that in PBT-based system (see Section 6.2.3). The absorption coefficient of PA66/GF25 was measured using the method described in Section 3.2.1. The absorption coefficient of GF was calculated by subtracting the value of PA66 from the value of PA66/GF25 based on their mass-weighted contributions. The emissivity and absorption coefficient of final residual component, GF_Res3, were defined as 0.94 and 100 $m^2 kg^{-1}$ in the same manner as the final product of PA66 decomposition, PA66_Res3. The emissivity and absorption coefficient of these intermediate components, GF_Melt, GF_Res1, and GF_Res2, were defined to be equally spanned between the values of initial GF and GF_Res3. The resulting emissivity and absorption coefficients are summarized in Table 5.5.

The density of PA66/GF25 was measured at room temperature. The density of GF was determined by the known density of PA66 and mass composition of PA66/GF25. The densities of GF_Melt, GF_Res1, GF_Res2, and GF_Res3 were determined to capture the observed sample thickness of PA66/GF25. The resulting densities are summarized in Table 5.5.

Subsequently, the back surface temperature data of PA66/GF25 at 30 kW m^{-2} and 60 kW m^{-2} in Figure 5.8 were inversely modeled to determine the thermal conductivities of GF-based components. The thermal conductivities are the only undefined parameters for characterizing the pyrolysis of PA66/GF25. The temperature data of 0 - 250 s and 250 - 500 s at 30 kW m^{-2} in Figure 5.8(a) were used to determine thermal conductivities of GF and GF_Melt. The temperature data of 500 - 800 s and 800 - 1350 s at 30 kW m^{-2} were used to determine the conductivities of GF_Res1 and GF_Res2. The temperature data of 400 - 600 s at 60 kW m^{-2} in Figure 5.8(b) were

employed to determine the thermal conductivity of GF_Res3 because GF_Res3 is the dominant component. Due to the high porosity and temperature of the residue, radiation was assumed to be the dominant mode of heat transfer inside the residue. The radiation diffusion approximation [130] was used to describe the thermal conductivity of the residual component, GR_Res3, with a third-power temperature dependence. The resulting thermal conductivities were adjusted to fit the temperature data within the experimental uncertainties at both heat fluxes. The simulated temperature profiles are shown as the red solid lines in Figure 5.8.

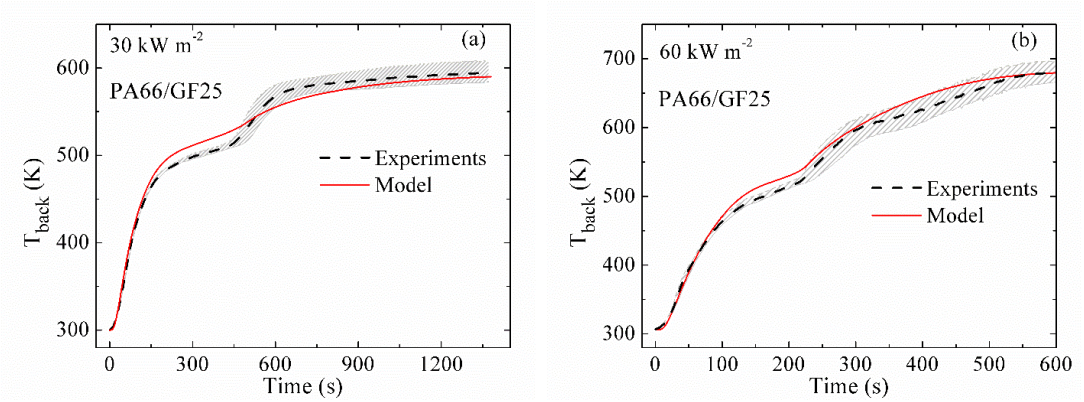

Figure 5.8 Experimental and simulated back surface temperatures of PA66/GF25 exposed to radiant fluxes set at (a) 30 kW m^{-2} and (b) 60 kW m^{-2}. Shaded area corresponds to the maximum and minimum experimental temperatures across the sample surface from repeated tests.

The pyrolysis model developed in the previous sections was employed and validated against the MLR data of PA66/GF25 obtained at 30 kW m^{-2} and 60 kW m^{-2} that were not utilized in the model parameterization. Figure 5.9 shows the experimental (symbols) and predicted (blue dotted lines) MLR data at both heat fluxes. The MLR peaks were underestimated by 25% and 45% at 30 kW m^{-2} and 60 kW m^{-2}, respectively.

An additional analysis was conducted to understand the cause of this poor agreement. First, the temperature profiles and MLR data of pure PA66 in Figure 5.7 were well captured, which indicated the accuracy of the reaction parameters and thermal transport parameters of pure PA66. Second, the well-captured temperature profiles of PA66/GF25 in Figure 5.8 indicated the accuracy of the thermal transport parameters of GF-based components. It is noted that the thermal conductivity definitions were experimented and none of the attempts to redefine thermal conductivities lead to improvement in the MLR prediction. Therefore, the significantly underestimated MLR data of PA66/GF25 in Figure 5.9 demonstrated that additional mass transport features should be included.

According to the literature information, the wick effect or capillary action was observed in the glass fiber reinforced polymers [96,97,103]. Wick effect of glass fiber resulted in an accelerated flow of the molten polymer along the smooth and high-energy glass fiber surface to the top flame zone [97]. Due to the wick effect, the molten polymer is transported from regions of higher concentration to regions of lower concentration. The known wick effect of glass fiber is a possible explanation for the underestimated MLR data.

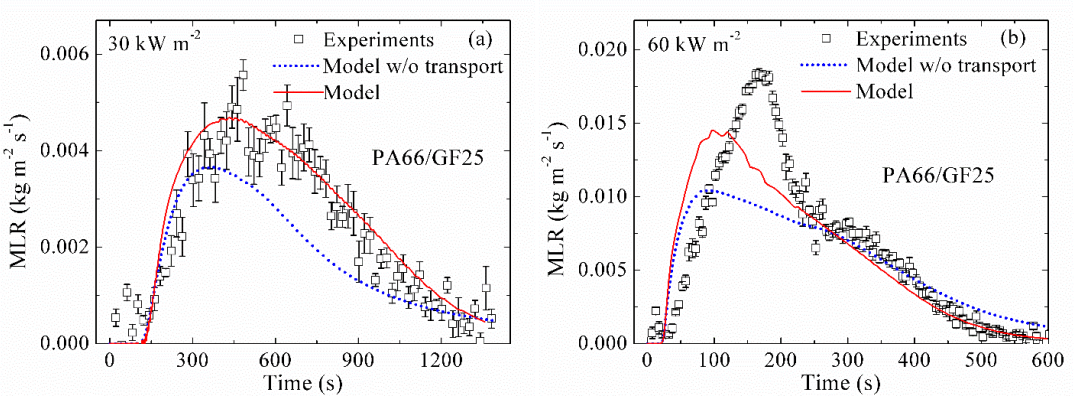

Figure 5.9 Experimental and predicted MLR data of PA66/GF25 exposed to radiant fluxes set at (a) 30 kW m^{-2} and (b) 60 kW m^{-2}.

The existence of wick effect was subsequently confirmed through experimental measurements. If the transport behavior exists during the gasification test of PA66/GF25, the molten polymer will migrate from the bottom layer to the top layer where the concentration of molten polymer is lower due to an earlier decomposition of PA66. Therefore, the concentration of the final residual component, PA66_Res3, in the top layer of PA66/GF25 residue obtained from CAPA II test at 60 kW m^{-2} (fully decomposed) is expected to be higher than that of the fully decomposed virgin sample without transport. To examine this hypothesis, the concentrations of the final residual component for both samples were estimated and compared to determine the presence of the transport behavior. Figure 5.10 details the three-step examination process and results. The first step was to obtain Sample A from the top layer of virgin PA66/GF25 sample, and Sample B from the top layer (~ 1 mm) of PA66/GF25 residue after the CAPA II test at 60 kW m^{-2}. The second step was to heat Sample A and Sample B (4 - 7 mg) up to 600 ℃ in N_2 at a prescribed heating rate of 10 K min^{-1} in TGA tests. The small sample mass and low heating rate allowed us to assume that the sample was thermally thin (no significant concentration and temperature gradient inside the sample). The second step was conducted to ensure that both samples were fully decomposed into final residual component, PA66_Res3. The third step was to re-heat the residue of both samples after the second step up to 600 ℃ in air at a prescribed heating rate of 10 K min^{-1}. The change in the mass of the samples observed in the air experiments was indicative of how much of the final residual component, PA66_Res3,

each sample contained (unlike the glass fiber, PA66_Res3 fully oxidizes and volatilizes when heated in the presence of oxygen). The mass loss of Sample B was twice larger than that of Sample A. This was because due to the wick effect, the molten polymer migrated to the top layer where the PA66 decomposed earlier and the concentration of molten polymer was lower. This larger mass loss of Sample B confirmed the existence of wick effect.

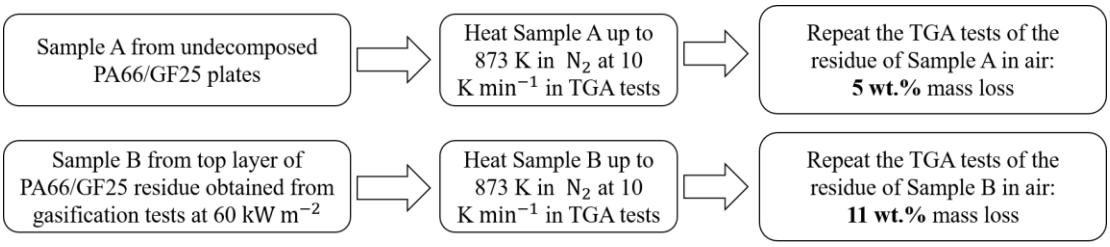

Figure 5.10 Three-step confirmation process of the existence of wick effect

Therefore, the wick effect or transport behavior was included in the current pyrolysis model. Both molten polymer and the first decomposition intermediate product, PA66_Melt and PA66_Res1, were assumed to be capable of undergoing the transport process because of their apparent low viscosity. The transport rate was characterized by a single mass transport coefficient. The value of the transport coefficient was determined to be 3.3×10^{-8} m^2 s^{-1} through inversely modeling the MLR data of PA66/GF25 obtained at 30 kW m^{-2}. All other material properties remain identical as in the previous model (without transport). The new transport model was checked against the MLR data of PA66/GF25 obtained at 60 kW m^{-2}. The simulated MLR profiles at both heat fluxes using the new transport model are shown as the red solid lines in Figure 5.9. It captures the MLR peak at 30 kW m^{-2} very well. The prediction of the magnitude of MLR peak at 60 kW m^{-2} is improved by 25%. However,

the magnitude and temperature of MLR peak at 60 kW m^{-2} are still underestimated. The underestimations were likely due to fact that the transport behavior may also depend on the temperature gradients inside the sample and thus cannot be fully characterized by a single transport coefficient. However, no more complexity of the transport behavior was included to avoid further complicating the model because the increased dependence of transport behavior on the higher external heat flux was less notable when flame retardant additive was added. The evidence of the less notable dependence is provided in Section 5.2.4. The new transport model was also employed to simulate the back surface temperature profiles of PA66/GF25. No significant difference was identified between the simulated temperature results calculated by the model with transport and the model without transport. The red solid lines in Figure 5.8 represent the simulated temperature profiles for both models with and without transport.

5.2.4 Pyrolysis Model Development for PA66/GF/RP Blends

Figure 5.11 shows the back surface temperature profiles of PA66/GF25-RP1.5 at 40 and 60 kW m^{-2}. The experimental results of lower RP concentration blend, PA66/GF25-RP1.5, were used to parameterize the properties of component in Reactions (5-7) in Table 5.1. They were not employed for Reactions (8-9) in Table 5.1 because these two reactions were inactive when RP concentration was low. It was assumed that RP component had the same transport rate as PA66_Melt and PA66_Res1. The rest of the RP-based components did not transport. The emissivity of RP was assumed to be the same as that of PA66 due to a small amount of RP in the blend. The absorption coefficient of PA66/GF25-RP1.5 was measured using the

method explained in Section 3.2.1. The absorption coefficient of RP was calculated by subtracting the values of PA66 and GF from the values of PA66/GF25-RP1.5 based on their mass-weighted contributions. PA66_RP_Res1 was one of the final decomposition products and thus its emissivity and absorption coefficient were defined to be 0.94 and 100 m^2 kg^{-1} in the same manner as the final residual component, PA66_Res3. The emissivity and absorption coefficient of interaction product, PA66_RP, were assumed to be the same as the averaged values of PA66_Melt and RP.

The density of PA66/GF25-RP1.5 was measured at room temperature. The density of RP was calculated based on the sample mass, material composition of PA66/GF25-RP1.5, and densities of PA66 and GF. It was observed that at 40 kW m^{-2}, the sample thickness of PA66/GF25-RP1.5 had an increase of 2 mm at the end, and at 60 kW m^{-2}, the sample thickness remained unchanged throughout the test. The densities of PA66_RP and PA66_RP_Res1 were defined to capture the sample thickness evolution. The resulting parameters are summarized in Table 5.5.

Figure 5.11 shows the mean experimental back surface temperatures (dashed line) of PA66/GF25-RP1.5 at both 40 kW m^{-2} and 60 kW m^{-2}. These temperature profiles were employed to determine the only remaining undefined thermal conductivities. The temperature data of 0 - 250 s and 250 - 600 s at 40 kW m^{-2} were used to determine the thermal conductivity of RP and PA66_RP. The temperature data of 450 - 800 s at 60 kW m^{-2} were used to determine the thermal conductivity of PA66_RP_Res1 since it was produced at a relatively high temperature. Due to the high porosity and temperature of the residue, radiation was assumed to be the dominant mode of heat transfer inside the residue. The radiation diffusion approximation [130]

was used to describe the thermal conductivity of the residual component, PA66_RP_Res1, with a third-power temperature dependence. These resulting conductivities were adjusted in order to fit both temperature profiles within the experimental uncertainties. The resulting parameters are summarized in Table 5.5. The simulated results are shown as the red solid lines in Figure 5.11. The model captures the profiles well except for a slight overestimation of temperature data from 200 - 450 s at 40 kW m^{-2}.

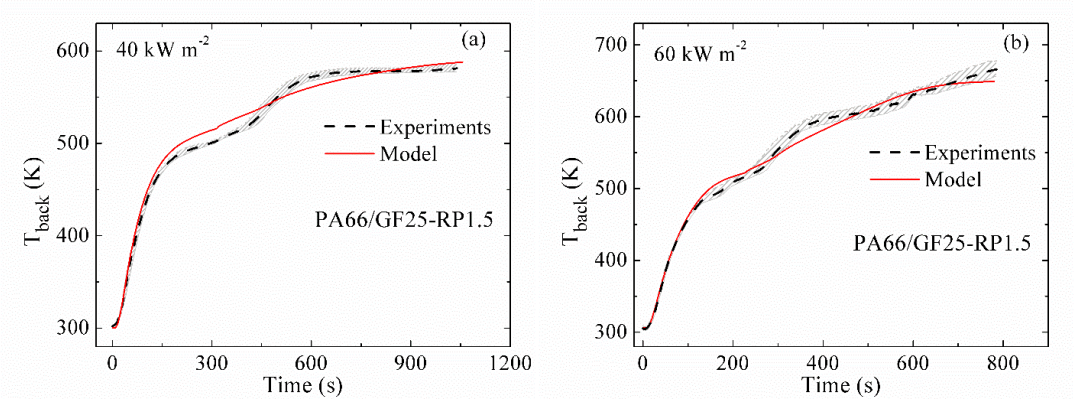

Figure 5.11 Experimental and simulated back surface temperatures of PA66/GF25-RP1.5 exposed to radiant fluxes set at (a) 40 kW m^{-2} and (b) 60 kW m^{-2}. Shaded area corresponds to the maximum and minimum experimental temperatures across the sample surface from repeated tests.

The experimental results of PA66/GF25-RP6.0 were inversely modeled to determine the properties of components in Reactions (8-9) in Table 5.1. PA66_RP_Res2 was a product preceding the final residual component, PA66_RP_Res3. Therefore, the emissivity and absorption coefficient of PA66_RP_Res2 and PA66_RP_Res3, were defined to be equal to those of other final decomposition residues, 0.94 and 100 m^2 kg^{-1}. The sample thickness of PA66/GF25-

RP6.0 was increased by 3 mm at the end for both heat fluxes. The densities of PA66_RP_Res2 and PA66_RP_Res3 were defined to capture this increase in sample thickness. The resulting parameters are summarized in Table 5.5.

Figure 5.12 shows the back surface temperature profiles of PA66/GF25-RP6.0 at 40 and 60 kW m^{-2}. The temperature data of 800 - 1250 s at 40 kW m^{-2} were used to determine the thermal conductivity of PA66_RP_Res2. The temperature data of 600 - 950 s at 60 kW m^{-2} were used to determine the thermal conductivity of PA66_RP_Res3 since it is the dominant component within such a high temperature range. These resulting thermal conductivities were adjusted in order to fit both temperature profiles within the experimental uncertainties. The simulated results are shown as the red solid lines in Figure 5.12. The resulting thermal conductivities are reported in Table 5.5.

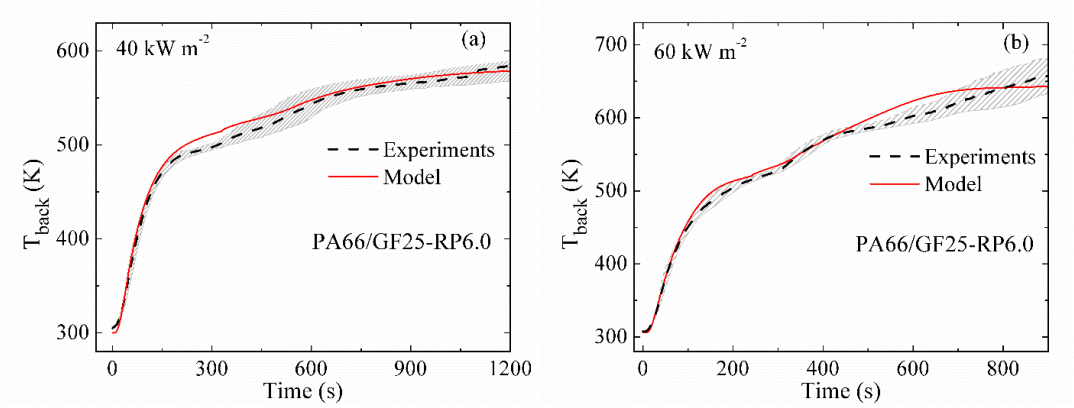

Figure 5.12 Experimental and simulated back surface temperatures of PA66/GF25-RP6.0 exposed to radiant fluxes set at (a) 40 kW m^{-2} and (b) 60 kW m^{-2}. Shaded area corresponds to the maximum and minimum experimental temperatures across the sample surface from repeated tests.

Subsequently, the MLR data of both RP-containing blends obtained at 40 kW m^{-2} and 60 kW m^{-2}, not utilized in the inverse analysis model calibration, were used to further validate the properties determined in this section. Figure 5.13 shows the experimental and predicted MLR data of PA66/GF25-RP1.5 and PA66/GF25-RP6.0 at 40 kW m^{-2} and 60 kW m^{-2}. When RP was added, the experimental MLR peaks at 60 kW m^{-2} were reduced compared to those of PA66/GF25. Additionally, as more RP was added, a greater reduction in the MLR peak was obtained. The pyrolysis model reasonably predicts the MLR data of both blends at both heat fluxes except for an underestimation in the magnitude and temperature of MLR peak of PA66/GF25-RP1.5 at the higher heat flux shown in Figure 5.13(b). Similar underestimation was observed in the predictions of the MLR data of PA66/GF25 in Figure 5.9(b). The underestimation was likely due to fact that the transport behavior may also depend on the temperature gradients inside the sample, which is not captured by the model. The underestimation was not present at the high RP concentration, as indicated by Figure 5.13(d). This observation indicates that, as was already discussed in Section 5.2.3, the addition of the flame retardant reduces the impact of the wick effect at high heating intensity.

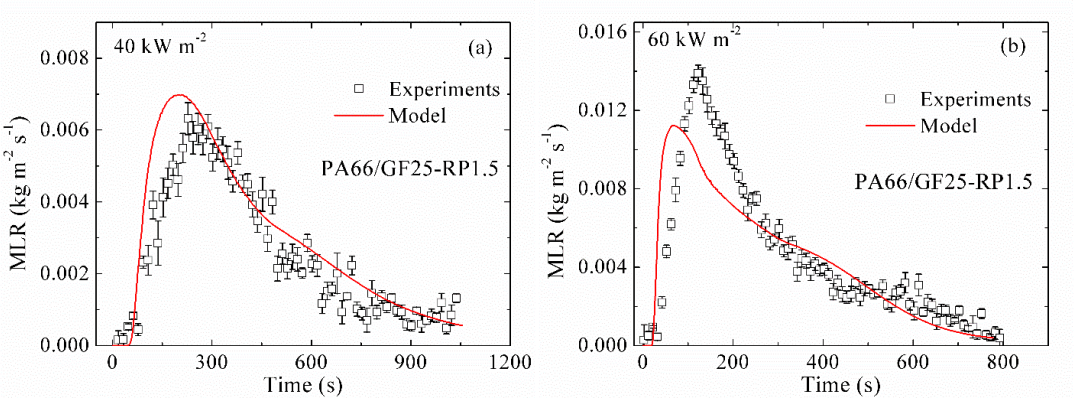

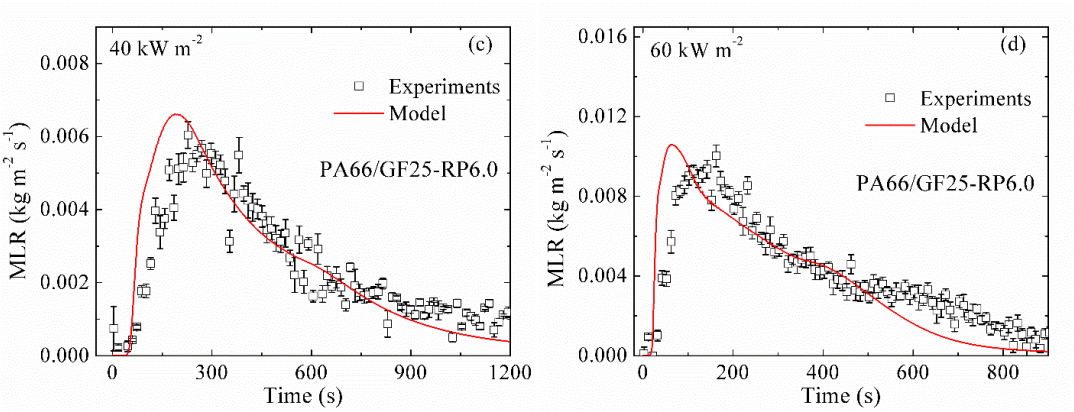

Figure 5.13 Experimental and predicted MLR data of (a) (b) PA66/GF25-RP1.5 and (c) (d) PA66/GF25-RP6.0 exposed to radiant fluxes set at 40 kW m^{-2} and 60 kW m^{-2}.

5.2.5. Extrapolation to New Compositions

The pyrolysis model that was derived from previous sections was capable of capturing the back surface temperature and MLR data of all four calibrated PA66/GF/RP blends for any thermal exposure. In this section, the extrapolating capability of the resulting model was validated against data obtained for two blends with new compositions, PA66/GF25-RP4.5 and PA66/GF25-RP9.0. The RP concentration of one blend lied in between and another one had a higher RP concentration than those of calibrated blends.

Figure 5.14 shows the experimental and predicted back surface temperature and MLR data of these two blends at 45 kW m^{-2}. No significant difference was observed in the experimental results for the two blends. It should be noted that these experimental measurements were not employed in the model parameterization process. The model predicts the experimental temperature data of both blends very well except for an overestimation of the temperature data between 200 - 400 s for PA66/GF25-RP4.5.

However, the model provides reasonable predictions considering the complexity of the pyrolysis model and the blends.

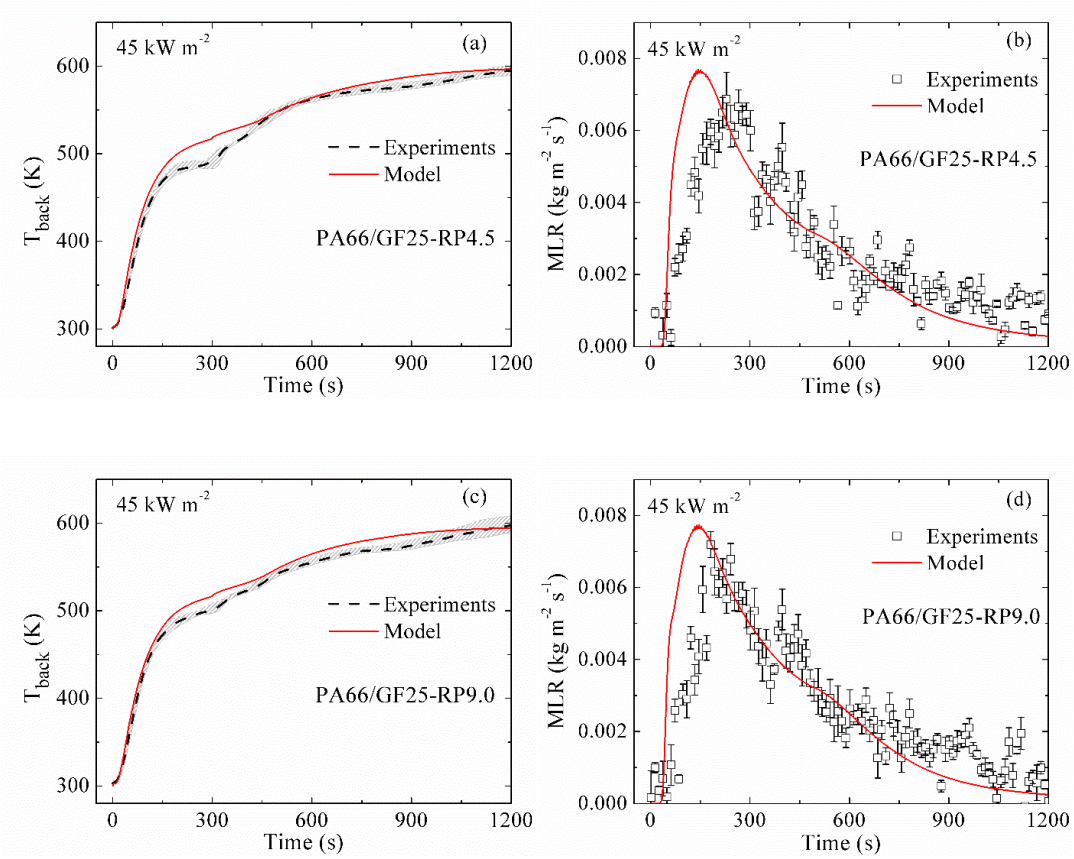

Figure 5.14 Experimental and predicted T_{back} and MLR data of (a) (b) PA66/GF25-RP4.5 and (c) (d) PA66/GF25-RP9.0 exposed to radiant flux set at 45 kW m^{-2}.

5.2.6. Impact of Flame Retardant Additive on HRR of Burning Blends

Additional simulations were conducted to understand the impact of the flame retardant additive on the fire performance of the blends. HRR is a critical parameter to assess the fire hazard of a material. Therefore, a simple 1D simulation that mimics the cone calorimetry experiment was conducted. In the simulation, a 4.0×10^{-3} m thick sample was subjected to an external radiant heat flux of 50 kW m^{-2} incident to the top

sample surface. This heat flux represents the heat flux corresponding to surface heating from small laminar flames [131] up to fully involved room fires [132]. The heat flux was constant throughout the entire simulation. The convective heat losses from the top sample surface were neglected and the bottom sample surface employed adiabatic boundary conditions. The simulation neglected the potential impact of sample surface oxidation prior to ignition. Moreover, the additional heat flux provided by the flame that formed on the sample surface upon ignition was also ignored in these simulations. An idealistic scenario was simulated to eliminate the effect of imperfection of experimental setup on evaluating the fire behavior of a material. It is noted that this work is also capable of simulating more complex experimental scenarios. The calculations were terminated when no additional mass loss was observed. The rates of gaseous fuel production or MLR, of the burning sample were computed by ThermaKin2Ds using the developed pyrolysis model. The product of the resulting MLR and the complete heats of combustion of gaseous products obtained in MCC [110] yielded the HRR of the burning sample.

A comparison of the simulated HRR profiles for four blends with varied compositions exposed to radiant heat flux set at 50 kW m^{-2} is shown in Figure 5.15(a). The incorporation of RP significantly reduced the magnitude of HRR and the integral HRR by about 38% and 12% on average compared to that of PA66/GF25. It is noted that the pyrolysis model developed in this work underestimates the experimental MLR peak of PA66/GF25 at 60 kW m^{-2} approximately by 20%, shown in Figure 5.9(b). Therefore, it is expected that the role of RP in reducing the HRR and integral HRR is more significant when the underestimations are eliminated. Figure 5.15(a) also shows

that no significant differences in these HRR profiles are identified with the RP composition changing from 2.0 wt. % to 9.0 wt. %. Similar trend was observed in the experimental HRR data obtained from actual cone calorimeter tests. The actual experimental data were not shown in the present work due to a confidential disclosure agreement between BASF and University of Maryland. Some previous studies [90,133] also showed that no further improvement on HRR reduction was achieved when the RP concentration was higher than a certain value.

Figure 5.15(b) shows the corresponding simulated MLR profiles, which have the similar trend as HRR profiles. The incorporation of RP reduces the magnitude of MLR by about 30% on average. The additional 8% reduction in HRR data compared to the MLR data indicates that RP plays a role in the gas-phase fuel dilution. A parameter sensitivity analysis demonstrates that the thermal transport properties of RP-based components are primarily responsible for the observed reduction in the MLR and HRR data. In other words, RP chemically reacts with PA66 and produces condensed-phase products that act as a thermal barrier. The excess amount of RP vaporized instead of interacting with PA66-based components, which did not further affect the thermal transport process and thus no additional reduction was seen in the MLR and HRR data. It is worth noting that the gas-phase flame inhibition effect of RP [90,134] was not considered as the heats of combustion were obtained from MCC wherein all volatiles were forced to complete combustion. Additional work that also accounts for its combustion efficiency impact is required to completely assess the role of RP in improving a material's fire performance.

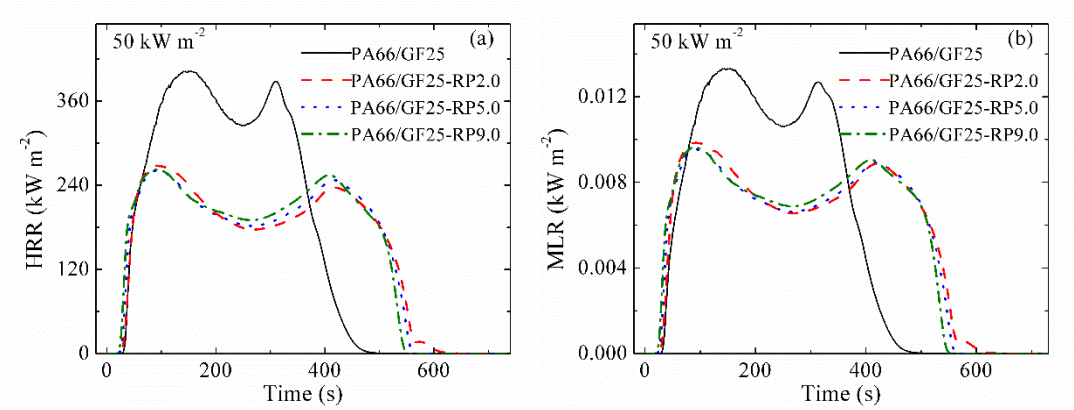

Figure 5.15 Simulated area-normalized (a) HRR and (b) MLR data of PA66/GF25, PA66/GF25-RP2.0, PA66/GF25-RP5.0, and PA66/GF25-RP9.0 exposed to radiant fluxes set at 50 kW m^{-2}.

5.3 Summary

Chapter 5.1 outlined an approach to develop a reaction model that predicted the thermal decomposition behavior of a thermoplastic blended with a condensed-phase-active flame retardant. This approach was based on TGA, DSC and MCC experiments and inverse numerical modeling of their results. While the developed model does not resolve chemical species involved in the decomposition process, it does capture all essential aspects of thermal decomposition behavior relevant to the material's ability to sustain and grow fire. Moreover, through the introduction of two-component reactions, this model gained a capability to provide accurate prediction of thermal decomposition dynamics for a material of any composition that consisted of the same initial components (in this case: PA66, RP and GF).

Chapter 5.2 detailed a combined experimental and modeling methodology to develop a pyrolysis model for PA66/GF/RP based on the reaction model constructed

in Chapter 5.1. The decomposition kinetics and thermodynamics obtained from Chapter 5.1 served as a core subset of the model inputs. The remaining required model inputs that define mass and heat transport within the condensed-phase were estimated through inversely modeling the simultaneous measurements of MLR, T_{back}, and sample thickness obtained from CAPA II experiments. The resulting single pyrolysis model was capable of quantitatively relating the flammability behavior to material composition.

The wick effect of glass fiber was revealed during the pyrolysis model construction and incorporated into the pyrolysis model to improve the accuracy of MLR data predictions. The addition of RP reduced the dependence of the wick effect on the temperature gradients in the condensed-phase. The resulting new pyrolysis model with the wick effect predicted the MLR profiles of all the tested blends at a heat flux ranging from 30 to 60 kW m^{-2} with an approximate error of 15% on average.

Chapter 5.2 provided a quantification of the action of the flame retardant additive (RP) on the fire behavior of a PA66/GF/RP blend and an understanding of the physical and/or chemical phenomena responsible for its action. It was concluded that when the gas-phase combustion inhibition effect was excluded, the impact of RP on the HRR was significant (38% reduction in the magnitude of HRR). The RP-based components are primarily responsible for the observed significant reduction in the HRR. No significant difference in the HRR reduction was observed when the concentration of RP changed from 2 wt.% to 9 wt.%. The RP appeared to provide no additional improvements to the HRR when added in excess of 2 wt.% because the surplus RP simply vaporized without interacting with other components. The addition of RP

reduced the magnitude of MLR data by only 30%, which indicated that RP also acted through fuel dilution.

Chapter 6. Characterization of PBT/GF/DEPAL/MPP Blends

6.1 Milligram-scale Results and Analysis

6.1.1 Overall Approach to Reaction Model Development for PBT/GF/DEPAL/MPP Blends

The development of a generalized reaction model for the PBT/GF/DEPAL/MPP blends consisted of five steps. In the first step, a PBT decomposition model was derived from the TGA and DSC data obtained for the PBT/GF25 blend. The GF component was assumed to be non-volatile and chemically inert.

In the second step, an attempt was made to simulate the TGA and DSC data obtained for the PBT/GF/DEPAL blends using a combination of the PBT decomposition model and DEPAL decomposition model, which was based on information available in the literature [135]. Significant differences between these simulations and experimental data were identified. These differences were interpreted as evidence of a chemical interaction between the polymer matrix and DEPAL. The reaction parameters of this interaction were initially estimated through a fitting of the TGA and DSC data obtained for PBT/GF25-DEPAL8 (a blend with a low concentration of DEPAL) and further adjusted by fitting of the data collected for PBT/GF25-DEPAL16 (a blend with a high concentration of DEPAL) until the best compromise in representing both data sets was achieved. In the third step, the same procedure was used to develop a reaction mechanism for the PBT/GF/MPP blends.

In the fourth step, the combined reaction model (including PBT, DEPAL, and MPP decomposition, PBT-DEPAL and PBT-MPP interactions) was employed to simulate experimental MCC data for all blends used for the reaction model development (see Table 6.1). Heats of combustion of all gaseous products were derived from these simulations. In the final step, the combined reaction model was validated by testing its ability to predict TGA and DSC data at heating rates and for material compositions not used in the model development process.

6.1.2 Inverse Modeling of TGA and DSC of PBT/GF25

The mean experimental results of TGA and DSC tests conducted on the PBT/GF25 material are shown as symbols in Figure 6.1. Figure 6.1(a) shows the dependence of sample mass and MLR normalized by the initial mass on temperature. Figure 6.1(b) contains the initial-sample-mass normalized heat flow and integral heat flow as a function of temperature. The error bars were calculated from the scatter of the experimental data as two standard deviations of the mean (Error bars that are comparable in size to the data symbols are omitted). The experimental MLR profile contains a single peak at 680 K corresponding to the thermal decomposition process. The decomposition produced 31.5 wt.% of residue including 25 wt.% of GF. The heat flow curve contains two distinct maxima. The first (500 K) and second (680 K) maxima represent melting and decomposition process, respectively.

Inverse modeling of the TGA and DSC data was performed using the same approach described in detail in Section 5.1.2. Only a brief description is provided here. A single first-order reaction was initially employed to model the TGA data. The stoichiometric coefficients of this reaction were initially set to capture the residue yield

observed in the TGA experiments. The Arrhenius parameters of this reaction were initially estimated using analytical expressions [136] relating these parameters to the temperature and height of the targeted MLR peak. Subsequently, these parameters were refined through a manually iterative process using ThermaKin2Ds until the modeling results were found to be in agreement with the experimental data. The reaction parameter manipulation was based on the following observations: an increase in the activation energy shifted the MLR curve to a higher temperature and reduced the height of the peak; an increase in the pre-exponential factor shifted the MLR curve to a lower temperature and increased the height of the peak. The agreement was declared to be satisfactory when the differences between the average experimental and modeled final mass residues, and temperatures and magnitudes of MLR maxima were found to be within 3%, 5 K, and 8%, respectively. If it was impossible to achieve such agreement, an additional reaction was added to the reaction scheme and its parameters were adjusted iteratively to achieve further improvement.

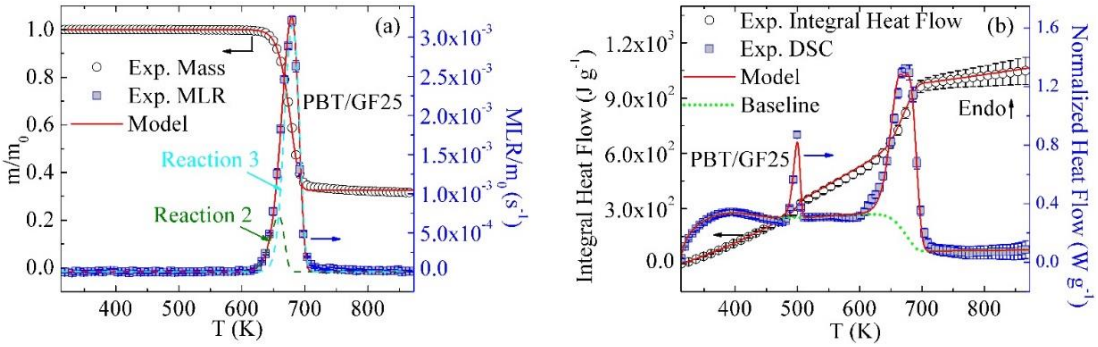

Figure 6.1 Experimental and simulated (a) TGA and (b) DSC data obtained for PBT/GF25 at 10 K min^{-1}.

In the case of PBT/GF25, two consecutive reactions, Reactions (2-3), were required to accurately capture the initial rise, maximum and final decay of the MLR.

These reactions are defined in Table 6.1. The component names used in the reaction definitions are self-explanatory. The reaction contributions to MLR profiles are depicted in Figure 6.1; their parameters are summarized in Table 6.2.

Table 6.1 Reaction mechanism for all the material is examined in this study.

Model	#	Reaction Equation
PBT	1	PBT → PBT_Melt
	2	PBT_Melt → 0.84 PBT_Res1 + 0.16 PBT_Gas1
	3	PBT_Res1 → 0.12 PBT_Res2 + 0.88 PBT_Gas2
PBT&DEPAL	4	DEPAL → 0.07 DEPAL_Res1 + 0.93 DEPAL_Gas1
	5	PBT_Melt + 3.6 DEPAL → 2.0 PBT_DEPAL_Res1 + 2.6 PBT_DEPAL_Gas1
PBT&MPP	6	MPP → 0.4 MPP_Res1 + 0.6 MPP_Gas1
	7	PBT_Res1 + 0.04 MPP → 0.92 PBT_MPP_Res1 + 0.12 PBT_MPP_Gas1
	8	PBT_MPP_Res1 → 0.07 PBT_MPP_Res2 + 0.93 PBT_MPP_Gas2

Table 6.2 Kinetics and thermodynamics of melting and decomposition reactions (positive heats of reaction, h, correspond to endothermic processes).

#	A (s^{-1} or $m^3\ kg^{-1}\ s^{-1}$)	E ($J\ mol^{-1}$)	h ($J\ kg^{-1}$)
1	2.0×10^{40}	4.00×10^5	6.0×10^4
2	2.0×10^{25}	3.41×10^5	1.4×10^5
3	2.4×10^{20}	2.90×10^5	3.1×10^5
4	1.0×10^{12}	2.09×10^5	0
5	2.0×10^{20}	3.19×10^5	2.4×10^6
6	2.5×10^{20}	2.88×10^5	6.9×10^5
7	2.0×10^{20}	2.70×10^5	1.5×10^5
8	2.5×10^{20}	2.87×10^5	4.0×10^5

The heat flow data were analyzed by first focusing on the regions not associated with melting or decomposition. The data corresponding to these regions were divided by the instantaneous heating rate and fitted with linear functions representing heat capacities of the corresponding condensed-phase components. The heat flow data

between 313 and 460 K and 510 and 590 K were used to determine the heat capacity of PBT and PBT_Melt, respectively. The heat capacity of GF was obtained from the literature [126]. The heat capacity of PBT_Res2 was impossible to resolve due to its small yield. Therefore, its heat capacity was assumed to be equal to the average heat capacity of chars produced by several common polymers, 1700 J kg^{-1} K^{-1} [46]. The heat capacity of the intermediate condensed-phase product (PBT_Res1) was assumed to be equal to the average heat capacity of the PBT_Melt and PBT_Res2. All heat capacity values are listed in Table 6.3.

The sensible heat flow baseline was subsequently calculated as a product of the mass fractions of condensed-phase components, whose temporal evolution was computed by ThermaKin2Ds, corresponding heat capacities and instantaneous heating rate. The baseline obtained for the PBT/GF25 is shown as a green dotted line in Figure 6.1(b). Subtraction of this baseline from the normalized experimental heat flow and subsequent integration of the differences yielded the values of the heat of melting and heats of decomposition, h. Reaction (1) (see Table 6.1) was added to the mechanism to simulate the melting process. The kinetics of this reaction and heats of melting and decomposition were refined until the overall heat flow curve simulated using ThermaKin2Ds was in agreement with the experimental data. This agreement was defined by the simulated heat flow maxima within 10%, temperatures of the maxima within 8 K, and the final integral heat flow value within 5% of the corresponding experimental data. The results of this exercise are shown in Figure 6.1(b). The heats of melting and decomposition reactions are listed in Table 6.2.

Table 6.3 Heat capacities of condensed-phase components.

Component	c (J kg^{-1} K^{-1})	Component	c (J kg^{-1} K^{-1})
PBT	$-524 + 5.60 \times T$	DEPAL_Res1	1700
PBT_Melt	$2100 + 0.20 \times T$	PBT_DEPAL_Res1	1700
PBT_Res1	$1900 + 0.10 \times T$	MPP	$-990 + 4.20 \times T$
PBT_Res2	1700	MPP_Res1	1700
GF	$442 + 1.24 \times T$	PBT_MPP_Res1	$1900 + 0.10 \times T$
DEPAL	$-2750 + 11.8 \times T$	PBT_MPP_Res2	1700

6.1.3 Inverse Modeling of TGA and DSC Data for PBT/GF/DEPAL Blends

Figure 6.2 displays the mean experimental results of TGA and DSC tests on PBT/GF25-DEPAL8 and PBT/GF25-DEPAL16 material systems. With the introduction of DEPAL, the MLR profiles gain an additional, barely discernable peak at 765 K. This peak becomes somewhat more evident as the concentration of DEPAL increases to 16 wt.%.

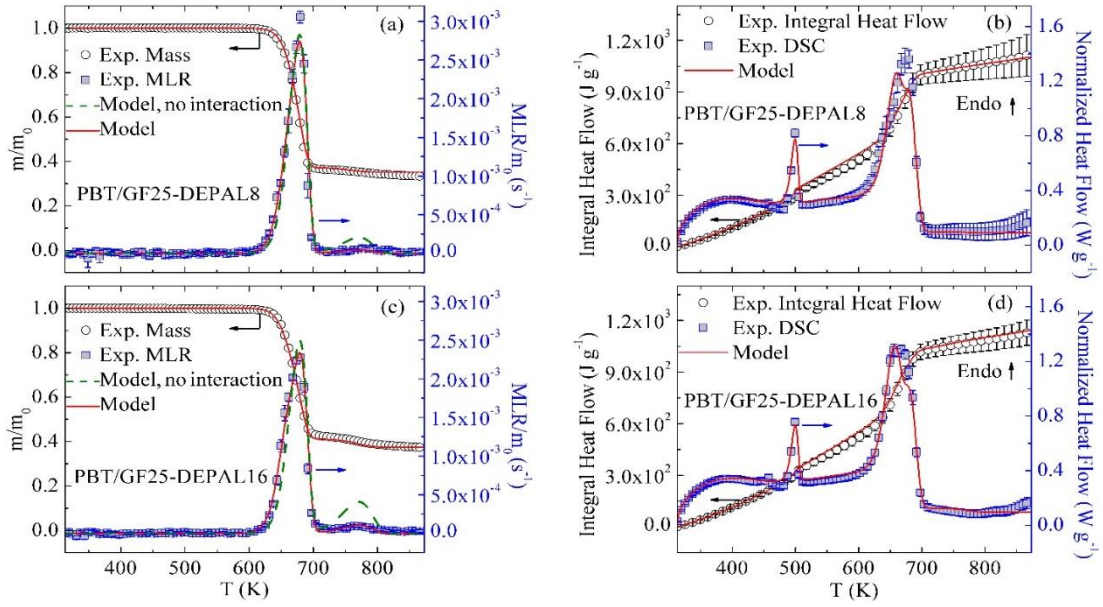

Figure 6.2 Experimental and simulated TGA and DSC data obtained for (a) (b) PBT/GF25-DEPAL8 and (c) (d) PBT/GF25-DEPAL16 at 10 K min^{-1}

Duquesne et al. [135] investigated the decomposition of pure DEPAL using TGA, which was conducted in nitrogen at a heating rate of 10 K min^{-1}. They found that DEPAL decomposed at about 750 K through a single step and produced 7 wt.% of final residue. Given a similarity between the position of the second MLR peak observed in this study and that of pure DEPAL, this second peak was attributed to DEPAL decomposition. Reaction (4) (see Table 6.1) was added to the mechanism to represent this process. The stoichiometric coefficients of this reaction were determined from Duquesne et al. results; the kinetic parameters were estimated based on the second MLR peak (765 K) observed in the current experiments.

The results of addition of Reaction (4) to the mechanism are shown as green dashed lines in Figure 6.2(a) and 6.2(c). These simulations significantly overestimate the size of the second MLR peak for both blends indicating that some DEPAL is consumed in a reaction with the polymer matrix prior to reaching its decomposition temperature. To account for this interaction, a reaction between PBT_Melt and DEPAL, Reaction (5) (see Table 6.1), was added to the mechanism. The stoichiometry and kinetics of this reaction were adjusted to correctly reproduce the experimental MLR peaks observed for the PBT/GF25-DEPAL8 and PBT/GF25-DEPAL16 blends. The final inverse modeling results using Reactions (1-5) (see Table 6.1) are shown in Figure 6.2(a) and 6.2(c) as red solid lines; the reaction parameters are summarized in Table 6.2. The first simulated MLR peak is still primarily associated with the decomposition of PBT_Melt, only a relatively small fraction of which is consumed in the reaction with DEPAL. The second simulated peak is associated with the decomposition of the portion of DEPAL that did not react with PBT_Melt.

The experimental heat flow data obtained for PBT/GF25-DEPAL8 and PBT/GF25-DEPAL16 in the temperature range between 313 and 460 K were used to determine the heat capacity of DEPAL. The sensible heat contributions of PBT and GF were subtracted from the heat flow data to determine DEPAL's contribution. Heat capacities of DEPAL_Res1 and PBT_DEPAL_Res1 components could not be determined from the heat flow data due to their small yields and, therefore, were assumed to be equal to the average heat capacity of chars produced by several common polymers, 1700 J kg^{-1} K^{-1} [46]. The heats of Reaction (4) and (5) (see Table 6.1) were subsequently determined by fitting the heat flow data for both blends. These final heat flow modeling results that agree with experimental results within the criteria defined in Section 6.1.2 are shown in Figure 6.2(b) and 6.2(d). The values of heat capacities and heats of reaction are reported in Table 6.3 and 6.2, respectively.

6.1.4 Inverse Modeling of TGA and DSC Data for PBT/GF/MPP Blends

The mean experimental results of TGA and DSC tests of PBT/GF25-MPP4 and PBT/GF25-MPP8 blends are shown as symbols in Figure 6.3. With the incorporation of MPP into the GF-reinforced PBT, the main MLR peak increases in height (by 20% upon addition of 4 wt.% of MPP) and becomes considerably more narrow in temperature. The char yield was not affected by the addition of MPP. An attempt was made to capture this behavior by adding a reaction of decomposition of MPP, Reaction (6) (see Table 6.1), to the mechanism. This reaction was parameterized by matching the final residue yield and temperature of the main MLR peak observed in the TGA experiments conducted in this work on pure MPP. However, as indicated by green dashed lines in Figure 6.3(a) and 6.3(c), the resulting model (no interaction)

significantly underestimated the heights of the main MLR peaks; the initial rise and final decay of the MLR curves were not captured. Also, the final residue yields were underestimated by about 5%. It was further deduced that it is the reaction of decomposition of PBT_Res1 (Reaction (3)) that was primarily responsible for the observed discrepancies. Therefore, a reaction between PBT_Res1 and MPP, Reaction (7) (see Table 6.1), was added to the model to compete with Reaction (3). Finally, one more consecutive reaction, Reaction (8) (see Table 6.1), was added to accurately capture the final decay of the MLR peaks observed for both blends. These inverse modeling results using Reactions (1-3) and (6-8) are shown in Figure 6.3(a) and 6.3(c) as red lines. The kinetic parameters of these additional reactions are summarized in Table 6.2.

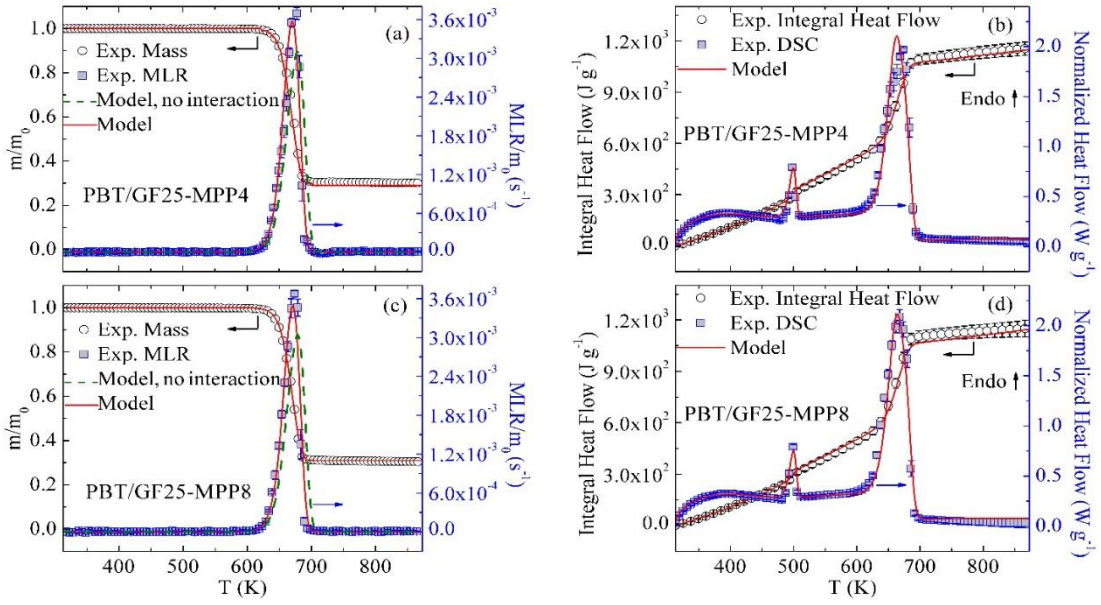

Figure 6.3 Experimental and simulated TGA and DSC data obtained for (a) (b) PBT/GF25-MPP4 and (c) (d) PBT/GF25-MPP8 at 10 K min^{-1}

The heat capacity of MPP was obtained in the same way as the heat capacity of DEPAL (see Section 6.3). The heat capacities of MPP_Res1 and PBT_MPP_Res2 could not be resolved and were assumed to be equal to the average heat capacity of chars produced by several common polymers, 1700 J kg^{-1} K^{-1} [46]. The heat capacity of PBT_MPP_Res1 was taken as the average heat capacity of PBT_Melt and PBT_MPP_Res2. The heats of Reaction (6-8) (see Table 6.1) were subsequently determined by fitting the heat flow data for both blends. The final heat flow modeling results are shown in Figure 6.3(b) and 6.3(d). The values of heat capacities and heats of reaction are reported in Table 6.3 and 6.2, respectively.

6.1.5 Inverse Modeling of MCC Data of PBT/GF/DEPAL/MPP Blends

The mean experimental HRR normalized by the initial sample mass and the integral HRR for PBT/GF25, PBT/GF25-DEPAL8, PBT/GF25-DEPAL16, PBT/GF25-MPP4, and PBT/GF25-MPP8 blends are shown as symbols in Figure 6.4. Initial comparisons between the experimental HRR and modeled MLR profiles generated using the heating rate temporal profiles specific to the MCC experiments revealed minor discrepancies that were attributed to sample/sensor temperature non-uniformities present in the MCC and associated with the use of open ceramic crucibles. To correct for these non-uniformities, the experimental HRR curves were shifted to a higher temperature by 5-10 K using the guiding principle that any detected heat release required a concurrent mass loss. The experimental data presented in Figure 6.4 are the shifted data; the original data are not presented because they are nearly indistinguishable from the shifted results.

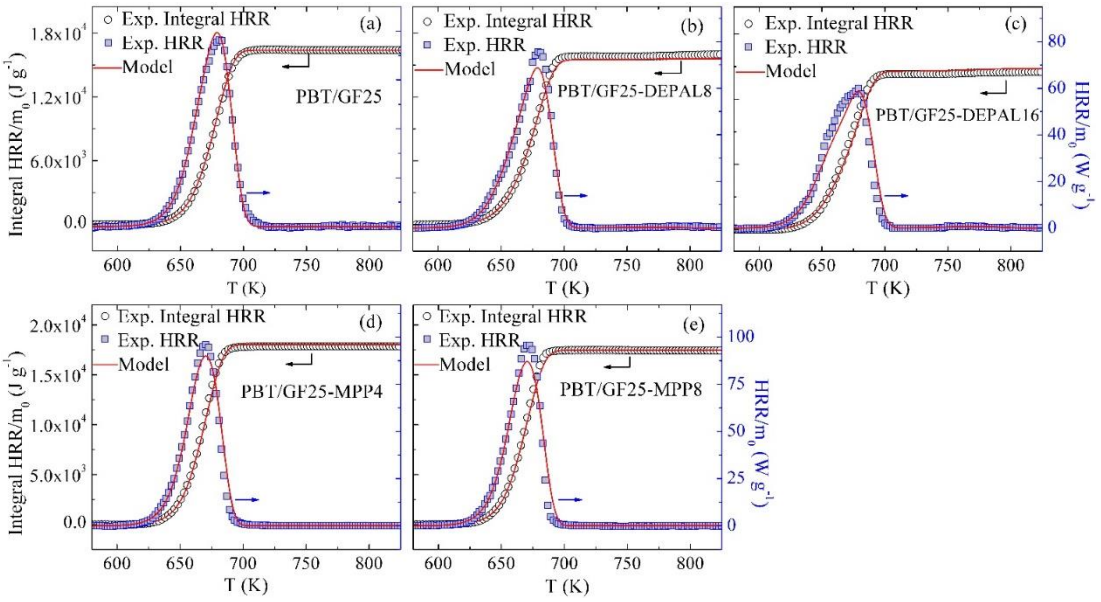

Figure 6.4 Experimental and simulated MCC data obtained for (a) PBT/GF25, (b) PBT/GF25-DEPAL8, (c) PBT/GF25-DEPAL16, (d) PBT/GF25-MPP4 and (e) PBT/GF25-MPP8 at 10 K min^{-1}

The heats of combustion of all gaseous products were first set to a single value that yielded the final integral HRR equal to that observed in the experiments. Subsequently, individual h_{com} values were adjusted up or down to capture the shapes of the experimental HRR peaks. As in the case of inverse modeling of TGA and DSC experiments, the iterative process continued until the differences between the modeled and experimental data satisfied specific criteria. These criteria were defined as differences of less than 8% between the values of HRR maxima, less than 10 K between the temperatures of the maxima and less than 8% between the final integral HRR values. The resulting heats of combustion that satisfy these criteria are given in Table 6.4. All h_{com} values are within the range, $0.7 - 3.8 \times 10^7$ J kg^{-1}, consistent with the

hydrocarbon nature of these gases [129]. The final simulated MCC results are shown in Figure 6.4.

Table 6.4 Heats of combustion of gaseous products

Component	h_{com} (J kg^{-1})	Component	h_{com} (J kg^{-1})
PBT_Gas1	2.1×10^7	PBT_DEPAL_Gas1	2.8×10^7
PBT_Gas2	2.5×10^7	MPP_Gas1	1.8×10^7
DEPAL_Gas1	0.7×10^7	PBT_MPP_Gas1	3.8×10^7
PBT_MPP_Gas2	2.5×10^7		

6.1.6 Model Performance at Different Heating Rates

The reaction mechanism shown in Table 6.1 and corresponding parameters reported in Tables 6.2-6.4 reproduce TGA, DSC, and MCC data collected at a nominal heating rate of 10 K min^{-1} for PBT/GF25, PBT/GF25-DEPAL8, PBT/GF25-DEPAL16, PBT/GF25-MPP4, and PBT/GF25-MPP8 blends with the accuracy defined by the criteria discussed in Section 6.1.2 and 6.1.5. To further validate this reaction model, the mean experimental TGA data obtained at lower, 5 K min^{-1}, as well as higher, 20 K min^{-1}, heating rates on the same blends were compared with the corresponding predictions. This comparison is summarized in Figure 6.5; no MLR data are shown on this figure to avoid congestion. Overall, good predictions were obtained for all blends and heating conditions. The model slightly (by 5-10 K) underestimates the temperatures of the onset of the experimental mass loss at 20 K min^{-1} for all blends, perhaps, due to some minor non-uniformities in the sample/sensor temperature arising at this heating rate (and not corrected for by the STA temperature sensor calibration, which was carried out at 10 K min^{-1}).

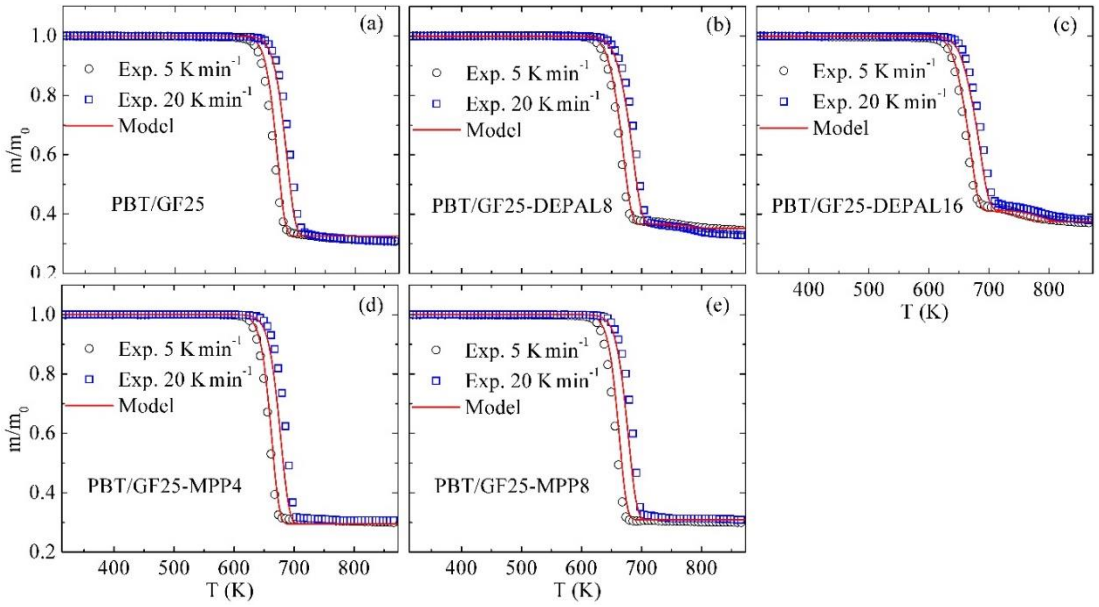

Figure 6.5 Experimental and simulated TGA data obtained for (a) PBT/GF25, (b) PBT/GF25-DEPAL8, (c) PBT/GF25-DEPAL16, (d) PBT/GF25-MPP4 and (e) PBT/GF25-MPP8 blends at 5 K min^{-1} and 20 K min^{-1}

6.1.7 Modeling of Different Material Compositions

To validate the model assumption that GF acts as an inert additive, TGA and DSC experiments were performed on pure PBT samples. The results of these experiments are compared with the model predictions in Figure 6.6. The experimental TGA data are in nearly perfect agreement with the model. The experimental heat flow is slightly underpredicted toward the end of the experiment. This discrepancy is likely to be associated with the uncertainties in the high temperature portion of the experimental heat flow baseline, which may not have been completely resolved in the five STA runs from which these data were derived (ten STA runs were used to generate all model calibration data).

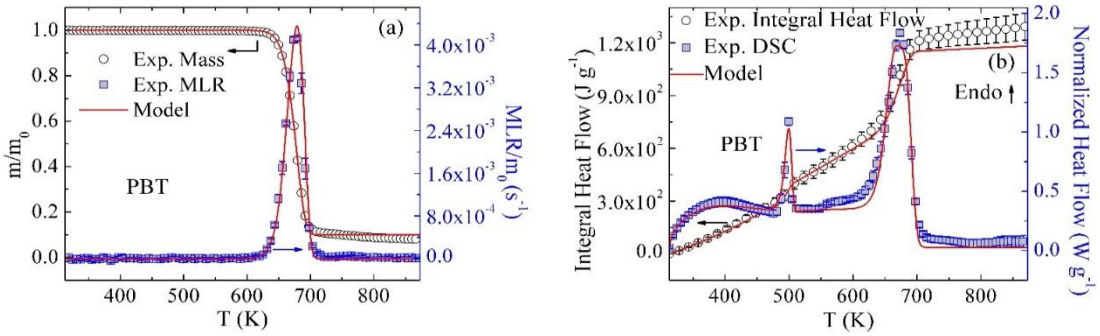

Figure 6.6 Experimental and simulated (a) TGA and (b) DSC data obtained for pure PBT at 10 K min^{-1}

Finally, the predictions of the reaction model were compared with the experimental results obtained for material blends containing both flame retardants (PBT/GF25-DEPAL8-MPP4 and PBT/GF25-DEPAL16-MPP8). This comparison is shown in Figure 6.7. The model captures all TGA and DSC experimental data well, with a possible exception of a slight overprediction of the maximum heat flows. In addition to validating the model, this comparison indicates absence of significant interactions between DEPAL and MPP additives. The same conclusion was reached by Samyn and Bourbigot who studied the thermal decomposition of DEPAL-MPP blends [107].

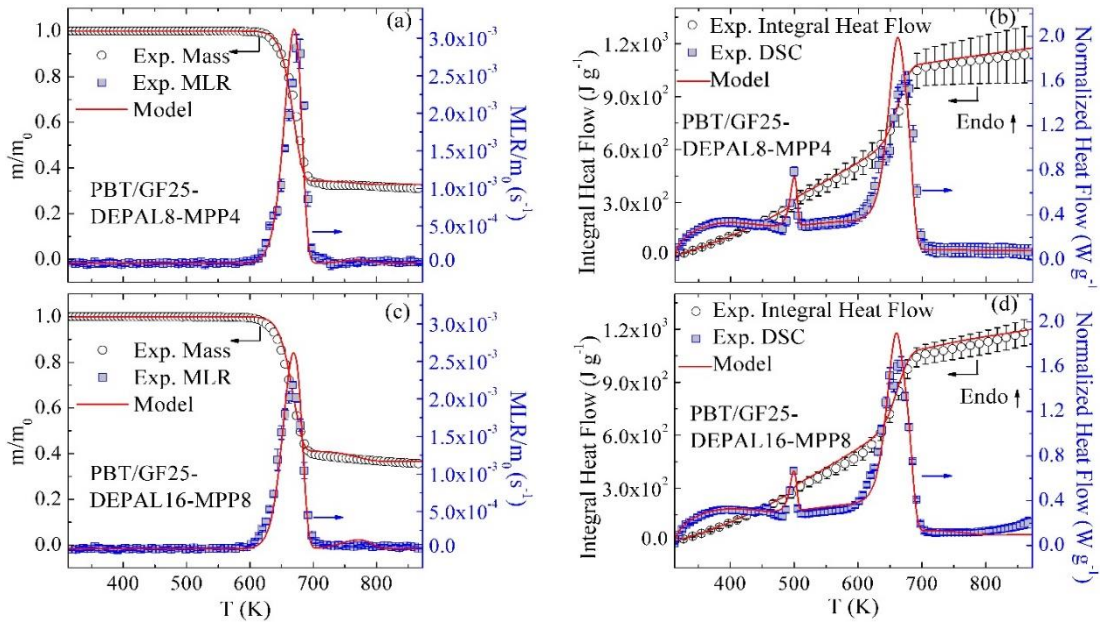

Figure 6.7 Experimental and simulated TGA and DSC data obtained for (a) (b) PBT/GF25-DEPAL8-MPP4 and (c) (d) PBT/GF25-DEPAL16-MPP8 at 10 K min^{-1}

6.2 Bench-scale Results and Analysis

6.2.1 Overall Approach to Pyrolysis Model Development for PBT/GF/DEPAL/MPP Blends

The pyrolysis model development of PBT/GF/DEPAL/MPP blends requires the measurement of the kinetics and thermodynamics of thermal decomposition, heats of combustion of gaseous products, and thermal transport properties. The kinetics and thermodynamics of thermal decomposition and heats of combustion of gaseous products have been parameterized through a manually iterative inverse analysis of milligram-scale experimental data in Section 6.1. The resulting reaction model along with the determined parameters summarized in Tables 6.1-6.4, are capable of predicting TGA, DSC, and MCC data of pyrolyzing blends as a function of material

compositions and heating conditions. The thermal transport properties were determined through an inverse analysis of the bench-scale gasification experimental results. The inverse analysis process for the pyrolyzing multi-component flame retardant blends consisted of five steps.

The first step is to parameterize the pyrolysis model of pure PBT. The sample thickness and T_{back} data of pure PBT at both 30 kW m^{-2} and 60 kW m^{-2} were inversely analyzed to determine the thermal transport properties of PBT-based condensed-phase components participating in Reactions (1-3) in Table 6.1. The resulting thermal transport properties were validated against the corresponding MLR data that were not used in the parameterization process. In the second step, the thermal transport properties of GF were estimated using the sample thickness and T_{back} data of PBT/GF25 at 30 kW m^{-2} and 60 kW m^{-2}. The parameterization process in the second step relied on the thermal transport properties of PBT determined in the first step. Initially, GF was modeled as a single component throughout the test. However, it is impossible to capture the temperature profiles at both heat fluxes by treating GF in such a simple manner. It is expected that when PBT melts and decomposes, the interface between PBT-based components and GF changes. Therefore, GF was assumed to evolve (GF→GF_Melt, GF_Mel→GF_Res1, GF_Res1→GF_Res2) identically to PBT decomposition (Reactions (1- 3) in Table 6.1). The same Arrhenius parameters as Reactions (1-3) in Table 6.1 were assigned to GF evolution; no mass loss and no heat of reactions were assigned. It should be noted that the incorporation of these reactions does not mean that GF is chemically reactive. The main purpose is to enable a flexible characterization of the effective physical interaction between PBT and GF during the

pyrolysis process. The GF in the PA66/GF25 system was treated in the same manner. The thermal transport properties of evolved GF-based components were determined and validated in a similar manner as the first step.

In the third step, the thermal transport parameters of DEPAL-based components participating in Reactions (4-5) in Table 6.1 were determined through the inverse analysis of sample thickness and T_{back} data of PBT/GF25-DEPAL16 (a higher DEPAL concentration blend) at 30 kW m^{-2} and 60 kW m^{-2}. The resulting properties were validated against the T_{back} data of a lower DEPAL concentration blend, PBT/GF25-DEPAL8, as well as the MLR data of both DEPAL-containing blends at both heat fluxes. In the fourth step, similar to the DEPAL-containing blends, the thermal transport parameters of MPP-based components participating in Reactions (6-8) in Table 6.1 were determined and validated through the inverse analysis of experimental measurements of two MPP-containing blends. In the final step, the extrapolating capability of the resulting model based on all the parameters determined in previous steps was examined through predicting experimental measurements obtained for two additional blends with new compositions, PBT/GF25-DEPAL8-MPP4 and PBT/GF25-DEPAL16-MPP8. In addition, simulations of an idealized cone calorimeter experiment were conducted to understand the impact of two additives, DEPAL and MPP, on HRR data of a burning material and thus evaluate it role in the fire performance of PBT/GF/DEPAL/MPP blends.

6.2.2 Pyrolysis Model Development for Pure PBT

The melting and decomposition processes of PBT are characterized by Reactions

(1-3) in Table 6.1. The pyrolysis model development of PBT requires the knowledge of these reaction parameters and the thermal transport properties (emissivity, absorption coefficient, density, and thermal conductivity) of the condensed-phase components participating in these reactions. The reaction parameters have been obtained in Section 6.1.2 and summarized in Tables 6.1-6.3. The optical properties (emissivity and absorption coefficient) were first parameterized. The emissivity of PBT was assumed to be the same as the average total emissivity of PBT that was calculated from the spectral reflectance measured with the NIST Integrating-sphere device at a source temperature of 1081 K by Linteris et al. [62]. The same emissivity as PBT was assigned to PBT_Melt and PBT_Res1 by assuming the melting process and first decomposition reaction did not affect the emissivity. The emissivity of final residual component, PBT_Res_2, was defined as 0.94. This value was determined experimentally by comparing the measured back surface temperatures of various residue samples with one-half of the residue surface coated with high emissivity paint (0.94) and the other uncoated residue. No difference in the sample back surface temperature was identified between the painted and unpainted halves. Therefore, the emissivity of the residual component was defined to be the same as the paint emissivity, 0.94.

The absorption coefficient of PBT was obtained from the study by Linteris et al. [62]. The absorption coefficient of PBT was determined as 3720 m^{-1} at a thickness where 80% of the energy was absorbed at a source temperature of 1081 K. It is noted that the absorption coefficients provided in the current study were normalized by the corresponding densities. PBT_Melt was assumed to have the same absorption

coefficient as PBT. The final residue was observed to appear very optically dark and graphitic in nature. Therefore, the absorption coefficient of PBT_Res2 was defined as 100 $m^2 kg^{-1}$ to ensure that no significant radiation was allowed to transmit through the residue. The absorption coefficient of intermediate product (PBT_Res1) that described the gradual transformation from PBT_Melt and PBT_Res2 was determined to be equal to the averaged value of PBT_Melt and PBT_Res2. The resulting emissivity and absorption coefficients are provided in Table 6.5.

Subsequently, the densities of condensed-phase components (PBT, PBT_Melt, PBT_Res1, and PBT_Res2) were defined to capture the sample thickness evolution. The density of PBT was measured at room temperature. At 60 kW m^{-2}, the sample thickness decreased to almost zero at the end. The densities of PBT_Melt, PBT_Res1, and PBT_Res2 were defined based on the experimental observation that the sample did not change in thickness until late stages of gasification tests. The resulting densities of these components are provided in Table 6.5.

Table 6.5 A full set of thermal transport properties of each condensed-phase component.

Component	ρ (kg m^{-3})	ε	κ (m^2 kg^{-1})	k (W m^{-1} K^1)
PBT	1333	0.88	2.8	0.12
PBT_Melt	1333	0.88	2.8	0.23
PBT_Res1	1120	0.88	51.4	$0.1+1.2\times10^{-4}$ T
PBT_Res2	1333	0.94	100	0.18
GF	2518	0.81	6.4	0.70
GF_Melt	2518	0.81	6.4	0.03
GF_Res1	2518	0.88	53.2	0.06
GF_Res2	413	0.94	100	0.15

DEPAL	1570	0.88	2.8	0.40
DEPAL_Res1	2566	0.94	100	$1\times10^{-10}\,T^3$
PBT_DEPAL_Res1	1511	0.94	100	$1\times10^{-9}\,T^3$
MPP/MPP*	2188/200	0.88	2.8	0.16
MPP_Res1	2188	0.94	100	0.16
PBT_MPP_Res1	200	0.91	51.4	$1.4\times10^{-4}\,T$
PBT_MPP_Res2	53	0.94	100	$0.1+2.7\times10^{-10}\,T^3$

Figure 6.8 depicts the mean experimental back surface temperatures (black dashed lines) of pure PBT exposed to radiant heat fluxes at both 30 kW m^{-2} and 60 kW m^{-2}. Shaded area corresponds to the maximum and minimum experimental temperatures across the sample surface from the repeated experiments. Both temperature profiles were cropped at the time when 70 wt.% of the sample was decomposed. This was done because the 1D assumption was not valid after a majority of sample was consumed. The residue agglomerated in the center rather than remained as a uniform layer.

The thermal conductivities of these four condensed-phase components were the only remaining undefined parameters in the development of pyrolysis model. Inverse analysis of back surface temperature profiles in Figure 6.8 was conducted to determine these thermal conductivities. The first 150 s of experimental temperature profile at 30 kW m^{-2} in Figure 6.8(a) was inversely modeled to determine the thermal conductivity of PBT component. The initial rise of the T_{back} curve was chosen as the target for the virgin component because PBT was the only component that affected the T_{back} curve early in the test. The thermal conductivities of the intermediate components, PBT_Melt, and PBT_Res1, were defined through the inverse analysis of the T_{back} profile of 150 - 300 s and 300 - 690 s obtained at 30 kW m^{-2}. The data at the lower heat

flux were chosen as the parameterization target because the distinct modeled components are more easily isolated in these data than in the data collected at the higher heat flux. The data of 150 - 230 s at 60 kW m^{-2} in Figure 6.8(b), where the sample was almost fully decomposed, were fitted to determine the thermal conductivity of the final residual component, PBT_Res2. The remaining data at the higher heat flux were used to adjust the initially determined conductivities to capture both temperature profiles. The principle of the inverse analysis process is to keep the simplest parameter set as possible while the agreement between the experimental and modeled curves is within the experimental uncertainties. The resulting thermal conductivities are reported in Table 6.5. The pyrolysis model, that included thermal transport properties determined in this section and the reaction parameters determined in Section 6.1.2, was employed to simulate the temperature profiles obtained at 30 and 60 kW m^{-2}, shown as red solid lines in Figure 6.8.

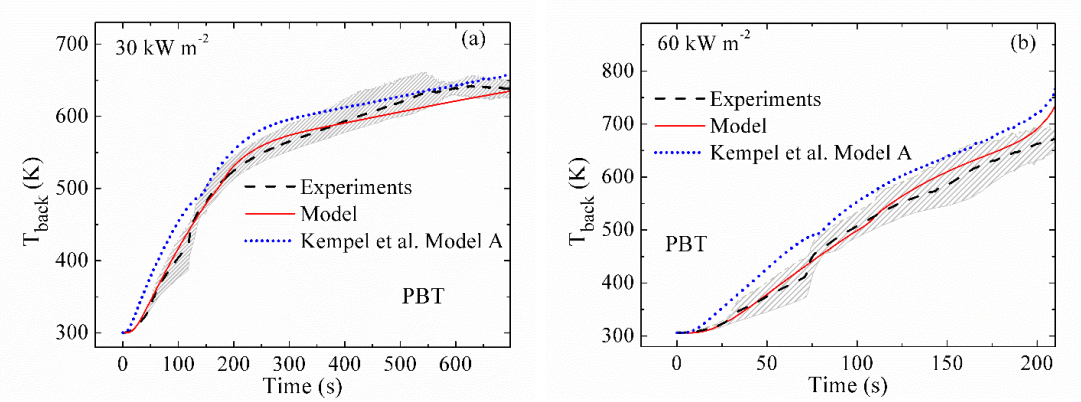

Figure 6.8 Experimental and simulated back surface temperatures of pure PBT exposed to radiant fluxes set at (a) 30 kW m^{-2} and (b) 60 kW m^{-2}. Shaded area corresponds to the maximum and minimum experimental temperatures across the

sample surface from repeated tests. Blue dotted lines represent the modeling results of Model A obtained from the study by Kempel et al. [39].

The developed pyrolysis model of PBT based on the resulting properties in this section was validated against the experimental MLR data of PBT obtained at 30 kW m^{-2} and 60 kW m^{-2}, shown in Figure 6.9. It is worth noting that the MLR data were not utilized in the inverse analysis model calibration. Figure 6.9 shows the mean experimental (symbols) and predicted (red solid lines) MLR data at both heat fluxes. The error bars of MLR data were computed as two standard deviations of the mean. 2 wt.% and 15 wt.% residues remained at the end of the 30 kW m^{-2} and 60 kW m^{-2} tests, respectively. The model predicts the experimental MLR profiles well at both heat fluxes with the exception of an abrupt MLR decrease to zero at the end of the 60 kW m^{-2}. This is likely due to the invalid 1D assumption at the end of the experiment when the residue agglomerated in the center instead of spreading out as a uniform layer.

The predictions of temperature and MLR data of pure PBT using a pyrolysis Model A developed by Kempel et al. [39] are also included as blue dotted lines in Figures 6.8 and 6.9. This model captures the initial rise of MLR curves at both heat fluxes very well. However, this model consistently over-predicts the T_{back} data and MLR peaks at both heat fluxes. The materials from different manufacturers used in these two studies may contribute to the overestimation.

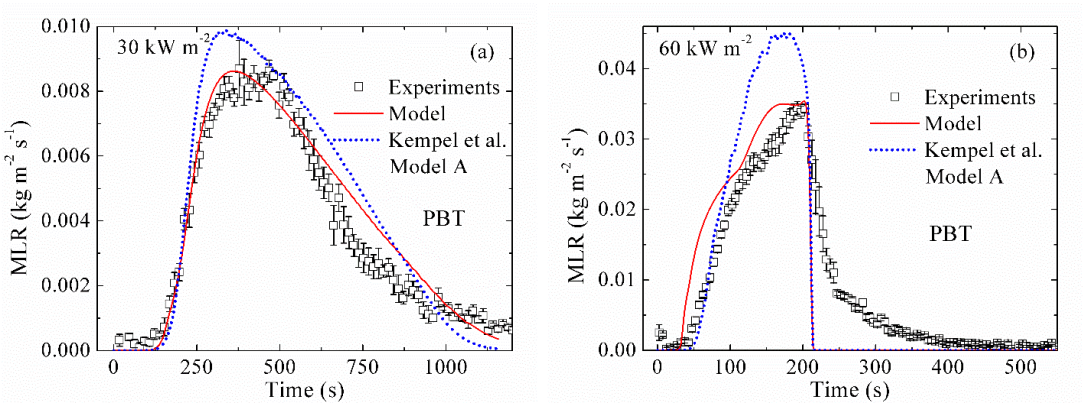

Figure 6.9 Experimental and predicted MLR data of pure PBT exposed to radiant fluxes set at (a) 30 kW m^{-2} and (b) 60 kW m^{-2}. Blue dotted lines represent the modeling results of Model A obtained from the study by Kempel et al. [39].

6.2.3 Pyrolysis Model Development for PBT/GF25

In the model parameterization of PBT/GF25, the resulting material properties of pure PBT in Section 6.2.2 remained identical and the additional properties of GF were determined. As discussed in Section 6.2.1, GF was assumed to evolve (GF→GF_Melt, GF_Mel→GF_Res1, GF_Res1→GF_Res2) in the same manner as PBT to account for the changes in the thermal transport interaction between PBT and GF during the PBT decomposition. Therefore, the thermal transport properties of GF-based components were estimated to capture the experimental measurements of PBT/GF25.

The emissivity and absorption coefficient of PBT/GF25 were obtained from a study by Linteris et al. [62]. The emissivity and absorption coefficient of GF were calculated by subtracting the values of PBT from the values of PBT/GF25 based on their volume- and mass-weighted contributions, respectively. The emissivity and absorption coefficient of GF_Melt were assumed to be the same as those of virgin

component, GF. The emissivity and absorption coefficient of final residue, GF_Res2, were defined as 0.94 and 100 $m^2 kg^{-1}$ in the same manner as the final residue of PBT decomposition, PBT_Res2. The emissivity and absorption coefficient of GF_Res1 were assumed to be the averaged values of GF_Melt and GF_Res_2. The density of PBT/GF25 was measured at room temperature. The density of GF was determined based on the known densities of PBT and PBT/GF25, and mass composition of PBT/GF25. The densities of the GF_Melt, GF_Res1, and GF_Res2 were determined to capture the approximately constant sample thickness. The resulting parameters are summarized in Table 6.5.

Figure 6.10 shows the mean experimental back surface temperatures (black dashed lines) of PBT/GF25 at 30 kW m^{-2} and 60 kW m^{-2}. When the GF (chemically inert) was added into PBT, the T_{back} data were significantly reduced compare to those of PBT. The thermal conductivities of GF-based components were determined through inversely modeling the temperature profiles in Figure 6.10. The initial rise of the temperature data of 0 - 200 s at 30 kW m^{-2} in Figure 6.10(a) were used to determine the thermal conductivity of GF. The temperature data of 200 - 400 s and after 400 s at 30 kW m^{-2} in Figure 6.10 (a) were employed to determine the thermal conductivities of GF_Melt and GF_Res1, respectively. The temperature data of 500 - 700 s at 60 kW m^{-2} in Figure 6.10 (b) were employed to determine the thermal conductivity of GF_Res2 since GF_Res2 is the dominant component. The resulting thermal conductivity values were adjusted to capture the temperature data at both heat fluxes in Figure 6.10. These slightly over-predicted temperature data of 250 - 450 s at 60 kW m^{-2} can be either due to the imperfections of the model (associated with a relative

simplicity of its formulation) or due to small systematic errors in the experimental measurements.

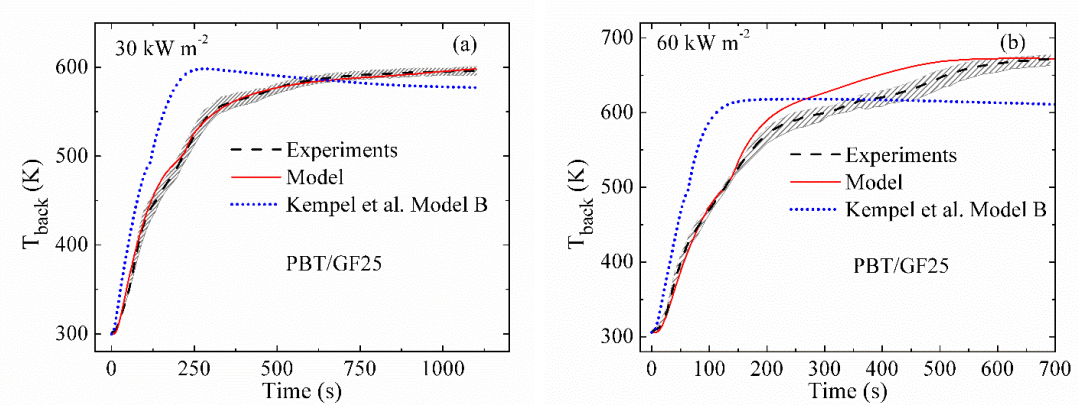

Figure 6.10 Experimental and simulated back surface temperatures of PBT/GF25 exposed to radiant fluxes set at (a) 30 kW m^{-2} and (b) 60 kW m^{-2}. Shaded area corresponds to the maximum and minimum experimental temperatures across the sample surface from repeated tests. Blue dotted lines represent the modeling results of Model B obtained from the study by Kempel et al. [39].

The developed pyrolysis model of PBT/GF25 was validated against the experimental MLR data obtained at 30 kW m^{-2} and 60 kW m^{-2}, shown in Figure 6.11. It is worth noting that the MLR data were not utilized in the inverse analysis model calibration. Figure 6.11 shows the experimental (symbols) and predicted (green dashed lines) MLR data at both heat fluxes. The magnitudes of MLR peaks were underestimated by 30% and 50% at 30 kW m^{-2} and 60 kW m^{-2}, respectively. A similar underestimation of the MLR peaks was observed in PA66-based system, shown in Figure 5.9 of Section 5.2.3. An additional analysis was also conducted to understand the cause of this poor agreement. First, the T_{back} and MLR profiles of pure PBT in Figures 6.8 and 6.9 were well captured, which indicated the accuracy of the resulting

reaction parameters and thermal transport parameters of pure PBT. It is noted that the same reaction parameters were used for PBT and PBT/GF since the GF is chemically inert. In addition, the well-captured temperature profiles of PBT/GF25 in Figure 6.10 indicated the accuracy of the resulting thermal transport parameters of GF-based components. Therefore, the underestimated MLR data of PBT/GF25 in Figure 6.11 demonstrated that additional mass transport features should be taken into account.

According to the literature information, the wick effect was observed in the glass fiber reinforced polymers [96,97,103]. Due to the wick effect of glass fiber, the molten polymer is transported from regions of higher concentration to regions of lower concentration. It was found that the incorporation of wick effect helped to improve the MLR predictions of PA66/GF25, shown in Figure 5.9 of Section 5.2.3. Therefore, the neglected wick effect of glass fiber is also a possible explanation for the underestimated MLR data.

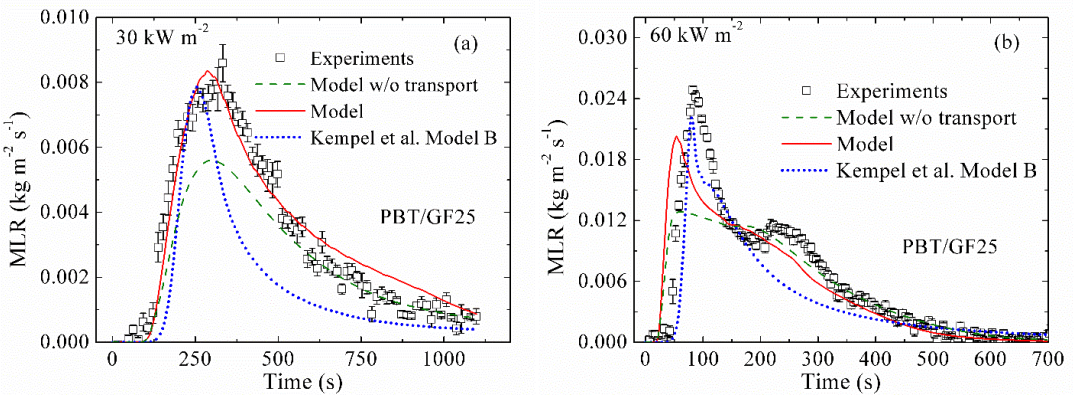

Figure 6.11 Experimental and predicted MLR data of PBT/GF25 exposed to radiant fluxes set at (a) 30 kW m^{-2} and (b) 60 kW m^{-2}. Blue dotted lines represent the modeling results of Model B obtained from the study by Kempel et al. [39].

The existence of wick effect (transport behavior) in PBT/GF25 was confirmed

through experimental measurements. If the wick effect exists during the gasification test of PBT/GF25, the molten PBT will migrate from the bottom layer to the top layer where the concentration of molten PBT is lower due to an earlier decomposition of PBT. Therefore, the concentration of the final residual component, PBT_Res2, in the top layer of PBT/GF25 residue obtained from CAPA II test at 60 kW m^{-2} (fully decomposed) is expected to be higher than that of the fully decomposed virgin sample without transport. Therefore, their concentration of PBT_Res2 were examined to confirm the existence of the transport behavior. Figure 6.12 details the three-step confirmation process. The first step is to obtain Sample A from the virgin PBT/GF25 granules or plates, and Sample B from the top layer (about 1×10^{-3} m) of PBT/GF25 residue (3.8×10^{-3} m) after the CAPA II test at 60 kW m^{-2}. The second step is to heat both Sample A and Sample B (4-7 mg) up to 600 ℃ in N_2 at a nominal heating rate of 10 K min^{-1} in TGA tests. The small sample mass and low heating rate allowed us to assume that the sample was thermally thin (no significant concentration and temperature gradient inside the sample). The second step was done to ensure that PBT in both samples were fully decomposed into the final residual component, PBT_Res2. The third step is to re-heat the sample residues obtained from the second step up to 600 ℃ in air at a prescribed heating rate of 10 K min^{-1} in TGA tests. The change in the mass of the samples observed in the air experiments was indicative of how much of the final residual component, PBT_Res2, each sample contained (unlike the glass fiber, PBT_Res2 fully oxidizes and volatilizes when heated in the presence of oxygen). The fact that the mass loss for the Sample B in the third step is larger than that for the Sample A indicates that the molten polymer migrates to the top layer during the

pyrolysis process and confirms the existence of wick effect during the gasification test of PBT/GF25.

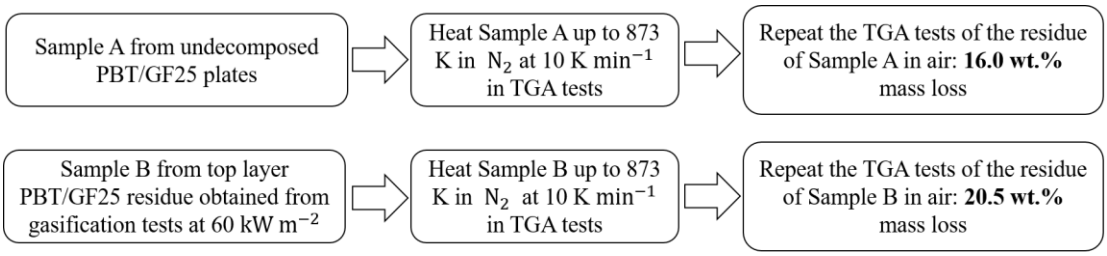

Figure 6.12 Three-step confirmation process of the existence of wick effect

Therefore, the transport behavior of molten polymer was included and characterized using a single mass transport coefficient in the current pyrolysis model. The value of the transport coefficient was determined to be 9.5×10^{-9} m^2s^{-1} through inversely modeling the MLR data of PBT/GF25 obtained at 30 kW m^{-2}. This value was smaller than that of transported components in PA66-based system, which is partially due to a slightly lower viscosity number of PA66 [137,138]. In this new molten polymer transport model, all the material properties remain identical as the previous model (without transport). Subsequently, the new transport model was validated against the MLR data of PBT/GF25 obtained at 60 kW m^{-2}. The simulated MLR profiles at both heat fluxes using the new transport model are shown as the red solid lines in Figure 6.11. The new transport model captures the MLR profile at 30 kW m^{-2} very well, with an improvement of 30% in the magnitude of MLR peak. The prediction of the magnitude of MLR peak at 60 kW m^{-2} was improved by 30%. However, the temperature and magnitude of MLR peak at 60 kW m^{-2} were still underestimated, which was likely due to fact that the transport behavior may also depend on the temperature gradient inside the sample and thus cannot be fully characterized by a

single transport coefficient. However, no further complexity of the transport behavior was included to avoid further complicating the model because when a small amount of flame retardant additives was added, the increased dependence of transport behavior on the higher external heat flux was less notable. The evidence of the less notable dependence is provided in Sections 6.2.4 and 6.2.5.

The new transport model was also employed to simulate the back surface temperature profiles of PBT/GF25 at both heat fluxes. No significant difference was identified between the simulated results calculated by the model with transport and the model without transport. Therefore, the red solid lines in Figure 6.10 represent the simulated T_{back} profiles for both models.

The predictions of T_{back} and MLR data using a pyrolysis Model B developed by Kempel et al. [39] are also included as blue dotted lines in Figures 6.10 and 6.11. This model initially over-predicts and then under-predicts the T_{back} data at both 30 kW m^{-2} and 60 kW m^{-2}. This model captures the magnitudes of the MLR peaks although it significantly underestimates the decaying portion of MLR curves at both heat fluxes. The materials from different manufacturers used in these two studies may contribute to the unsatisfactory agreement. In addition, the neglected molten polymer transport behavior in the model developed by Kempel et al. may also explain the poor agreement. It should be emphasized that the pyrolysis model of PBT/GF25 developed in this work can be used to capture the pyrolysis behavior for both pure PBT and PBT/GF25. However, Model A and Model B obtained from the study by Kempel et al. were developed for pure PBT and PBT/GF25 individually and consisted of completely independent property sets.

6.2.4 Pyrolysis Model Development for PBT/GF/DEPAL Blends

During the parameterization process of pyrolyzing PBT/GF/DEPAL blends, all the properties of PBT-based and GF-based components determined in the previous sections were adopted and the additional properties of DEPAL-based components participating in Reactions (4-5) in Table 6.1 were obtained. It was assumed that DEPAL component had the same transport rate as the molten polymer, PBT_Melt. The emissivity and absorption coefficient of DEPAL were assumed to be the same as those of PBT due to a small amount of DEPAL in the blend. The emissivity and absorption coefficient of final residual components, DEPAL_Res1 and PBT_DEPAL_Res1, were also defined as 0.94 and 100 $m^2 kg^{-1}$ in the same manner as the residual component, PBT_Res2. The density of PBT/GF25-DEPAL16 was measured at the room temperature. The density of DEPAL was calculated based on the known densities of PBT, GF, and PBT/GF25-DEPAL16, and mass composition of PBT/GF25-DEPAL16. DEPAL partly vaporizes and partly decomposes to a diethyl phosphinic acid vapor and an aluminum phosphate residue in the condensed-phase [91]. Therefore, DEPAL_Res1 was assumed to have the same density as aluminum phosphate [139]. The density of PBT_DEPAL_Res1 was estimated to capture the approximately constant sample thickness throughout the test. The resulting parameters are summarized in Table 6.5.

Figure 6.13 shows the mean experimental T_{back} profiles (black dashed lines) of PBT/GF25-DEPAL16 at both heat fluxes. The initial rise of the back surface temperature data of 0 - 200 s at 30 kW m^{-2} was employed to determine the thermal conductivity of DEPAL. The back surface temperature data after 300 s at 30 kW m^{-2} were used to determine the thermal conductivity of PBT_DEPAL_Res1. The

temperature data of 450 - 650 s at 60 kW m^{-2} were used to determine the thermal conductivity of DEPAL_Res1 since it was produced at a relatively high temperature. Due to the high porosity and temperature of the residue, radiation was assumed to be the dominant mode of heat transfer inside the residue. The radiation diffusion approximation [130] was used to describe the thermal conductivity of the residual components, DEPAL_Res1 and PBT_DEPAL_Res1, with a third-power temperature dependence. The resulting conductivities were adjusted in order to fit both temperature profiles within the experimental uncertainties on average. The simulated results are shown as the red solid lines in Figure 6.13.

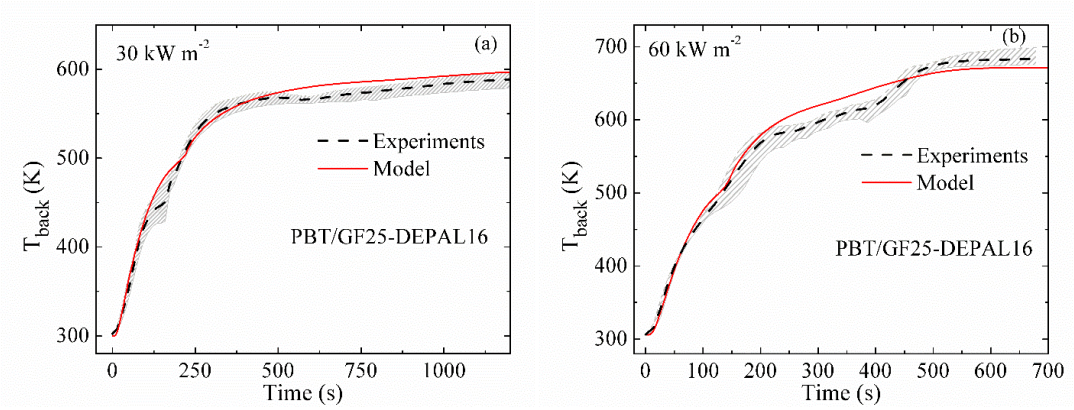

Figure 6.13 Experimental and simulated back surface temperatures of PBT/GF25-DEPAL16 exposed to radiant fluxes set at (a) 30 kW m^{-2} and (b) 60 kW m^{-2}. Shaded area corresponds to the maximum and minimum experimental temperatures across the sample surface from repeated tests.

The material properties determined in this section were first validated against the T_{back} data obtained for a lower DEPAL concentration blend, PBT/GF25-DEPAL8. Figure 6.14 shows the experimental and simulated temperature profiles of PBT/GF25-DEPAL8 at both heat fluxes. The model captures the temperature profiles pretty well

except for an overestimation of the data at the end of the 30 kW m^{-2} test and of the data between 250 - 450 s at 60 kW m^{-2} in Figure 6.14(b). The presence of these minor discrepancies can be either due to the imperfections of the model (associated with a relative simplicity of its formulation) or due to small systematic errors in the experimental measurements.

Subsequently, the MLR data of both DEPAL-containing blends obtained at 30 and 60 kW m^{-2}, not utilized in the inverse analysis model calibration, were used to further validate the resulting properties. Figure 6.15 shows the mean experimental and predicted MLR data of PBT/GF25-DEPAL8 and PBT/GF25-DEPAL16 at 30 and 60 kW m^{-2}. When DEPAL was added, the experimental MLR peaks were reduced compared to those of PBT/GF25. Additionally, as more DEPAL was added, a greater reduction in the MLR peaks was obtained. The model captures the MLR profiles at 30 kW m^{-2} very well. Despite an underestimation of the decaying of the MLR profiles at the higher heat flux, the corresponding magnitudes of the MLR peaks are predicted very well. The improved prediction of MLR profiles indicates that, as was already discussed in Section 6.2.3, the addition of the flame retardant reduces the impact of the wick effect at high heating intensity.

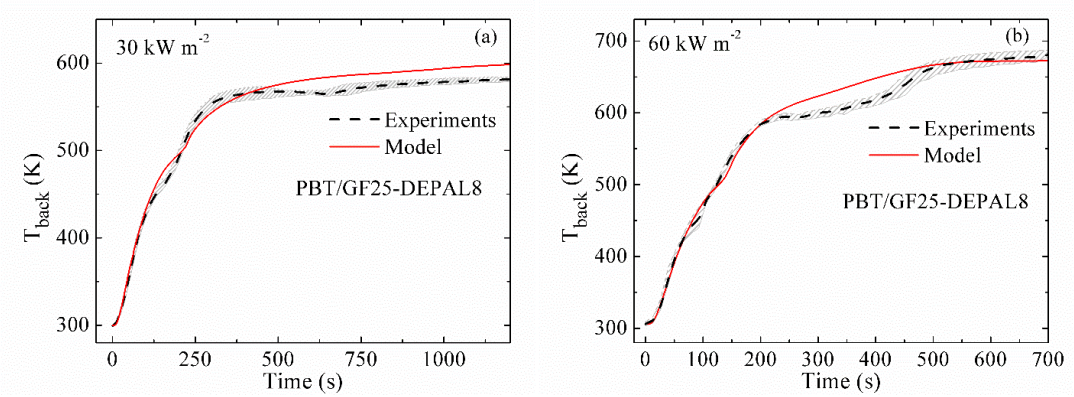

Figure 6.14 Experimental and predicted back surface temperatures of PBT/GF25-DEPAL8 exposed to radiant fluxes set at (a) 30 kW m^{-2} and (b) 60 kW m^{-2}. Shaded area corresponds to the maximum and minimum experimental temperatures across the sample surface from repeated tests.

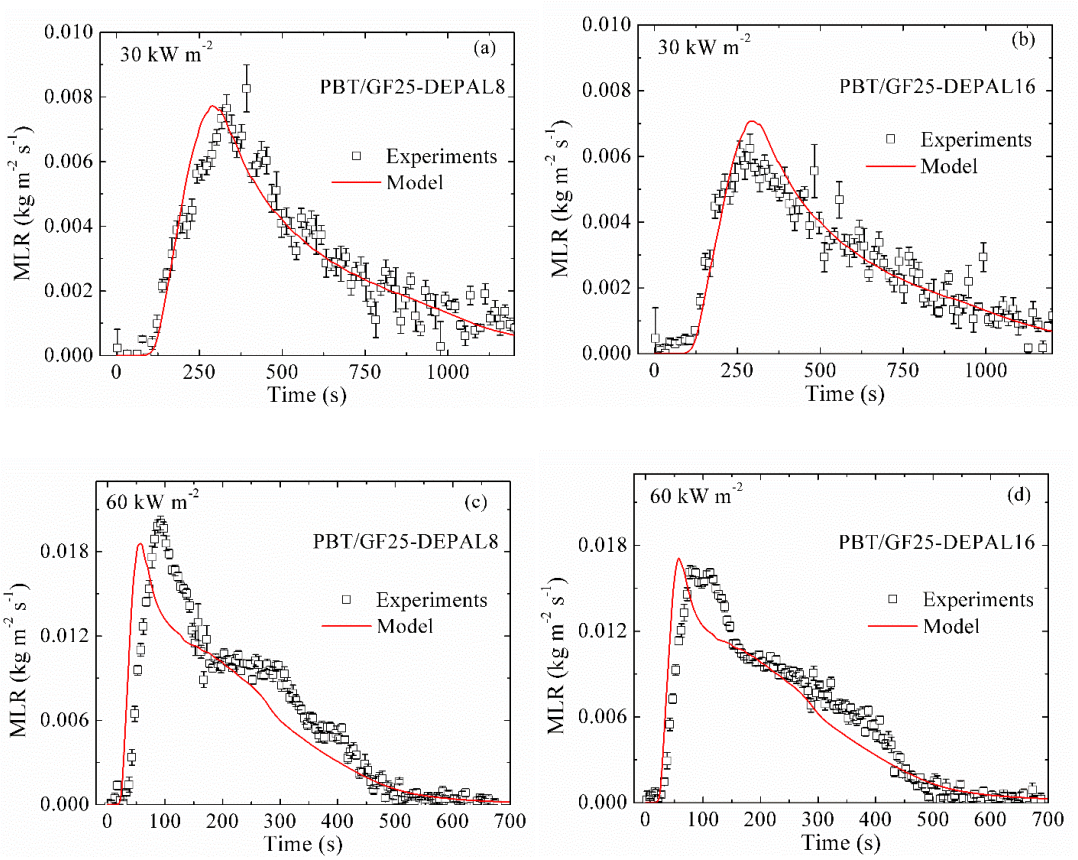

Figure 6.15 Experimental and predicted MLR data of (a) (c) PBT/GF25-DEPAL8 and (b) (d) PBT/GF25-DEPAL16 exposed to radiant fluxes set at 30 and 60 kW m^{-2}.

6.2.5 Pyrolysis Model Development for PBT/GF/MPP Blends

During the parameterization process of pyrolyzing PBT/GF/MPP blends, all the properties determined in the previous sections were adopted and the additional properties of MPP-based components participating in Reactions (6-8) in Table 6.1 were

obtained. It was assumed that MPP had the same transport rate as the molten polymer, PBT_Melt. The emissivity and absorption coefficient of MPP component were assumed to be the same as those of PBT due to a small amount of MPP in the blend. The emissivity and absorption coefficient of residual components, MPP_Res1 and PBT_MPP_Res2, were also defined as 0.94 and 100 $m^2 kg^{-1}$ in the same manner as PBT_Res2. The emissivity and absorption coefficient of the intermediate product, PBT_MPP_Res1, were assumed to be the averaged values of PBT_Melt and PBT_MPP_Res2.

The density of PBT/GF25-MPP8 was measured at the room temperature. The density of MPP was calculated based on the known densities of PBT, GF, and PBT/GF25-MPP8, and the mass composition of PBT/GF25-MPP8. In order to simulate the sample thickness, an additional component MPP* that has the same properties as MPP, except for a lower density, was introduced in the model. MPP changed into MPP* when its temperature reached 430 K. The value of the transition temperature was determined through fitting the measured experimental sample thickness evolution. MPP_Res1 was assumed to have the same density as MPP due to a very small amount of MPP_Res1 remaining in the residue. The resulting parameters are summarized in Table 6.5.

Figure 6.16 shows the mean experimental back surface temperature profiles (black dashed lines) of PBT/GF25-MPP8 at both heat fluxes. With the incorporation of MPP, the T_{back} at 1100 s of 30 kW m^{-2} was reduced by 40 K and the T_{back} at 700 s of 60 kW m^{-2} was reduced by 65 K compared to those of PBT/GF25 in Figure 6.12. The initial rise of the temperature data of 0 - 250 s at 30 kW m^{-2} was fitted to determine the

thermal conductivity of MPP. The thermal conductivity of MPP_Res1 was assumed to be the same as MPP due to a very small amount of MPP_Res1 produced in the condensed-phase. The temperature data of 300 - 600 s and 600 - 1200 s at 60 kW m^{-2} were used to determine the thermal conductivities of PBT_MPP_Res1 and PBT_MPP_Res2, respectively. The thermal conductivities were adjusted in order to fit both temperature profiles. The resulting parameters are summarized in Table 6.5. The simulated results are shown as the red solid lines in Figure 6.16. The model captures the profiles very well except for a slight underestimation of temperature data at the end of the 30 kW m^{-2} test.

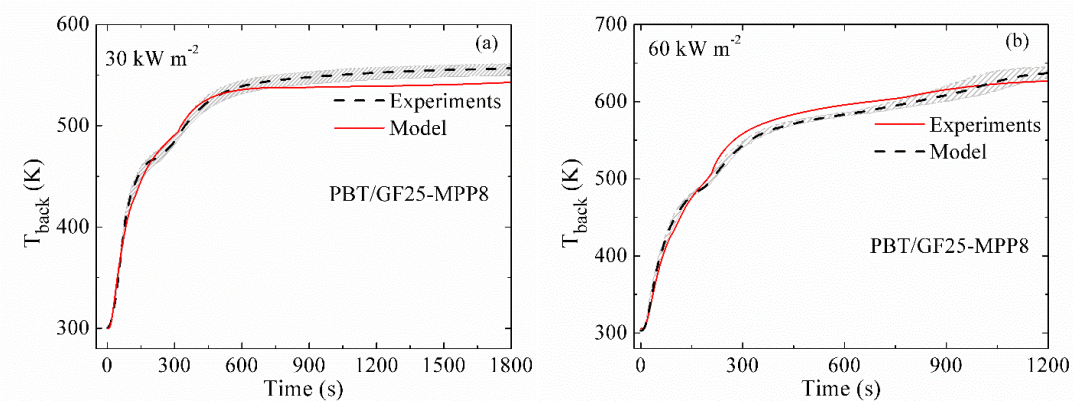

Figure 6.16 Experimental and simulated back surface temperatures of PBT/GF25-MPP8 exposed to radiant fluxes set at (a) 30 kW m^{-2} and (b) 60 kW m^{-2}. Shaded area corresponds to the maximum and minimum experimental temperatures across the sample surface from repeated tests.

The material properties determined in this section were first validated against the T_{back} data obtained for a lower MPP concentration blend, PBT/GF25-MPP4. Figure 6.17 shows the experimental and predicted temperature profiles of PBT/GF25-MPP4 at both heat fluxes. The model captures the T_{back} profiles well except for an

underestimation at the end of the 30 kW m^{-2} test. The presence of these minor discrepancies can be either due to the imperfections of the model (associated with a relative simplicity of its formulation) or due to small systematic errors in the experimental measurements.

Subsequently, the MLR data of both MPP-containing blends obtained at 30 and 60 kW m^{-2} were used to further validate the resulting properties. Figure 6.18 shows the mean experimental and predicted MLR data of PBT/GF25-MPP4 and PBT/GF25-MPP8 at 30 and 60 kW m^{-2}. The experimental MLR peaks of both blends were reduced significantly compared to PBT/GF25 wherein MPP was not present. At 30 kW m^{-2}, the MLR peaks were reduced by 40% and at 60 kW m^{-2}, the MLR peaks were reduced by 50%. No significant MLR profile changes were identified with MPP composition changing from 8 wt.% to 4 wt.%. The model captures the MLR data very well. The good prediction of the high heat flux MLR profiles indicates that, as mentioned in Section 6.2.3, the incorporation of MPP reduces the impact of the wick effect at this high heating intensity and thus brings the modeling results into nearly perfect agreement with the experimental results.

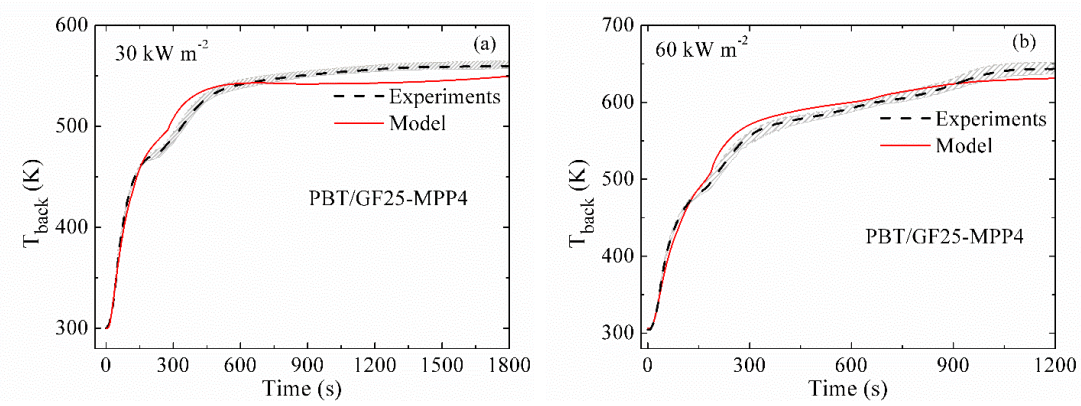

Figure 6.17 Experimental and predicted back surface temperatures of PBT/GF25-MPP4 exposed to radiant fluxes set at (a) 30 kW m^{-2} and (b) 60 kW m^{-2}. Shaded area corresponds to the maximum and minimum experimental temperatures across the sample surface from repeated tests.

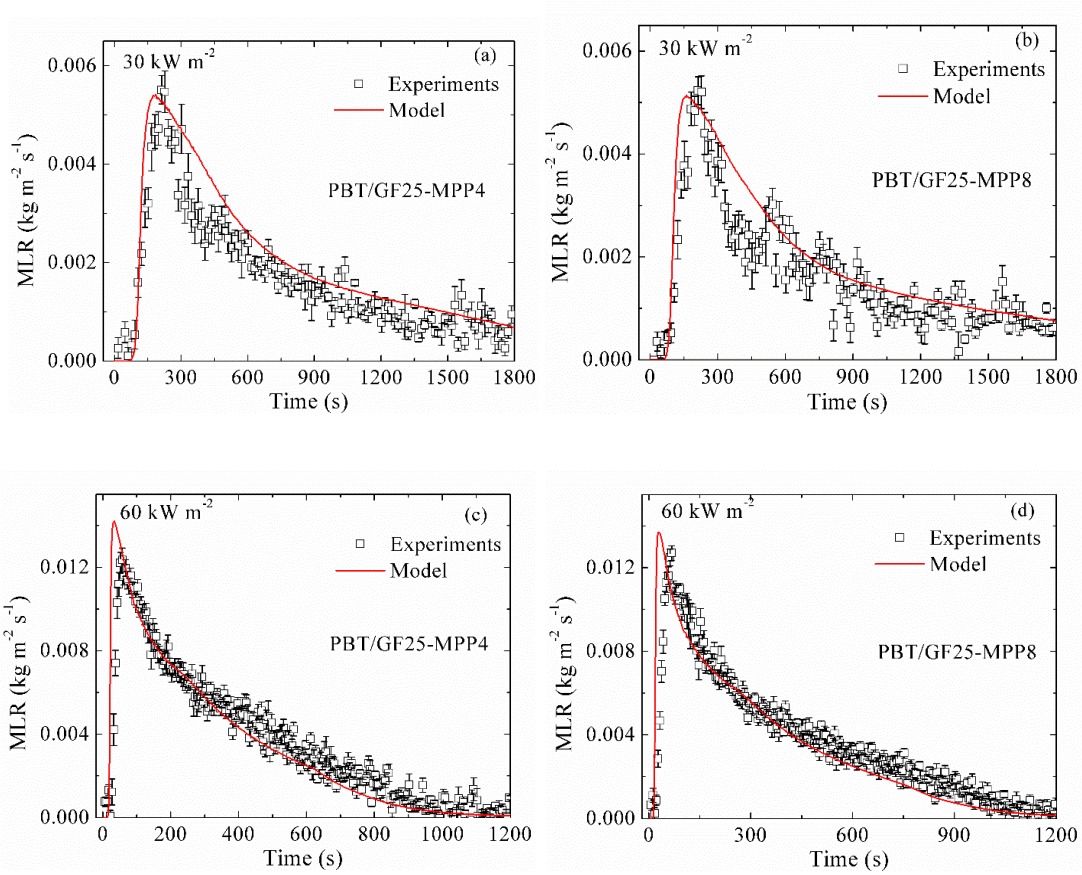

Figure 6.18 Experimental and predicted MLR data of (a) (c) PBT/GF25-MPP4 and (b) (d) PBT/GF25-MPP8 exposed to radiant fluxes set at 30 kW m^{-2} and 60 kW m^{-2}.

6.2.6 Extrapolation to New Compositions

The previous sections demonstrated that the developed pyrolysis model captured the T_{back} and MLR data of all six calibrated PBT/GF/DEPAL/MPP blends for any thermal exposure. In this section, the extrapolating capability of the pyrolysis model

was validated against the experimental data obtained for two blends with new compositions, PBT/GF25-DEPAL8-MPP4 and PBT/GF25-DEPAL16-MPP8. The gasification experiments of the two blends were conducted at a nominal radiant heat flux of 45 kW m^{-2} that lies in between the two calibrated heat fluxes.

Figure 6.19 shows the mean experimental and predicted back surface temperature and MLR data of the two blends at 45 kW m^{-2}. It should be noted that these experimental measurements were not employed in the model parameterization process. The magnitude of experimental MLR peak of PBT/GF25-DEPAL16-MPP8 is slightly reduced compared to that of PBT/GF25-DEPAL8-MPP4. The model predicts the experimental data well except for the underestimated temperature data (after 180 s) of PBT/GF25-DEPAL16-MPP8. It is noted that the current model did not include the potential synergetic effect between DEPAL and MPP on the thermal transport process in condensed-phase. However, the model provides reasonable predictions considering the complexity of the pyrolysis model and the blends, which indicates that the synergetic effect on thermal transport process is not significant.

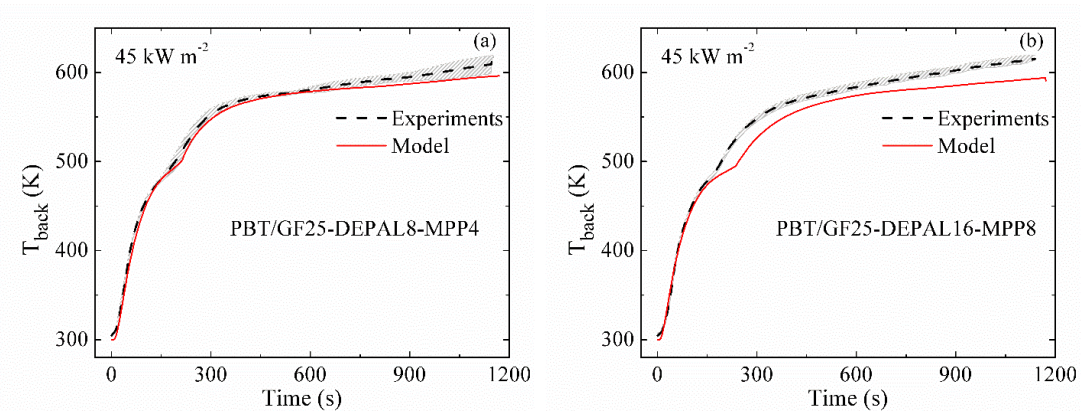

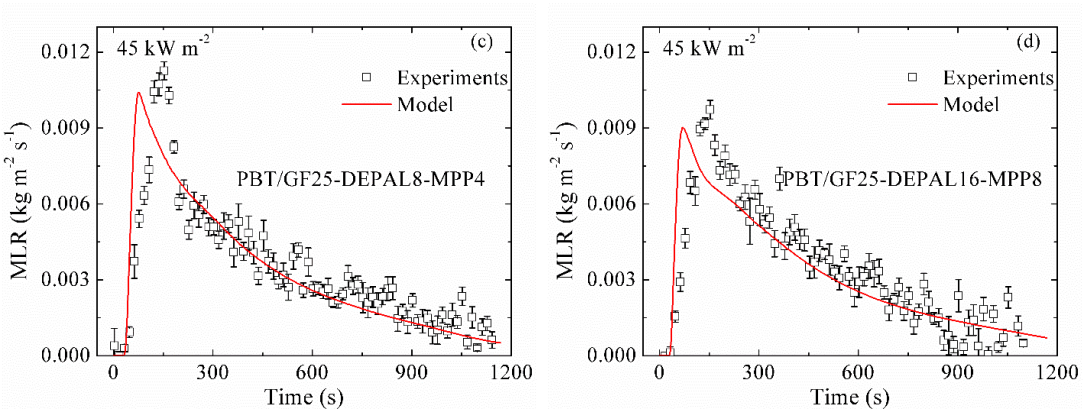

Figure 6.19 Experimental and predicted T_{back} and MLR data of (a) (c) PBT/GF25-DEPAL8-MPP4 and (b) (d) PBT/GF25-DEPAL16-MPP8 exposed to radiant fluxes set at 45 kW m^{-2}.

6.2.7 Impact of Flame Retardant Additives on HRR of Burning Blends

Additional simulations were conducted to understand the impact of the flame retardant additives on the fire performance of the blends. HRR is a critical parameter to assess the fire hazard of a material. Therefore, a simple 1D simulation that mimics the cone calorimeter experiment was conducted. In the simulation, a 4×10^{-3} m thick sample was subjected to an external radiant heat flux of 50 kW m^{-2} incident to the top sample surface. This heat flux represents the heat flux corresponding to surface heating from small laminar flames [131] up to fully involved room fires [132]. The heat flux was constant throughout the entire simulation. The convective heat losses from the top sample surface were neglected and the bottom sample surface employed adiabatic boundary conditions. The simulation neglected the potential impact of sample surface oxidation prior to ignition. Moreover, the additional heat flux provided by the flame that forms on the top sample surface upon ignition was also ignored in the simulation.

A simple and idealistic scenario was simulated to eliminate the effect of imperfection of experimental setup on evaluating the fire behavior of a material. The calculations were terminated when no additional mass loss was observed. The rates of gaseous fuel production or MLR, of the burning sample were computed by ThermaKin2Ds using the developed pyrolysis model. The product of the resulting MLR and the complete heats of combustion of gaseous products obtained in MCC [111], summarized in Table 6.4, yielded the HRR of the burning sample.

The simulated HRR profiles for PBT/GF25, PBT/GF25-DEPAL8, PBT/GF25-DEPAL16, PBT/GF25, PBT/GF25-MPP4, and PBT/GF25-MPP8 exposed to radiant flux set at 50 kW m^{-2} are shown in Figure 6.20. Figure 6.20(a) shows that the incorporation of DEPAL into the sample does not reduce the HRR significantly. Similar action of DEPAL on the MLR curves was observed. It should be noted that the pyrolysis model developed in this work underestimates the magnitude of the experimental MLR peak of PBT/GF25 at a higher heat flux approximately by 20%, shown in Figure 6.11(b). The underestimation likely weakened the impact of DEPAL on the reduction in HRR. A parameter sensitivity analysis demonstrates that the reduction in HRR is mainly due to the impact of DEPAL on the kinetic parameters of the condensed-phase decomposition. The current model has already accounted for all the effects of the additive, DEPAL, on the condensed-phase pyrolysis process. However, the role of DEPAL in reducing the efficiency of gas-phase combustion [92,140] was not considered as the heats of combustion were obtained from MCC wherein all volatiles were forced to complete combustion. Additional work accounting

for the flame inhibition impact of DEPAL on HRR is required to completely assess its role in improving a material's fire performance.

Figure 6.20(b) demonstrates that when MPP is added into the blend, the magnitudes of HRR curves are significantly reduced by about 20% compared to that of PBT/GF25, especially when considering the underestimated magnitude of the MLR peak of PBT/GF25 in Figure 6.11(b). The effect of MPP appears to level off after addition of just 4 wt.%; i.e., further addition of MPP does not significantly reduce the HRR. A sensitivity analysis performed on the model parameters indicates that the thermal transport properties of MPP-based components are primarily responsible for the observed reduction in the HRR. In other words, MPP chemically reacts with PBT and produces condensed-phase products that act as a thermal barrier. The additional MPP component does not further contribute to the reduction of HRR because 4 wt.% MPP is sufficient to interact with PBT-based components. The excess amount of MPP component decomposes by itself, which does not affect the thermal transport significantly and thus no addition reduction in HRR was achieved. Previous work [91,92] also found that MPP acts in the condensed-phase through the formation of a thermal barrier that inhibits the thermal transport underneath.

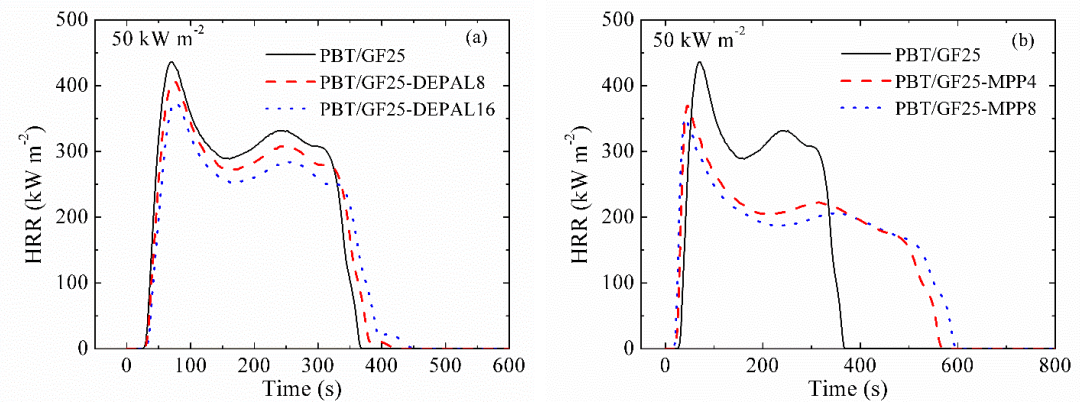

Figure 6.20 Simulated area-normalized HRR data of (a) PBT/GF25, PBT/GF25-DEPAL8, PBT/GF25-DEPAL16 (b) PBT/GF25, PBT/GF25-MPP4, PBT/GF25-MPP8 thermal decomposition exposed to radiant fluxes set at 50 kW m^{-2}.

6.3 Summary

Chapter 6.1 outlined a methodology to develop a quantitative reaction model for a GF-reinforced PBT blended with multiple condensed-phase-active flame retardants, DEPAL and MPP. This methodology was based on TGA, DSC, and MCC experiments that were analyzed using inverse numerical modeling. The developed model was shown to simultaneously reproduce all measurement results for mixtures containing a full range of relevant flame retardant concentrations with a high degree of accuracy. While this model was based on a lumped species approach (and thus did not explicitly resolve individual chemical species), it did capture all essential aspects of the thermal decomposition behavior relevant to the flammability of studies materials. Moreover, through the presented analysis key binary interactions between the material constituents were identified and implemented in the model using second-order (two-component) reactions.

Chapter 6.2 detailed an approach to develop a pyrolysis model for PBT/GF/DEPAL/MPP based on the reaction model constructed in Chapter 6.1. The decomposition kinetics and thermodynamics obtained from Chapter 6.1 served as a core subset of the pyrolysis model inputs. These model inputs were combined with simultaneous measurements of MLR, T_{back}, and sample surface profiles provided by a

newly developed gasification apparatus, to determine the properties that define heat and mass transport in the pyrolyzing blends.

The bench-scale gasification test results demonstrated that the MLR peaks of MPP-containing blends exposed to radiant heat fluxes of 30 kW m^{-2} and 60 kW m^{-2} were reduced by about 40% and 50%, respectively, compared to those of PBT/GF25 wherein MPP was not present. No significant MLR profile changes were identified with MPP content changing from 4 wt.% to 8 wt.%. Smaller reductions of experimental MLR peaks were found in DEPAL-containing blends compared to those of PBT/GF25. Additionally, as more DEPAL was added, a greater reduction in the MLR peak was observed.

During the model development, it was revealed that the wick effect associated with the presence of the glass fiber resulted in the transport of molten polymer from regions of higher concentration to regions of lower concentration. Incorporation of the wick effect into the pyrolysis model significantly improved the accuracy of the PBT/GF25 MLR data prediction. The model was subsequently extended to MPP- and DEPAL-containing blends. In addition, the model was shown to accurately predict the MLR data of two additional blends containing both flame retardant additives, which indicated that the condensed-phase interactions between these two additives were insignificant. The error between all experimental and predicted MLR data was calculated as approximately 15%, on average.

Chapter 6.2 provides a quantification of the action of these two flame retardant additives on the fire performance of glass-reinforced PBT and allows for identification of the physical and chemical phenomena responsible for their action. Specifically, it

was concluded that the incorporation of MPP significantly reduced the magnitudes of HRR curves. The thermal transport properties of the condensed-phase products of reactions between the decomposing matrix polymer and MPP were found to be primarily responsible for the observed reduction in the HRR. The effect of MPP leveled off after addition of just 4 wt.% because the excess amount of MPP decomposed by itself and did not react with PBT-based components. A relatively minor reduction in the HRR with the addition of DEPAL was predicted by the developed model, which did not account for the DEPAL's gas-phase activity. This reduction was attributed to the impact of DEPAL on the kinetics of the condensed-phase decomposition.

Chapter 7. Conclusions and Future Work

7.1 Conclusions

This work detailed a generalized systematic methodology to develop condensed-phase pyrolysis models of pyrolyzing polymeric materials blended with flame retardants. This work represented the first development of detailed pyrolysis models that provided a quantitative relation between the fire behavior of the flame retardant materials to flame retardant content. Knowledge of this relation enables informed design of flame retardant materials with optimal fire resistance.

This methodology was based on milligram-scale (TGA, DSC, and MCC) and bench-scale gasification experiments and the inverse modeling of these experimental measurements using a numerical pyrolysis framework, ThermaKin2Ds. The methodology was demonstrated on two sets of flame retardant polymeric materials that are commonly encountered in industrial and commercial applications: PA66/GF/RP and PBT/GF/DEPAL/MPP blends. The simultaneous measurements of TGA and DSC data improved the efficiency by reducing the number of thermal analysis experiments required to determine the decomposition kinetics and thermodynamics by half. Inverse analysis of the MCC data allowed for the determination of complete heats of combustion of gaseous pyrolyzate evolved from the sample decomposition. A reaction mechanism that predicted the decomposition behavior of flame retardant materials was developed based on the resulting properties (see Chapter 5 and 6). While the resulting reaction mechanism was based on a lumped-species approach (and thus did not explicitly resolved individual chemical species), it captured all essential aspects of the

thermal decomposition behavior relevant to the flammability of the studied materials within the criteria defined in this work. The resulting reaction mechanism was also capable of predicting the decomposition behavior as a function of heating rates. Moreover, through the introduction of the second-order (two-component) chemical interactions between the polymer matrix and flame retardants, the reaction mechanism gained the capability to capture changes in the decomposition behavior with changes in the flame retardant contents.

An additional improvement in the efficiency was revealed with simultaneous measurement of back surface temperatures, sample shape profiles, and MLR data in the bench-scale gasification tests. A pyrolysis model was subsequently developed based on the resulting reaction mechanism and the thermal transport properties determined through inverse analysis of the gasification experimental measurements (see Chapter 5 and 6). During model construction, an additional complicating phenomenon was investigated. The molten polymer, when blended with glass fiber, was transported from regions of higher concentration to regions of lower concentration through the wick effect. Incorporating the wick effect into the pyrolysis model was required to capture the associated MLR curves. The developed pyrolysis model was capable of predicting MLR data at a bench-scale as a function of material composition and external heating conditions. The error between the experimental and predicted MLR data of the pyrolyzing samples was calculated as approximately 15% on average for external radiative heat fluxes ranging from 30 to 60 kW m^{-2}.

Finally, the effects of flame retardant additives on the fire performance of flame retardant materials were quantified through comparing the HRR curves generated from

additional idealized cone calorimetry simulations. It was demonstrated that when the gas-phase combustion inhibition effect was excluded, aluminum diethyl phosphinate had a relatively minor impact on the HRR profiles, while the impact of melamine polyphosphate and red phosphorus was significant. It was demonstrated that melamine polyphosphate and red phosphorus resulted in a reduction in HRR magnitudes of PBT/GF25 and PA66/GF25 by 20% and 38%, respectively. No significant differences in the HRR reduction were observed when the concentration of melamine polyphosphate is changing from 4 wt.% to 8 wt.% and the concentration of red phosphorus is varying from 2 wt.% to 9 wt.%. This work provides a quantitative analysis of the action of the additives and allows for identification of the physical and/or chemical phenomena responsible for their action.

7.2 Future Work

Following the summary of the present study, some recommendations for future work are summarized in the following.

1. Additional work would be required to account for the impact of oxygen on the gas-solid interface on the pyrolysis before the ignition. RP is known to react slowly with oxygen at ambient temperatures and more rapidly at elevated temperatures. It was found that RP increased the thermo-oxidative stability of the polymer matrix by scavenging oxygen at the surface of the polymer and thus retarding oxidative process [134,141]. The quantification of this impact would enable a more accurate prediction of the ignition time.

2. The chemical interactions in the current reaction mechanism were determined through analyzing the mass loss and heat flow information obtained from STA. STA coupled with Fourier transform infrared spectroscopy and/or mass spectrometry would be a very useful technique to provide additional information of the interaction through identifying the gaseous species released from condensed-phase decomposition.
3. The current study fully characterized the action of flame retardant additives on the condensed-phase pyrolysis process. It is recommended additional microscale flaming calorimeter and cone calorimeter tests should be conducted to understand the effect of the flame retardant additives on the gas-phase combustion process. This would allow for a complete characterization of their roles (including the flame inhibition effect) in improving the fire performance of a material.
4. Additional careful characterization of the wick effect in the glass-fiber-reinforced blends could be conducted to better quantify its dependence on the external heating conditions; such improved quantification would enable the development of a complete pyrolysis model that provides more accurate predictions of burning rates in gasification experiments.
5. The methodology presented in the work should be applied to additional sets of flame retardant materials to further demonstrate its generality. Moreover, it is very important to develop a publicly accessible database filled with material properties for common encountered flame retardant materials. Such a database

would reduce the redundant studies conducted in independent labs and create a set of properties accepted by consensus.

6. Additional larger-scale validation tests, that are more representative of real fire scenarios, should be designed to assess the validity of the pyrolysis models developed in this work.

Appendices

Appendix I: Explanation of Input Files

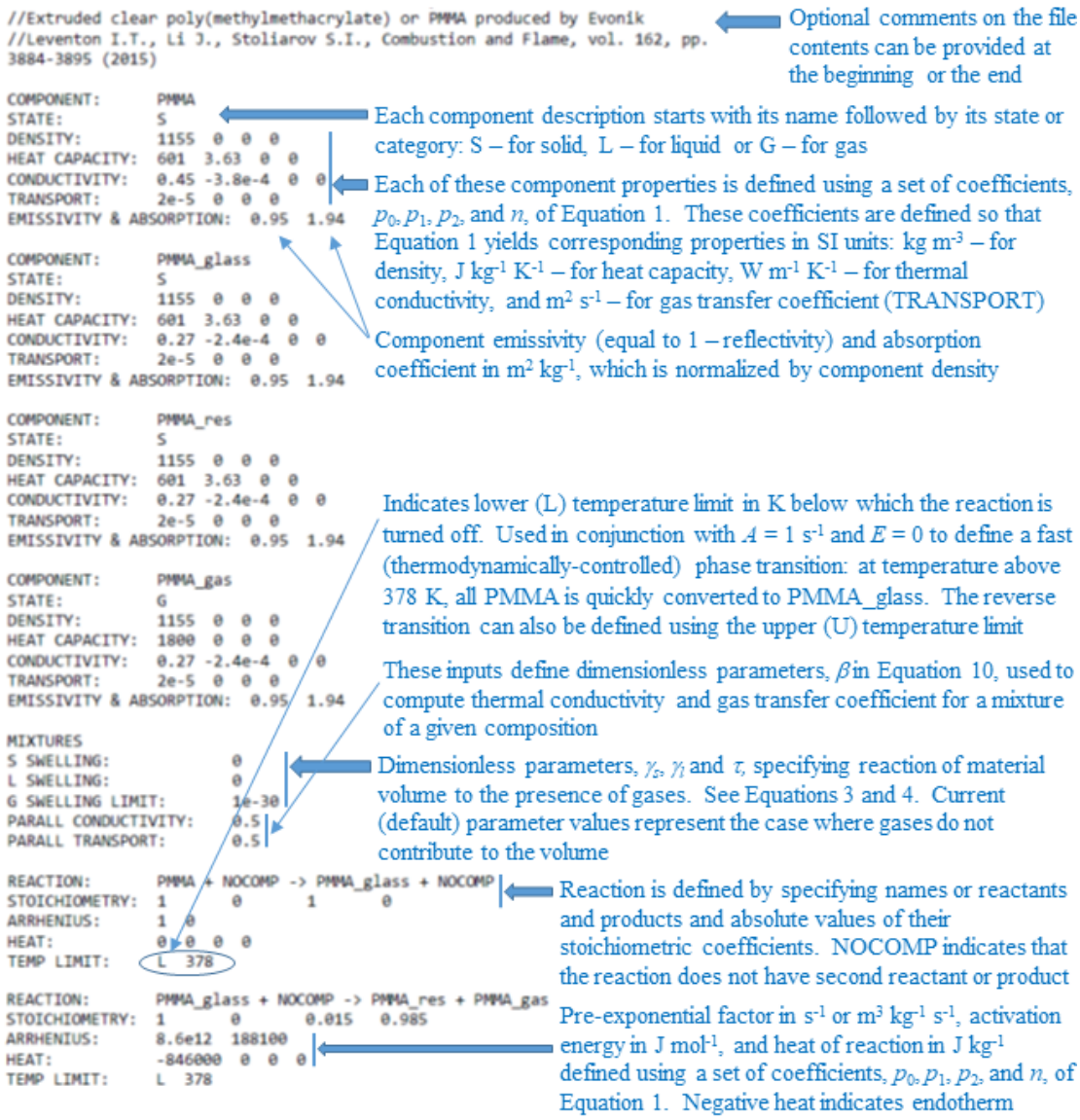

Figure A1 PMMA.cmp – an example of components file used to define material properties.

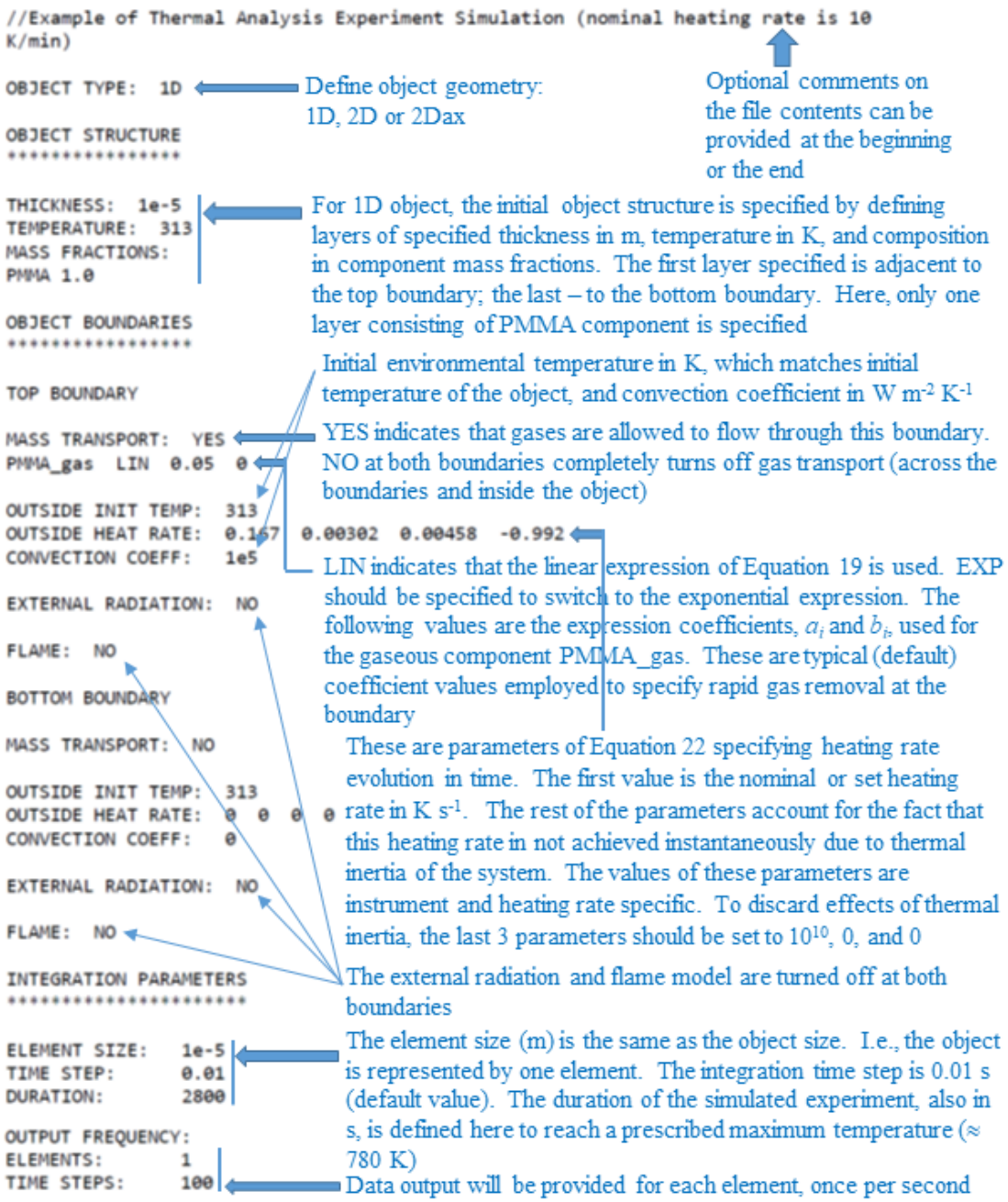

Figure A2 PMMA.cnd – an example of conditions file used to simulate a thermal analysis experiment.

Appendix II: Reaction Model Development

Figure A3 shows the algorithm for building the reaction model for a single-component material. The process starts with identifying the mass loss rate (MLR) peaks and evaluating the corresponding peak mass loss rate (MLR_p), peak temperature (T_p), and residual mass fraction (θ). An initial estimation for the Arrhenius parameters (activation energy, E, and pre-exponential factor, A) for the reaction representing the peak is performed using Eq. (A1) and (A2), which are an approximate solution for the first-order decomposition under linear heating conditions [136].

$$E = \frac{eR_u T_P^2 \frac{MLR_P}{m_0}}{(1-\theta)\frac{dT}{dt}} \tag{A1}$$

$$A = \frac{MLR_P}{\left(\frac{m(T_P)-m_0\theta}{1-\theta}\right)} e^{\frac{E}{R_u T_P}} \tag{A2}$$

In these equations, R is the universal gas constant, $m(T_p)$ is the mass at the peak temperature, $\frac{dT}{dt}$ is the instantaneous heating rate, and m_0 is the initial mass. Using these estimated parameters, ThermaKin2Ds is employed to simulate the reaction and produce the mass loss data. The modeled and experimental mass loss curves are compared. If the temperature of the experimental peak is not captured within the criteria defined in Section 5.1.2 of the present study, the peak temperature is adjusted using the equation in the flowchart (Figure A3) to produce a new set of estimated Arrhenius parameters and modeled results. The symbol $T_{P,mod}$ represents the modeled peak temperature. If the height of the experimental peak is underestimated, the pre-exponential factor is increased; if overestimated, the pre-exponential factor is decreased. The ThermaKin2Ds modeling is subsequently repeated. This manually

iterative process continues until the criteria are met. If, after these adjustments, the initial onset and/or the final decay is not captured sufficiently to bring the agreement between the predicted curve and the experimental curve to within the acceptance criteria, an additional reaction is added to the model. The parameters of the additional reaction are evaluated and adjusted using the same process to bring agreement between the predicted curve and the experimental data within the acceptance criteria.

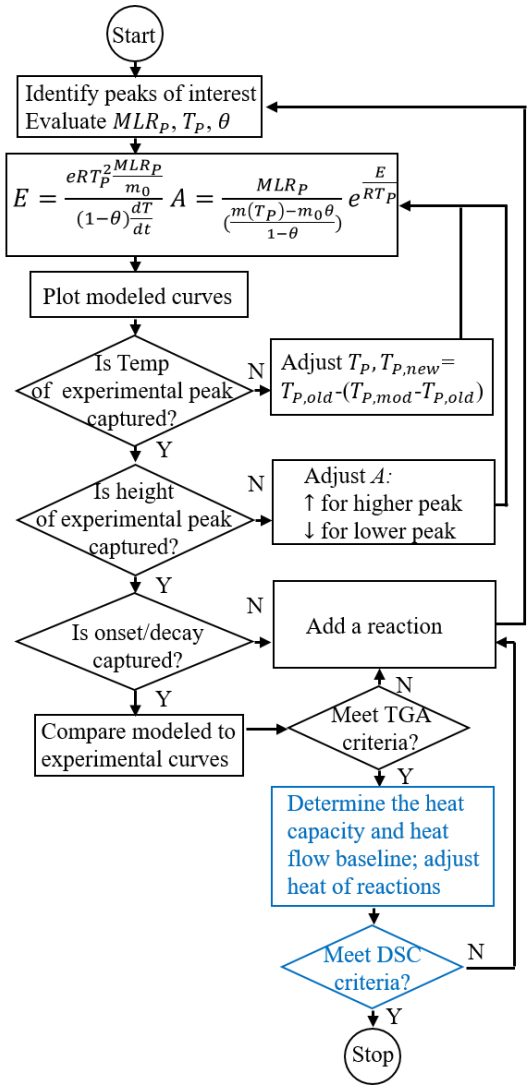

Figure A3 A flowchart of algorithm employed in the reaction model development: Black and blue boxes represent the steps for determining kinetic and thermodynamic parameters, respectively.

After the kinetics of reactions is determined, the heat capacities of condensed-phase components are computed using the heat flow data normalized by the instantaneous heating rate. The parts of the curve that do not contain melting or decomposition peaks are fit with linear temperature-dependent heat capacity expressions. The heat capacity of the final residue is either measured in a separate DSC test or, if the char yield is very low (<5 wt.%), assumed to be equal to the average heat capacity of chars produced by several common polymers, 1700 J $kg^{-1}K^{-1}$ [46]. The heat capacities of the intermediate condensed-phase products are assumed to be equal to the average heat capacity of the molten polymer and final residue. These heat capacities are used to compute a sensible heat flow baseline, HF_{base}. This baseline is calculated as follows:

$$HF_{base}(T) = \sum_{j=1}^{N_c} \frac{m_j(T)}{m_0} c_{p,j}(T) \frac{dT}{dt} \quad (A3)$$

The summation is performed over all the condensed-phase components j. N_c is the number of the condensed-phase components. The normalized mass of each individual component ($m_j(T)$) is obtained from the ThermaKin2Ds simulation results using the kinetic parameters derived from inverse modeling of the TGA data. As an example, Figure A4(b) shows the heat flow baseline computed for the PA66/GF25 blend along with its heat flow data. Subtraction of the baseline from the heat flow curve and subsequent integration of the difference (shaded area in Figure A4(b)) produces an

initial estimates of the heat of melting and the total heat of decomposition. The heats of individual reactions are adjusted to fully capture the shape of the experimental heat flow curve, which is simulated using ThermaKin2Ds, starting with the assumption that all reaction heats have the same value, the total heat of decomposition. If it is determined that the heat flow data cannot be fit with the quality defined by the prescribed criteria, an additional reaction is added and TGA and DSC data are re-modeled.

In the case of PA66/GF25 blend, this process leads to four consecutive reactions, which individual contributions to the mass loss are shown in Figure A4(a). Reaction (1) in Table 5.1 represents the melting process (see Figure A4(b)), while Reactions (2-4) in Table 5.1 are required to represent the mass loss and heat flow data, including the onset and final decay of the curves.

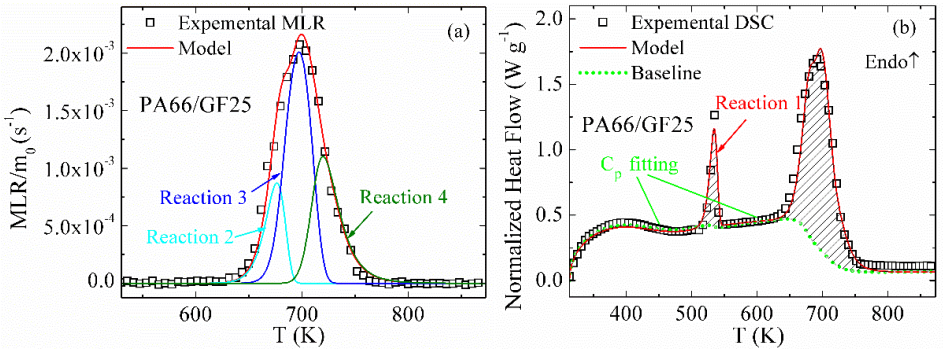

Figure A4 (a) MLR curve for PA66/GF25 along with individual contributions from each reaction; (b) normalized heat flow data for PA66/GF25

Bibliography

[1] London fire: A visual guide to what happened at Grenfell Tower - BBC News, (n.d.). http://www.bbc.com/news/uk-40301289 (accessed October 3, 2017).

[2] ASTM-E176, Standard Terminology of Fire Standards, ASTM Stand. (2015). doi:10.1520/E0176-10A.2.

[3] M. De Poortere, C. Schonbach, M. Simonson, Fire safety of TV set enclosure materials, a survey of European statistics, Fire Mater. 24 (2000) 53–60. doi:10.1002/(SICI)1099-1018(200001/02)24:1<53::AID-FAM721>3.0.CO;2-J.

[4] ASTM E1354-15 Standard Test Method for Heat and Visible Smoke Release Rates for Materials and Products Using an Oxygen Consumption Calorimeter, (2007) 1–20. doi:10.1520/E1354-13.2.

[5] Tests for flammability of plastic materials for parts in devices and appliances, Underwrit. Lab. Inc. (2015).

[6] ASTM E2058-13a Standard Test Methods for Measurement of Material Flammability Using a Fire Propagation Apparatus (FPA), (2013) 1–30. doi:10.1520/E2058-13A.2.

[7] T. Kashiwagi, Polymer combustion and flammability - role of the condensed phase, Twenty-Fifth Symp. Combust. 25 (1994) 1423–1437. doi:10.1016/S0082-0784(06)80786-1.

[8] S.I. Stoliarov, S. Crowley, R.N. Walters, R.E. Lyon, Prediction of the burning rates of non-charring polymers, Combust. Flame. 157 (2009) 2024–2034.

doi:10.1016/j.combustflame.2010.03.011.

[9] J. Li, J. Gong, S.I. Stoliarov, Development of pyrolysis models for charring polymers, Polym. Degrad. Stab. 115 (2015) 138–152. doi:10.1016/j.polymdegradstab.2015.03.003.

[10] A.Y. Snegirev, V.A. Talalov, V. V. Stepanov, J.N. Harris, A new model to predict pyrolysis, ignition and burning of flammable materials in fire tests, Fire Saf. J. 59 (2013) 132–150. doi:10.1016/j.firesaf.2013.03.012.

[11] M.B. McKinnon, S.I. Stoliarov, A. Witkowski, Development of a pyrolysis model for corrugated cardboard, Combust. Flame. 160 (2013) 2595–2607. doi:10.1016/j.combustflame.2013.06.001.

[12] M.B. McKinnon, Y. Ding, S.I. Stoliarov, S. Crowley, R.E. Lyon., Pyrolysis model for a carbon fiber/epoxy structural aerospace composite, J. Fire Sci. 35 (2017) 36–61. doi:10.1177/0734904116679422.

[13] M. Chaos, M.M. Khan, S.B. Dorofeev, Pyrolysis of corrugated cardboard in inert and oxidative environments, Proc. Combust. Inst. 34 (2013) 2583–2590. doi:10.1016/j.proci.2012.06.031.

[14] A.R. Horrocks, D. Price, Fire Retardant Materials, woodhead Publishing, 2001.

[15] C. Di Blasi, Modeling and simulation of combustion processes of charring and non-charring solid fuels, Prog. Energy Combust. Sci. 19 (1993) 71–104. doi:10.1016/0360-1285(93)90022-7.

[16] B. Moghtaderi, The state-of-the-art in pyrolysis modelling of lignocellulosic solid fuels, Fire Mater. 30 (2006) 1–34. doi:10.1002/fam.891.

[17] C. Di Blasi, Modeling chemical and physical processes of wood and biomass pyrolysis, Prog. Energy Combust. Sci. 34 (2008) 47–90. doi:10.1016/j.pecs.2006.12.001.

[18] T.R. Goodman, Application of Integral Methods to Transient Nonlinear Heat Transfer, Adv. Heat Transf. 1 (1964) 51–122. doi:10.1016/S0065-2717(08)70097-2.

[19] J. Quintiere, A semi-quantitative model for the burning rate of solid materials, Fire Saf. Sci. 1 (1992) 3–25.

[20] J. Quintiere, N. Iqbal, An approximate integral model for the burning rate of a thermoplastic-like material, Fire Mater. 18 (1994) 89–98. doi:10.1002/fam.810180205.

[21] M.J. Spearpoint, J.G. Quintiere, Predicting the burning of wood using an integral model, Combust. Flame. 123 (2000) 308–325. doi:10.1016/S0010-2180(00)00162-0.

[22] B. Moghtaderi, V. Novozhilov, D. Fletcher, J.H. Kent, An Integral Model for the Transient Pyrolysis of Solid Materials, 21 (1997) 7–16.

[23] D. Brenner, Chemical Dynamics and Bond-Order Potentials, J. Phys. Chem. 21 (1996) 36–41. doi:10.1021/j100103a007.

[24] A. Strachan, A.C.T. van Duin, D. Chakraborty, S. Dasgupta, W.A. Goddard, A.C.T. van Duin, D. Chakraborty, S. Dasgupta, W.A. Goddard, A.C.T. van Duin, D. Chakraborty, S. Dasgupta, W.A. Goddard, Shock Waves in High-Energy Materials: The Initial Chemical Events in Nitramine RDX, Phys. Rev.

Lett. 91 (2003) 098301. doi:10.1103/PhysRevLett.91.098301.

[25] A. Strachan, E.M. Kober, A.C.T. Van Duin, J. Oxgaard, W.A. Goddard, Thermal decomposition of RDX from reactive molecular dynamics, J. Chem. Phys. 122 (2005). doi:10.1063/1.1831277.

[26] M.R. Nyden, S.I. Stoliarov, P.R. Westmoreland, Z.X. Guo, C. Jee, Applications of reactive molecular dynamics to the study of the thermal decomposition of polymers and nanoscale structures, Mater. Sci. Eng. A. 365 (2004) 114–121. doi:10.1016/j.msea.2003.09.060.

[27] S.I. Stoliarov, P.R. Westmoreland, M.R. Nyden, G.P. Forney, A reactive molecular dynamics model of thermal decomposition in polymers: I. Poly(methyl methacrylate), Polymer (Guildf). 44 (2003) 883–894. doi:10.1016/S0032-3861(02)00761-9.

[28] S.I. Stoliarov, R.E. Lyon, M.R. Nyden, A reactive molecular dynamics model of thermal decomposition in polymers. II. Polyisobutylene, Polymer (Guildf). 45 (2004) 8613–8621. doi:10.1016/j.polymer.2004.10.023.

[29] K.D. Smith, M. Bruns, S.I. Stoliarov, M.R. Nyden, O.A. Ezekoye, P.R. Westmoreland, Assessing the effect of molecular weight on the kinetics of backbone scission reactions in polyethylene using reactive molecular dynamics, Polymer (Guildf). 52 (2011) 3104–3111. doi:10.1016/j.polymer.2011.04.035.

[30] R. Vinu, L.J. Broadbelt, Unraveling Reaction Pathways and Specifying Reaction Kinetics for Complex Systems, Annu. Rev. Chem. Biomol. Eng. 3 (2012) 29–54. doi:10.1146/annurev-chembioeng-062011-081108.

[31] C.H. Bamford, J. Crank, D.H. Malan, A.H. Wilson, The combustion of wood. Part I, Math. Proc. Cambridge Philos. Soc. 42 (2008) 166. doi:10.1017/S030500410002288X.

[32] E. Roy Tinney, The combustion of wooden dowels in heated air, Symp. Combust. 10 (1965) 925–930. doi:10.1016/S0082-0784(65)80235-1.

[33] H.C. Kung, A mathematical model of wood pyrolysis, Combust. Flame. 18 (1972) 185–195. doi:10.1016/S0010-2180(72)80134-2.

[34] C. Lautenberger, C. Fernandez-Pello, Generalized pyrolysis model for combustible solids, Fire Saf. J. 44 (2009) 819–839. doi:10.1016/j.firesaf.2009.03.011.

[35] K. Mcgrattan, S. Hostikka, R. Mcdermott, J. Floyd, C. Weinschenk, K. Overholt, Sixth Edition Fire Dynamics Simulator Technical Reference Guide Volume 4: Configuration Management, 4 (2017). doi:10.6028/NIST.SP.1018-4.

[36] S.I. Stoliarov, R.E. Lyon, Thermo-kinetic model of burning for pyrolyzing materials, Fire Saf. Sci. 9 (2008) 1141–1152. doi:10.3801/IAFSS.FSS.9-1141.

[37] A. Matala, C. Lautenberger, S. Hostikka, Generalized direct method for pyrolysis kinetic parameter estimation and comparison to existing methods, J. Fire Sci. 30 (2012) 339–356. doi:10.1177/0734904112439840.

[38] M.C. Bruns, Inferring and Propagating Kinetic Parameter Uncertainty for Condensed Phase Burning Models, Fire Technol. 52 (2016) 93–120. doi:10.1007/s10694-015-0457-2.

[39] F. Kempel, B. Schartel, G.T. Linteris, S.I. Stoliarov, R.E. Lyon, R.N. Walters,

A. Hofmann, Prediction of the mass loss rate of polymer materials: Impact of residue formation, Combust. Flame. 159 (2012) 2974–2984. doi:10.1016/j.combustflame.2012.03.012.

[40] S.I. Stoliarov, S. Crowley, R.N. Walters, R.E. Lyon, Prediction of the burning rates of charring polymers, Combust. Flame. 157 (2010) 2024–2034. doi:10.1016/j.combustflame.2010.03.011.

[41] ASTM-International, Standard Test Method for Thermal Stability by Thermogravimetry, (2017). doi:10.1520/E2550-07.responsibility.

[42] H. E. Kissinger, Reaction Kinetics in Differential Thermal Analysis, Anal. Chem. 11 (1957) 1702–1706.

[43] A.K. Galwey, M.E. Brown, Application of the arrhenius equation to solid state kinetics: Can this be justified?, Thermochim. Acta. 386 (2002) 91–98. doi:10.1016/S0040-6031(01)00769-9.

[44] P. Kannan, J.J. Biernacki, D.P. Visco, A review of physical and kinetic models of thermal degradation of expanded polystyrene foam and their application to the lost foam casting process, J. Anal. Appl. Pyrolysis. 78 (2007) 162–171. doi:10.1016/j.jaap.2006.06.005.

[45] J. Li, S.I. Stoliarov, Measurement of kinetics and thermodynamics of the thermal degradation for non-charring polymers, Combust. Flame. 160 (2013) 1287–1297. doi:10.1016/j.combustflame.2013.02.012.

[46] J. Li, S.I. Stoliarov, Measurement of kinetics and thermodynamics of the thermal degradation for charring polymers, Polym. Degrad. Stab. 106 (2014) 2–15.

doi:10.1016/j.polymdegradstab.2013.09.022.

[47] S. Vyazovkin, C.A. Wight, Kinetics in Solids, Annu. Rev. Phys. Chem. 48 (1997) 125–149. doi:10.1146/annurev.physchem.48.1.125.

[48] M.E. Brown, M. Maciejewski, S. Vyazovkin, R. Nomen, J. Sempere, A. Burnham, J. Opfermann, R. Strey, H.L. Anderson, A. Kemmler, R. Keuleers, J. Janssens, H.O. Desseyn, C.R. Li, T.B. Tang, B. Roduit, J. Malek, T. Mitsuhashi, Computational aspects of kinetic analysis Part A: The ICTAC Kinetics Project-data, methods and results, Thermochim. Acta. 355 (2000) 125–143. doi:10.1016/S0040-6031(00)00443-3.

[49] H. Bockhorn, Mechanisms and kinetics of thermal decomposition of plastics from isothermal and dynamic measurements, J. Anal. Appl. Pyrolysis. 50 (1999) 77–101. doi:10.1016/S0165-2370(99)00026-1.

[50] J.B. Dahiya, K. Kumar, M. Muller-Hagendorn, H. Bockhorn, Kinetics of isothermal and non-isothermal degradation of cellulose: model-based and model-free methods, Polym. Int. 57 (2008) 722–729. doi:10.1002/pi.2398.

[51] B. Saha, A.K. Ghoshal, Model-fitting methods for evaluation of the kinetics triplet during thermal decomposition of poly(ethylene terephthalate) (PET) soft drink bottles, Ind. Eng. Chem. Res. 45 (2006) 7752–7759. doi:10.1021/ie060282x.

[52] S. Vyazovkin, N. Sbirrazzuoli, Isoconversional kinetic analysis of thermally stimulated processes in polymers, Macromol. Rapid Commun. 27 (2006) 1515–1532. doi:10.1002/marc.200600404.

[53] A.K. Galwey, M.E. Brown, Arrhenius parameters and compensation behaviour in solid-state decompositions, Thermochim. Acta. 300 (1997) 107–115. doi:10.1016/S0040-6031(96)03120-6.

[54] H.L. Friedman, New methods for evaluating kinetic parameters from thermal analysis data, J. Polym. Sci. Part B Polym. Lett. 7 (1969) 41–46. doi:10.1002/pol.1969.110070109.

[55] R.E. Lyon, Direct Isoconversion Method for Nonisothermal Kinetic Analysis, J. Test. Eval. 42 (2014) JTE20140169. doi:10.1520/JTE20140169.

[56] ASTM E698-11, Standard Test Method for Arrhenius Kinetic Constants for Thermally Unstable Materials Using Differential Scanning Calorimetry and the Flynn/Wall/Ozawa Method, Annu. B. ASTM Stand. i (2005) 1–8. doi:10.1520/E0698-11.2.

[57] ASTM International, Standard Test Method for Transition Temperatures and Enthalpies of Fusion and Crystallization of Polymers by Differential Scanning, ASTM Stand. D4318-08 (2012) 1–7. doi:http://dx.doi.org/10.1520/D3418-08.

[58] G. Hohne, W. Hemminger, H.J. Flammersheim, Differential Scanning Calorimetry, 1996. doi:10.1007/978-3-662-03302-9.

[59] N. Bal, G. Rein, Numerical investigation of the ignition delay time of a translucent solid at high radiant heat fluxes, Combust. Flame. 158 (2011) 1109–1116. doi:10.1016/j.combustflame.2010.10.014.

[60] P.T. Tsilingiris, Comparative evaluation of the infrared transmission of polymer films, Energy Convers. Manag. 44 (2003) 2839–2856. doi:10.1016/S0196-

8904(03)00066-9.

[61] M. Försth, A. Roos, Absorptivity and its dependence on heat source temperature and degree of thermal breakdown, Fire Mater. 35 (2011) 285–301. doi:10.1002/fam.1053.

[62] G.T. Linteris, M. Zammarano, B. Wilthan, L. Hanssen, Absorption and relfection of infrared radiation by polymers in fire-like environments, Fire Mater. 36 (2012) 537–553. doi:10.1002/fam.

[63] F. Jiang, J.L. de Ris, M.M. Khan, Absorption of thermal energy in PMMA by in-depth radiation, Fire Saf. J. 44 (2009) 106–112. doi:10.1016/j.firesaf.2008.04.004.

[64] ASTM, Standard Test Method for Steady-State Heat Flux Measurements and Thermal Transmission Properties by Means of the Guarded-Hot-Plate, Annu. B. ASTM Stand. (2014) 1–23. doi:10.1520/C0177-13.2.

[65] ASTM, Standard Test Method for Steady-State Thermal Transmission Properties by Means of the Heat Flow Meter Apparatus, ASTM Int. (2015) 1–15. doi:10.1520/C0518-10.2.

[66] T. Harada, T. Hata, S. Ishihara, Thermal constants of wood during the heating process measured with the laser flash method, J. Wood Sci. 44 (1998) 425–431. doi:10.1007/BF00833405.

[67] ASTM, Standard test method for thermal diffusivity by the flash method, ASTM, West Conshohocken, PA. i (2001) 1–11. doi:10.1520/E1461-13.2.

[68] X. Zhang, M. Fujii, Measurements of the thermal conductivity and thermal

diffusivity of polymers, Polym. Eng. Sci. 43 (2003) 1755–1764. doi:10.1002/pen.10148.

[69] ASTM, Standard Test Method for Thermal Conductivity of Refractories by Hot Wire (Platinum Resistance Thermometer Technique) 1, Astm. 09 (2015) 1–6. doi:10.1520/C1113.

[70] M.J. Assael, S. Botsios, K. Gialou, I.N. Metaxa, Thermal conductivity of polymethyl methacrylate (PMMA) and borosilicate crown glass BK7, Int. J. Thermophys. 26 (2005) 1595–1605. doi:10.1007/s10765-005-8106-5.

[71] S.I. Stoliarov, N. Safronava, R.E. Lyon, The effect of variation in polymer properties on the rate of burning, Fire Mater. 33 (2009) 257–271. doi:10.1002/fam.1003.

[72] G.T. Linteris, Numerical simulations of polymer pyrolysis rate: Effect of property variations, Fire Mater. 35 (2011) 463–480. doi:10.1002/fam.

[73] G.T. Linteris, R.E. Lyon, S.I. Stoliarov, Prediction of the gasification rate of thermoplastic polymers in fire-like environments, Fire Saf. J. 60 (2013) 14–24. doi:10.1016/j.firesaf.2013.03.018.

[74] M. Tsoi, J. Zhuge, R.H. Chen, J. Gou, Modeling and experimental studies of thermal degradation of glass fiber reinforced polymer composites, Fire Mater. 38 (2014) 247–263. doi:10.1002/fam.

[75] P.J. Austin, R.R. Buch, T. Kashiwagi, Gasification of Silicone Fluids Under External Thermal Radiation, 1997. doi:NISTIR 6041.

[76] M. Chaos, M.M. Khan, N. Krishnamoorthy, J.L. De Ris, S.B. Dorofeev,

Evaluation of optimization schemes and determination of solid fuel properties for CFD fire models using bench-scale pyrolysis tests, Proc. Combust. Inst. 33 (2011) 2599–2606. doi:10.1016/j.proci.2010.07.018.

[77] A. Witkowski, B. Girardin, M. Forsth, F. Hewitt, G. Fontaine, S. Duquesne, S. Bourbigot, T.R. Hull, Development of an anaerobic pyrolysis model for fire retardant cable sheathing materials, Polym. Degrad. Stab. 113 (2015) 208–217. doi:10.1016/j.polymdegradstab.2015.01.006.

[78] J. Li, J. Gong, S.I. Stoliarov, Gasification experiments for pyrolysis model parameterization and validation, Int. J. Heat Mass Transf. 77 (2014) 738–744. doi:10.1016/j.ijheatmasstransfer.2014.06.003.

[79] C. Lautenberger, G. Rein, C. Fernandez-Pello, The application of a genetic algorithm to estimate material properties for fire modeling from bench-scale fire test data, Fire Saf. J. 41 (2006) 204–214. doi:10.1016/j.firesaf.2005.12.004.

[80] R. Webster, M. Lázaro, D. Alvear, J. Capote, A. Trouvé, Limitations in Current Parameter Estimation Techniques for Pyrolysis Modelling, in: Proc. Sixth Int. Semin. Fire Explos. Hazards, Research Publishing Services, Singapore, 2011: pp. 1008–1019. doi:10.3850/978-981-08-7724-8_15-02.

[81] J. Li, S.I. Stoliarov, Measurement of kinetics and thermodynamics of the thermal degradation for non-charring polymers, Polym. Degrad. Stab. 106 (2013) 2–15. doi:10.1016/j.polymdegradstab.2013.09.022.

[82] M.B. Mckinnon, S.I. Stoliarov, Pyrolysis model development for a multilayer floor covering, Materials (Basel). 8 (2015) 6117–6153.

doi:10.3390/ma8095295.

[83] R.E. Lyon, R.N. Walters, S.I. Stoliarov, N. Safronava, Principles and practice of microscale combustion calorimetry, Fed. Aviat. Adm. Atl. City Airport, NJ 8405. (2013). doi:DOT/FAA/TC-12/53, R1.

[84] B. Girardin, G. Fontaine, S. Duquesne, M. Försth, S. Bourbigot, Measurement of kinetics and thermodynamics of the thermal degradation for flame retarded materials: application to EVA/ATH/NC, J. Anal. Appl. Pyrolysis. (2017). doi:10.1016/j.jaap.2016.12.034.

[85] A.B. Morgan, J.W. Gilman, An overview of flame retardancy of polymeric materials: application, technology, and future directions, Fire Mater. 37 (2013) 259–279. doi:10.1002/fam.2128.

[86] L.S. Birnbaum, D.F. Staskal, Brominated flame retardants: Cause for concern?, Environ. Health Perspect. 112 (2004) 9–17. doi:10.1289/ehp.6559.

[87] K. D'silva, A. Fernandes, M. Rose, Brominated Organic Micropollutants—Igniting the Flame Retardant Issue, Crit. Rev. Environ. Sci. Technol. 34 (2004) 141–207. doi:10.1080/10643380490430672.

[88] C.H. Marvin, G.T. Tomy, J.M. Armitage, J.A. Arnot, L. McCarty, A. Covaci, V. Palace, Hexabromocyclododecane: Current understanding of chemistry, environmental fate and toxicology and implications for global management, Environ. Sci. Technol. 45 (2011) 8613–8623. doi:10.1021/es201548c.

[89] K.H. Pawlowski, B. Schartel, Flame retardancy mechanisms of triphenyl phosphate, resorcinol bis(diphenyl phosphate) and bisphenol A bis(diphenyl

phosphate) in polycarbon- ate/acrylonitrile–butadiene–styrene blends, Polym. Int. 56 (2007) 1404–1414. doi:10.1002/pi.

[90] U. Braun, B. Schartel, Flame retardant mechanisms of red phosphorus and magnesium hydroxide in high impact polystyrene, Macromol. Chem. Phys. 205 (2004) 2185–2196. doi:10.1002/macp.200400255.

[91] U. Braun, B. Schartel, M.A. Fichera, C. Jager, Flame retardancy mechanisms of aluminium phosphinate in combination with melamine polyphosphate and zinc borate in glass-fibre reinforced polyamide 6,6, Polym. Degrad. Stab. 92 (2007) 1528–1545. doi:10.1016/j.polymdegradstab.2007.05.007.

[92] U. Braun, H. Bahr, B. Schartel, Fire retardancy effect of aluminium phosphinate and melamine polyphosphate in glass fibre reinforced polyamide 6, E-Polymers. 10 (2010). doi:10.1515/epoly.2010.10.1.443.

[93] S. V. Levchik, A Review of Recent Progress in Phosphorus-based Flame Retardants, J. Fire Sci. 24 (2006) 345–364. doi:10.1177/0734904106068426.

[94] S. V Levchik, E.D. Weil, Combustion and fire retardancy of aliphatic nylons, 49 (2000) 1033–1073.

[95] G. Fontaine, S. Bourbigot, Intumescent polylactide: a nonflammable material, J. Appl. Polym. Sci. 113 (2009) 3860–3865. doi:10.1002/app.30379.

[96] A. Casu, G. Camino, M. De Giorgi, D. Flath, A. Laudi, V. Morone, Effect of glass fibres and fire retardant on the combustion behaviour of composites, glass fibres-poly(butylene terephthalate), Fire Mater. 22 (1998) 7–14. doi:10.1002/(SICI)1099-1018(199801/02)22:1<7::AID-FAM623>3.0.CO;2-3.

[97] L. Liu, Y. Liu, Y. Han, Y. Liu, Q. Wang, Interfacial charring method to overcome the wicking action in glass fiber-reinforced polypropylene composite, Compos. Sci. Technol. 121 (2015) 9–15. doi:10.1016/j.compscitech.2015.09.006.

[98] B. Schartel, Phosphorus-based flame retardancy mechanisms—old hat or a starting point for future development, Materials (Basel). 3 (2010) 4710–4745. doi:10.3390/ma3104710.

[99] B. Schartel, R. Kunze, D. Neubert, Red phosphorus-controlled decomposition for fire retardant PA 66, J. Appl. Polym. Sci. 83 (2002) 2060–2071. doi:10.1002/app.10144.

[100] F. Gao, L. Tong, Z. Fang, Effect of a novel phosphorous-nitrogen containing intumescent flame retardant on the fire retardancy and the thermal behaviour of poly(butylene terephthalate), Polym. Degrad. Stab. 91 (2006) 1295–1299. doi:10.1016/j.polymdegradstab.2005.08.013.

[101] A.R. Horrocks, D. Price, Fire Retardant Materials, 2001.

[102] U. Braun, B. Schartel, Flame retardancy mechanisms of aluminium phosphinate in combination with melamine cyanurate in glass-fibre-reinforced poly(1,4-butylene terephthalate), Macromol. Mater. Eng. 293 (2008) 206–217. doi:10.1002/mame.200700330.

[103] U. Braun, H. Bahr, Heinz Sturm, B. Schartel., Flame retardancy mechanisms of metal phosphinates and metal phosphinates in combination with melamine cyanurate in glass-fiber reinforced poly(1,4-butylene terephthalate): the

influence of metal cation, Polym. Adv. Technol. 19 (2008) 680–692. doi:10.1002/pat.

[104] G. Camino, L. Costa, M.P. Luda di Cortemiglia, Overview of fire retardant mechanisms, Polym. Degrad. Stab. 33 (1991) 131–154. doi:10.1016/0141-3910(91)90014-I.

[105] J. Xiao, Y. Hu, L. Yang, Y. Cai, L. Song, Z. Chen, W. Fan, Fire retardant synergism between melamine and triphenyl phosphate in poly(butylene terephthalate), Polym. Degrad. Stab. 91 (2006) 2093–2100. doi:10.1016/j.polymdegradstab.2006.01.018.

[106] S. V Levchik, E.D. Weil, M. Lewin, Thermal decomposition of aliphatic nylons, Polym. Int. 48 (1999) 532–557. doi:10.1002/(SICI)1097-0126(199907)48:7<532::AID-PI214>3.0.CO;2-R.

[107] F. Samyn, S. Bourbigot, Thermal decomposition of flame retarded formulations PA6/aluminum phosphinate/melamine polyphosphate/organomodified clay: Interactions between the constituents?, Polym. Degrad. Stab. 97 (2012) 2217–2230. doi:10.1016/j.polymdegradstab.2012.08.004.

[108] W.S. Jou, K.N. Chen, D.Y. Chao, C.Y. Lin, J.T. Yeh, Flame retardant and dielectric properties of glass fibre reinforced nylon-66 filled with red phosphorous, Polym. Degrad. Stab. 74 (2001) 239–245. doi:10.1016/S0141-3910(01)00109-4.

[109] Y. Liu, Q. Wang, Melamine cyanurate-microencapsulated red phosphorus flame retardant unreinforced and glass fiber reinforced polyamide 66, Polym. Degrad.

Stab. 91 (2006) 3103–3109. doi:10.1016/j.polymdegradstab.2006.07.026.

[110] Y. Ding, K. Kwon, S.I. Stoliarov, R.H. Kraemer, Development of a semi-global reaction mechanism for thermal decomposition of a polymer containing reactive flame retardant, 37th Int. Symp. Combust. (2018). https://doi.org/10.1016/j.proci.2018.05.073

[111] Y. Ding, S. Stoliarov, R. Kraemer, Development of a semiglobal reaction mechanism for the thermal decomposition of a polymer containing reactive flame retardants: Application to glass-fiber-reinforced polybutylene terephthalate blended with aluminum diethyl phosphinate and melamine polypho, Polymers (Basel). 10 (2018) 1137. doi:10.3390/polym10101137.

[112] Y. Ding, S.I. Stoliarov, R.H. Kraemer, Pyrolysis model development for a polymeric material containing multiple flame retardants: Relationship between heat release rate and material composition, Combust. Flame. (2019). https://doi.org/10.1016/j.combustflame.2019.01.003

[113] Y. Ding, J.D. Swann, Q. Sun, S.I. Stoliarov, R.H. Kraemer, Development of a Pyrolysis Model of Glass Fiber Reinforced Polyamide 66 Blended with Red Phosphorus: Relationship between Flammability Behavior and Material Composition, Compos. Part B Eng. (2019). Under Review.

[114] D. V. Rosato, M.G. Rosato, Injection molding handbook, Springer Science & Business Media, 2012.

[115] STA 449 F3 Jupiter brochure; NETASCH, (2012). https://www.netzsch-thermal-analysis.com/en/.

[116] J.D. Swann, Y. Ding, S.I. Stoliarov, Characterization of pyrolysis and combustion of rigid poly(vinyl chloride) using two-dimensional modeling, Int. J. Heat Mass Transf. 132 (2018) 347–361. doi:S0017931018339838.

[117] J.D. Swann, Y. Ding, M.B. McKinnon, S.I. Stoliarov, Controlled atmosphere pyrolysis apparatus II (CAPA II): A new tool for analysis of pyrolysis of charring and intumescent polymers, Fire Saf. J. 91 (2017) 130–139. doi:10.1016/j.firesaf.2017.03.038.

[118] S.I. Stoliarov, I.T. Leventon, R.E. Lyon., Two-dimensional model of burning for pyrolyzable solids, Fire Mater. 38 (2014) 391–408. doi:10.1002/fam.

[119] K. McGrattan, S. Hostikka, R. McDermott, J. Floyd, C. Weinschenk, K. Overholt, Sixth Edition Fire Dynamics Simulator Technical Reference Guide Volume 1 : Mathematical Model, 1 (2017) 1–147. doi:http://dx.doi.org/10.6028/NIST.SP.1018-1.

[120] F.P. Incropera, D.P. DeWitt, T.L. Bergman, A.S. Lavine, Fundamentals of Heat and Mass Transfer, John Wiley & Sons, 2007. doi:10.1016/j.applthermaleng.2011.03.022.

[121] I.T. Leventon, J. Li, S.I. Stoliarov, A flame spread simulation based on a comprehensive solid pyrolysis model coupled with a detailed empirical flame structure representation, Combust. Flame. 162 (2015) 3884–3895. doi:10.1016/j.combustflame.2015.07.025.

[122] W.H. Press, S.A. Teukolsky, W.T. Vetterling, B.P. Flannery, Numerical Recipes in C++, (1988) 444.

[123] H.S. Carslaw, J.C. Jaeger, Conduction of Heat in Solids, 2nd ed., Oxford University Press, 1959.

[124] J. Crank, The mathematics of diffusion, 2nd ed., Clarendon Press, Oxford, 1975. doi:10.1016/0306-4549(77)90072-X.

[125] Y. Ding, M.B. McKinnon, S.I. Stoliarov, G. Fontaine, S. Bourbigot, Determination of kinetics and thermodynamics of thermal decomposition for polymers containing reactive flame retardants: Application to poly(lactic acid) blended with melamine and ammonium polyphosphate, Polym. Degrad. Stab. 129 (2016) 347–362. doi:10.1016/j.polymdegradstab.2016.05.014.

[126] MatWeb, "E-Glass Fiber, Generic," MatWeb Material Property Data, (n.d.). http://matweb.com/search/DataSheet.aspx?MatGUID=d9c18047c49147a2a7c0b0bb1743e812 (accessed June 4, 2018).

[127] J.J. McKetta, Encyclopedia of Chemical Processing and Design: Volume 36 - Phosphorus to Pipeline Failure, Subsidence Strains, CRC press, New York, 1990.

[128] C. Hugget, Estimation of Rate of Heat Release by Means of Oxygen Consumption Measurement, Fire Mater. 4 (1980) 61. doi:10.1002/fam.810040202.

[129] NIST Chemistry WebBook, (n.d.). http://webbook.nist.gov/chemistry/ (accessed June 4, 2018).

[130] J. Howell, M. Menguc, R. Siegel, Thermal radiation heat transfer, 2010.

[131] A. Ito, T. Kashiwagi, Characterization of flame spread over PMMA using

holographic interferometry sample orientation effects, Combust. Flame. 71 (1988) 189–204. doi:10.1016/0010-2180(88)90007-7.

[132] J.G. Quintiere, Fundamentals of Fire Phenomena, 2006. doi:10.1002/0470091150.

[133] U. Braun, B. Schartel, Effect of red phosphorus and melamine polyphosphate on the fire behavior of HIPS, J. Fire Sci. 23 (2005) 5–30. doi:10.1177/0734904105043451.

[134] E.N. Peters, Flame-retardant thermoplastics . I . polyethylene-red phosphorus, J. Appl. Polym. Sci. 24 (1979) 1457–1464.

[135] S. Duquesne, G. Fontaine, O. Cérin-Delaval, B. Gardelle, G. Tricot, S. Bourbigot, Study of the thermal degradation of an aluminium phosphinate-aluminium trihydrate combination, Thermochim. Acta. 551 (2013) 175–183. doi:10.1016/j.tca.2012.10.025.

[136] R.E. Lyon, R.N. Walters, S.I. Stoliarov, A thermal analysis method for measuring polymer flammability, J. ASTM Int. 3 (2006) 1–18. doi:10.1520/JAI13895.

[137] Albis, Ultramid® A24 E PA66 BASF, n.d. https://www.albis.com/de/products/download/doc/en/SI/basf/UltramidA24E (accessed November 9, 2018).

[138] BASF Ultradur B 4500 PBT, (n.d.). http://www.matweb.com/search/datasheet.aspx?matguid=0e804016f8044be6a786f6f903c86daf&ckck=1.

[139] P. Patnaik, Handbook of Inorganic Chemicals, 2003.

[140] F. Raffan-Montoya, X. Ding, S.I. Stoliarov, R.H. Kraemer, Measurement of Heat Release in Laminar Diffusion Flames Fuelled by Controlled Pyrolysis of Milligram-sized Solid Samples: Impact of Bromine- and Phosphorus- based Flame Retardants, Combust. Flame J. 162 (2015) 4660–4670. doi:https://doi.org/10.1016/j.combustflame.2015.09.031.

[141] G. Küper, J. Hormes, K. Sommer, In situ X-ray absorption spectroscopy at the K-edge of red phosphorus in polyamide 6,6 during a thermo-oxidative degradation, Macromol. Chem. Phys. 195 (1994) 1741–1753. doi:10.1002/macp.1994.021950524.